

AD-A092 410

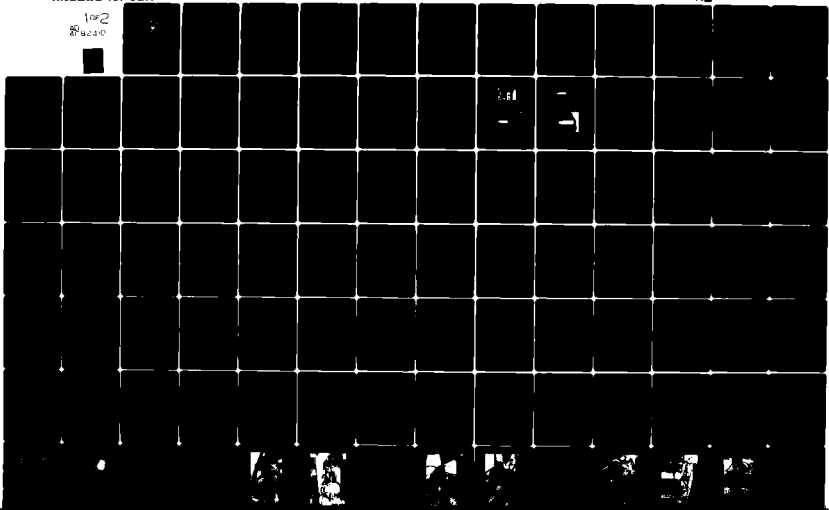
NAVAL POSTGRADUATE SCHOOL MONTEREY CA  
BALL OBTURATION OF A SPIN STABILIZED TUBULAR PROJECTILE.(U)  
JUN 80 J W BLOOMER

F/6 19/1

UNCLASSIFIED

NL

1 of 2  
280000

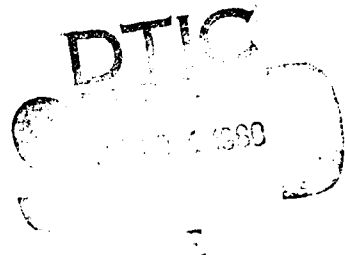


LEVEL II

2

# NAVAL POSTGRADUATE SCHOOL Monterey, California

AD A092410



## THESIS

BALL OBTURATION OF A SPIN STABILIZED  
TUBULAR PROJECTILE

by

James Wayne Bloomer II

June 1980

Thesis Advisor:

R. H. Nunn

Approved For Public Release; Distribution Unlimited

DDC FILE COPY

8 1 1 2 5

Unclassified

SECURITY CLASSIFICATION OF THIS PAGE (When Data Entered)

REPORT DOCUMENTATION PAGE		READ INSTRUCTIONS BEFORE COMPLETING FORM	
1. REPORT NUMBER	2. GOVT ACCESSION NO.	3. RECIPIENT'S CATALOG NUMBER	
	AD A092410		
4. TITLE (and Subtitle)	5. TYPE OF REPORT & PERIOD COVERED	6. PERFORMING ORG. REPORT NUMBER	
BALL OBTURATION OF A SPIN STABILIZED TUBULAR PROJECTILE	Master's Thesis June 1980		
7. AUTHOR(s)	8. CONTRACT OR GRANT NUMBER(s)		
James Wayne Bloomer II			
9. PERFORMING ORGANIZATION NAME AND ADDRESS	10. PROGRAM ELEMENT, PROJECT, TASK AREA & WORK UNIT NUMBERS		
Naval Postgraduate School Monterey, California 93940	(11)		
11. CONTROLLING OFFICE NAME AND ADDRESS	12. REPORT DATE	13. NUMBER OF PAGES	
Naval Postgraduate School Monterey, California 93940	June 1980	126	
14. MONITORING AGENCY NAME & ADDRESS (if different from Controlling Office)	15. SECURITY CLASS. (of this report)		
(12) 107	Unclassified		
16. DISTRIBUTION STATEMENT (of this Report)			
Approved for public release; distribution unlimited			
17. DISTRIBUTION STATEMENT (of the abstract entered in Block 20, if different from Report)			
18. SUPPLEMENTARY NOTES			
19. KEY WORDS (Continue on reverse side if necessary and identify by block number)			
Projectile Exterior Ballistics Tubular Obturation Sabots			
20. ABSTRACT (Continue on reverse side if necessary and identify by block number)			
An analytical model was constructed to predict the response of the ball obturator in a ball obturated, spin stabilized tubular projectile (BOT). Torques acting on the obturator were considered to be due to fluid and sliding friction forces. An experimental apparatus was designed, and built to simulate the BOT. Data obtained were the times required for the obturator to nutate through a known angle over a range of			

DD FORM 1 JAN 73 1473 (Page 1)

EDITION OF 1 NOV 68 IS OBSOLETE S/N 0102-014-8601

251-150

Unclassified SECURITY CLASSIFICATION OF THIS PAGE (When Data Entered)

projectile angular velocities. Utilizing published coefficient of sliding friction information and a linear approximation of the exact solution, the trend in the data to go through a minimum value was duplicated. A least squares fit of the linear approximation to the data allowed the formulation of a new sliding friction coefficient,  $\mu_s$ . - Using this value of  $\mu_s$ , a plot of the least squares fit, values from the exact solution and the experimental data was constructed. The correlation is extremely good so that confidence in the predictive capabilities of the model was gained.

Accession For	
1.111	<input checked="" type="checkbox"/>
1.112	<input type="checkbox"/>
1.113	<input type="checkbox"/>
1.114	<input type="checkbox"/>
Date	
Time	
Initials	
Special	
A	

Approved For Public Release; Distribution Unlimited

BALL OBTURATION OF A SPIN STABILIZED  
TUBULAR PROJECTILE

by

James Wayne Bloomer II  
Lieutenant, United States Navy  
B.S., University of New Mexico, 1974

Submitted In Partial Fulfillment Of The  
Requirements For The Degrees Of

MASTER OF SCIENCE IN MECHANICAL ENGINEERING  
and  
MECHANICAL ENGINEER

from the

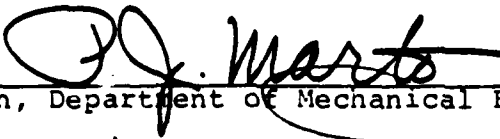
NAVAL POSTGRADUATE SCHOOL  
June 1980

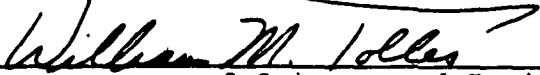
Author

  
\_\_\_\_\_

Approved by:

  
\_\_\_\_\_ Thesis Advisor

  
\_\_\_\_\_ Chairman, Department of Mechanical Engineering

  
\_\_\_\_\_ Dean of Science and Engineering

## ABSTRACT

An analytical model was constructed to predict the response of the ball obturator in a ball obturated, spin stabilized tubular projectile (BOT). Torques acting on the obturator were considered to be due to fluid and sliding friction forces. An experimental apparatus was designed, and built to simulate the BOT. Data obtained were the times required for the obturator to nutate through a known angle over a range of projectile angular velocities. Utilizing published coefficient of sliding friction information and a linear approximation of the exact solution, the trend in the data to go through a minimum value was duplicated. A least squares fit of the linear approximation to the data allowed the formulation of a new sliding friction coefficient,  $\mu_s$ . Using this value of  $\mu_s$ , a plot of the least squares fit, values from the exact solution and the experimental data was constructed. The correlation is extremely good so that confidence in the predictive capabilities of the model was gained.

## TABLE OF CONTENTS

I.	INTRODUCTION -----	15
	A. BACKGROUND -----	15
	B. RECENT DEVELOPMENTAL STUDIES -----	16
	1. Range Tests -----	16
	2. Target Impact Tests -----	18
	3. Weapons System Capability -----	19
	4. Review Of Internal Shock Wave Considerations -----	22
	5. Laboratory/Wind Tunnel Testing -----	31
	C. PURPOSE OF STUDY -----	32
II.	ANALYSIS -----	36
	A. DEVELOPMENT AND SOLUTION OF THE EQUATIONS OF MOTION -----	36
	B. MODELING OF THE APPLIED TORQUES -----	47
	1. Moments Due To Viscous Effects -----	47
	2. Moments Due To Sliding Friction -----	57
	C. DEVELOPMENT OF AN APPROXIMATE SOLUTION -----	66
	D. THE EFFECT OF GEOMETRY ON OBTURATOR RESPONSE ---	75
III.	EXPERIMENTATION -----	81
	A. EXPERIMENTAL APPARATUS -----	81
	B. EXPERIMENTAL PROCEDURE -----	91
	C. DATA REDUCTION -----	96
IV.	CORRELATION OF RESULTS -----	97
V.	CONCLUSIONS -----	114

VI. RECOMMENDATIONS -----	117
APPENDIX A - COMPUTER CODE -----	118
APPENDIX B - RAW DATA -----	121
LIST OF REFERENCES -----	122
INITIAL DISTRIBUTION LIST -----	125

LIST OF FIGURES

1.	Photograph of 20-mm Ball Obturated Tubular Projectile (BOT), components and conventional 20-mm projectile.----	20
2.	a. Standard 20-mm projectile in flight with detached bow shock. -----	20
	b. BOT in flight with passage blocked resulting in detached bow shock. -----	21
	c. BOT with no blockage in passage. Only attached oblique shocks emanating from the lip. -----	21
3.	Sketch of Split (a) and Solid (b) disk, pusher-type, discarding sabots/obturators. -----	23
4.	Drawing of BOT with obturator oriented to block the passage (loading position). -----	34
5.	Drawing of BOT illustrating body-fixed and inertial coordinate systems and angular velocity components associated with each. -----	37
6.	Drawing of the guide used in determining the inertia tensor and moments of inertia of the obturator. -----	39
7.	Drawing of BOT illustrating relationship of Euler angles to coordinate axes. -----	43
8.	Diagram of differential area of sphere utilized in calculation of fluid friction. -----	50
9.	$\theta$ vs. time for applied torques due to fluid friction from Couette model (Eq. 32). -----	53

10.	$\theta$ vs. time for obturator with applied torques due to fluid friction with increasing orders of magnitude of S. -----	53
11.	Diagram showing area under the influence of viscous shearing stresses developed from Couette flow theory.---	55
12.	Diagram showing the geometric relationships for determining moment arms $r_1$ and $r_2$ for calculating sliding friction torques due to aerodynamic forces. -----	60
13.	Plot of $\theta$ vs. time for BOT utilizing aerodynamic force development. -----	67
14.	Plot of $\theta$ vs. time for BOT utilizing gravitational force development. -----	68
15.	Comparison plot of $\theta$ vs. time for the (a) exact and (b) approximate solutions. -----	76
16.	Comparison plot of $\theta$ vs. time for obturator material densities of (a) 6000 Kg/m <sup>3</sup> and (b) 10,000 Kg/m <sup>3</sup> .-----	78
17.	Comparison plot of $\theta$ vs. time for obturator hole radii of (a) 3.75 mm and (b) 5.58 mm. -----	80
18.	Obturator boring process. -----	82
19.	Milling of obturator mount at a specified angle. -----	82
20.	Obturator mounts after being machined to desired angle for polishing. -----	83
21.	Illustration of polished spot orientation. -----	83
22.	Photograph of obturator with three piece lucite housing components. -----	84

23.	Photograph of assembled lucite housing and aluminum end pieces. -----	84
24.	Photograph of assembled spin-up rig showing obturator supported by lucite housing. -----	86
25.	Photograph of spin-up rig showing bucket wheel, air jet orientation and Proximitor mounted above bucket wheel. -----	87
26.	Photograph of holding-jet nozzle, Proximitor and solenoid plunger (extended) prior to obturator release.-	89
27.	Photograph of holding-jet nozzle, Proximitor and solenoid plunger retracted after obturator release. -----	90
28.	Photograph of light sensitive diode housing (1) illuminated by reflected laser beam from the polished end of the solenoid plunger. -----	92
29.	Photograph of complete experimental apparatus layout.---	93
30.	Photograph of laser reflection on the target from the polished spot on the obturator. -----	94
31.	Photograph of circle traced by the reflected laser (Fig. 30) while the apparatus is spinning. -----	94
32.	$\theta$ vs. time for gravity model, $\omega_p = 40 \text{ sec}^{-1}$ -----	98
33.	$\theta$ vs. time for gravity model, $\omega_p = 100 \text{ sec}^{-1}$ -----	99
34.	$\theta$ vs. time for gravity model, $\omega_p = 200 \text{ sec}^{-1}$ -----	100
35.	$\theta$ vs. time for gravity model, $\omega_p = 500 \text{ sec}^{-1}$ -----	101
36.	$\theta$ vs. time for gravity model, $\omega_p = 700 \text{ sec}^{-1}$ -----	102
37.	$\theta$ vs. time for gravity model, $\omega_p = 1000 \text{ sec}^{-1}$ -----	103

38.	Plot of experimental data and $t_{cr}$ calculated from approximate solution.-----	104
39.	Plot of $t_{cr}$ vs. $\omega_p$ for various values of sliding friction coefficient $\mu_s$ .-----	105
40.	Plot of $t_{cr}$ vs. $\omega_p$ for various values of $\theta_0$ .-----	106
41.	Plot of experimental data showing the relative insensitivity to small variations in $\theta_0$ .-----	107
42.	Plot of experimental data on plot from Fig. 39 showing close correlation for $\omega_p$ 200 $\text{sec}^{-1}$ with curve for $\mu_s = 0.55$ .-----	108
43.	Plot of experimental data, linear approximation from least squares fit of data and values obtained from exact solution for $\mu_s = 0.5437$ .-----	113

## NOMENCLATURE

(Only primary symbols are listed. Intermediate quantities are defined in the text.)

A	major mass moment in inertia, N-m-s
C	minor mass moment of inertia, N-m-s
G	applied torque, N-m
h	width of gap between ball and projectile, m
M	magnitude of applied torque, N-m
$r_p$	radius of hole through projectile, m
$r_s$	radius of hole through ball, m
$R_s$	radius of ball, m
$\beta$	$\sin^{-1} (r_s/R_s)$
$\theta, \phi, \psi$	Euler angles (see Fig. 7)
$\lambda$	$(C/A)-1$
$\mu_f$	fluid viscosity (Pa-s)
$\mu_s$	coefficient of sliding friction, dimensionless
$\omega$	angular velocity

### Subscripts

cr	refers to condition when $\theta = \theta_{cr} = \beta_s$
o	initial value
p	projectile
r	refers to relative angular velocity
s	sphere (ball obturator)

$x,y,z$  refers to inertial coordinate system

$1,2,3$  refers to body-fixed coordinate system

Superscripts

- denotes differential with respect to time

## ACKNOWLEDGEMENT

In the course of this research there were many persons who were extremely helpful in their kind and timely assistance. I would like to express my appreciation to Mr. Tom Christian, Mr. Ken Mothersell, Mr. John Moulton and Mr. Ron Longueira for their assistance in my experimental efforts. I would like to thank Mrs. Vicky Culley and the clerical staff of the Mechanical Engineering Department for their timely response and logistical support. The services provided by Mr. Roger Hilleary, Mr. Richard Donat and the operators on the evening shift at the W.R. Church Computer Center were invaluable in my research. The patience exhibited by Mr. Howard Bensch and his staff of the Educational Media Department Photo Lab in assisting with the preparation of photographs and motion pictures was tremendous. The unselfishness of Professors Brock, Cantin, Newton, Pucci, Salinas, Marto, and Vanderplaats in providing expert guidance upon request is deeply appreciated. The constant support provided by Commanders Neyman and Garritson and their lovely secretary, Mrs. Carol Alejo was instrumental in the successful completion of this research.

I want to express my deepest appreciation to Professor Robert H. "Bud" Nunn for his tireless support and long hours in the development of the linear approximation and assistance in data correlation. I am grateful for his constant regard

for feelings and the understanding that comes from caring and concern for others. Professor Nunn's ability to be professional and personable is a rare gift and I thank him for sharing it with me. Words are not enough to express my thanks to God for the gift of my loving wife Mary. She has been with me and for me through it all. Her love and understanding made the most difficult times easier and helped our beautiful children, Jimmy, Christy and John Michael, to remain close even though the time we spent together was short. I thank her for her decision to love me.

## I. INTRODUCTION

### A. BACKGROUND

The tubular projectile is not a new concept. As early as 1858, the usefulness of tubular projectiles was recognized for specific purposes. In that year, Joseph Whitworth (Whitworth Threads) wrote about and included an illustration of the tubular projectile in the section on Rifled Firearms of his Miscellaneous Papers on Mechanical Subjects [1]<sup>1</sup>. The projectile pictured was hexagonal with a circular hole. Whitworth noted its particular "...effectiveness in perforating elastic materials which prevented them from closing up." The projectile utilized a wooden sabot. Whitworth also said that the tubular projectile penetrated deeper into masonry than any he was acquainted with.

The Krnka-Hebler projectile was the next projectile referenced chronologically [2]. According to Charters and Thomas, this projectile was reported in the Allgemeine Schweizerische Militarzeitung as having been so successful that the Ordnance Department in the United States carried out firing tests of caliber .30 tubular projectiles in 1894. A description of those test firings and an updating of the results was performed by I.E. Segal and included in Ref. 2. In the 1894 tests, a vulcanized fiber sabot was used to push the projectile out the barrel.

---

<sup>1</sup>Numbers appearing in brackets refer to the list of references.

The purpose of the 1894 test was to compare trajectories of standard and tubular projectiles. This was done by comparing the vertical drop on target at a given range.

Segal's report in Ref. 2 indicates that the drag coefficients computed from the 1894 results agree closely with those of Charters and Thomas [2], even though their report was published fifty years later (1944) and their experimental apparatus was more sophisticated.

#### B. RECENT DEVELOPMENTAL STUDIES

The results obtained by independent researchers as to the value of the tubular projectile as an alternative to the conventional round are contradictory. It seems as if there was as much research devoted to discrediting the tubular projectile as there was to investigating its merits. Frank and McLaughlin [3] have accumulated a great deal of data from various sources in an attempt to "objectively compare" the merits of the tubular and "conventional shapes". The authors concluded that the tubular has no particular advantages over "well designed" conventional projectile shapes.

Their findings disagree with most of those discussed in the following sections.

##### 1. Range Tests

Winchenbach, Daniel and Edgar [4] conducted range tests of six configurations of tubular projectiles and concluded that the drag coefficients were significantly lower

than the standard High Explosive Incendiary (HEI) projectile of the same caliber. Only projectiles of the same bore size were compared. The experimental models were constructed from standard 20-mm ammunition by boring various hole sizes to obtain ". . . area ratios ( $A_t/A_i$ ) of 0.7, 0.8, 0.9 and 1.0." Where  $A_t$  is the throat area and  $A_i$  is the inlet area of the projectile. The drag coefficients of the projectiles with area ratios of 0.8, 0.9 and 1.0 were less than half that of the projectile with area ratio of 0.7. The higher drag coefficient was attributed to the underexpanded flow at the exit resulting in high base drag.

Range tests conducted for the concept evaluation of the 20-mm tubular projectile for the Vulcan Weapons System [5] showed that the tubular projectile performed better than the standard HEI round, with lower drag, shorter time of flight for a given range (30 percent shorter at 1000 meters, 40 percent shorter at 2000 meters) and similar dispersion characteristics on target.

Recent tests at the Naval Weapons Center, China Lake, California of the Ball Obturated Tubular Projectile (BOT) have shown a definite advantage in that the low drag of the tubular projectile means slower retardation of velocity and hence a higher terminal kinetic energy [6]. (The BOT is the object of this investigation and will be described in detail in later sections of this thesis.)

## 2. Target Impact Tests

The higher the energy delivered to the target, the greater the damage. Since kinetic energy is directly proportional to the first power of mass and to the square of the velocity, the reduced mass of the tubular projectile is compensated by a higher muzzle velocity and therefore a potential for higher kinetic energy. However, due to the improved drag characteristics, the reduction in mass to obtain the higher muzzle velocities may not be necessary, depending upon the imposed performance criteria.

Target impact studies have been carried out with various projectile configurations and target types. Rhethorst, et.al. [7] conducted impact studies of 7.62-mm tubular projectiles on helmets. Tests showed that even with the same energy, the tubular projectile penetrated further.

Kitchen and Keeser [8] conducted studies for the Air Force on the impact effectiveness of tubular projectiles on simulated aircraft fuel cells. These tests were conducted with steel and depleted uranium (DU) tubular projectiles and standard 20-mm HEI projectiles. The projectiles were fired at double panels at varying degrees of obliquity. Of the forty-seven tests of the steel tubular projectiles which impacted the target, twenty breached the rear panel up to angles of  $70^{\circ}$ . The DU projectiles breached the rear panel even at angles of  $85^{\circ}$  and fires were started in three of the five DU tests. The standard M56 HEI projectiles failed to

breach the rear panel in each of the five firings even though severe damage to the front panel and two fires occurred.

Brunsvold and Kalivretenos [9] conducted a program to test the effectiveness of the tubular projectile against a simulated cruise missile warhead. Tests were conducted with 20 and 40-mm rounds. Results of those tests are classified, and therefore not presented here. It was noted [9] that due to the improved stability characteristics of the tubular projectile, only half the spin rate need be imparted by the rifling in the barrel to obtain the same stability as a standard projectile, which indicates less barrel wear.

### 3. Weapons System Capability

For the tubular projectile to be practical, it must be able to interface with existing weapons systems. Reference 5 is a report of the 1978 tests conducted by the Army to evaluate the tubular projectile in the Vulcan weapons system.

Because the nose of the tubular projectile is flat compared to the standard projectile (See Fig. 1), it ". . . did not lend itself to chambering in the weapon." Personnel safety required that the weapon be remotely operated and therefore only the surface-to-surface performance comparison was made.

The dispersion on target improved for the tubular projectile from 700 to 2000 meters. The dispersion varied

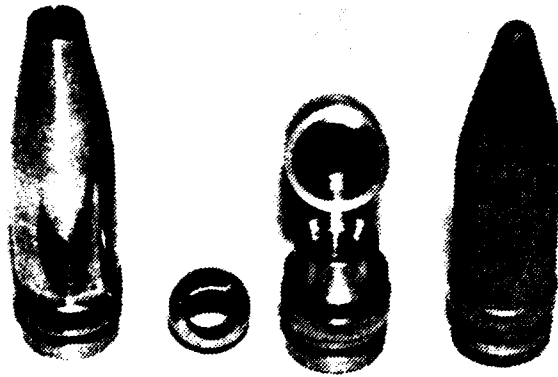


Figure 1. 20-mm Ball Obturated Tubular Projectile (BOT), components, and conventional 20-mm projectile. (Photograph courtesy of NWC, China Lake).

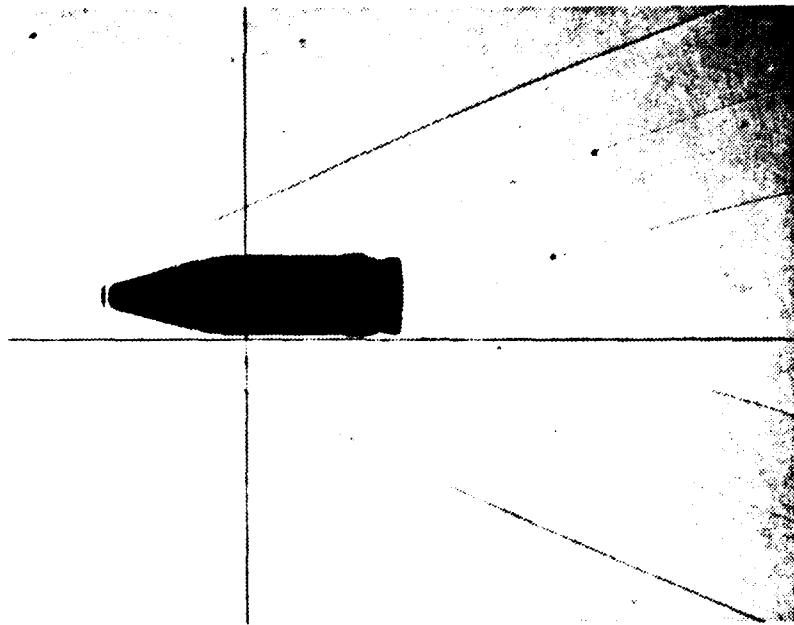


Figure 2a. Standard 20-mm projectile in flight with detached bow shock. (Photograph courtesy of NWC, China Lake).

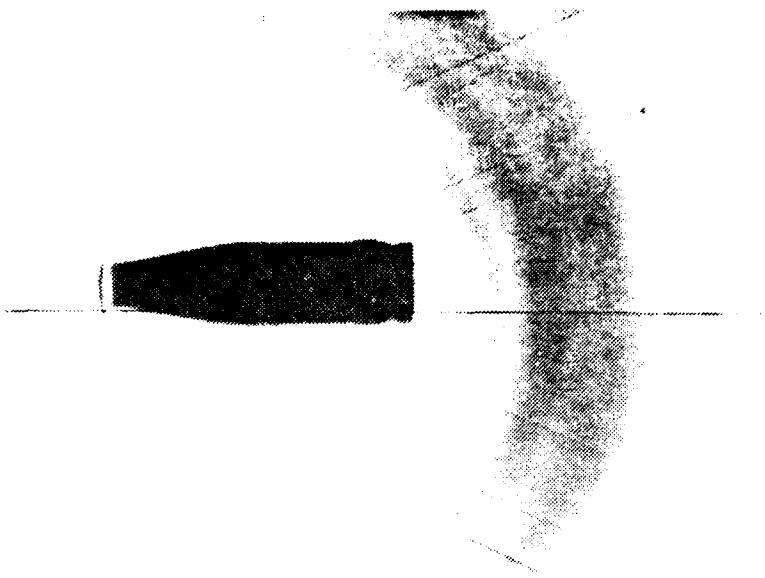


Figure 2b. BOT with passage blocked resulting in detached bow shock. (Photograph courtesy of NWC, China Lake).

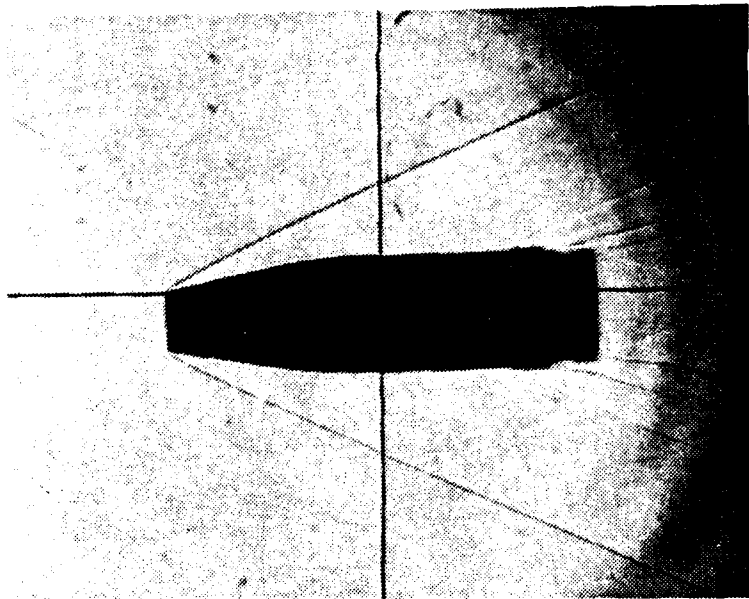


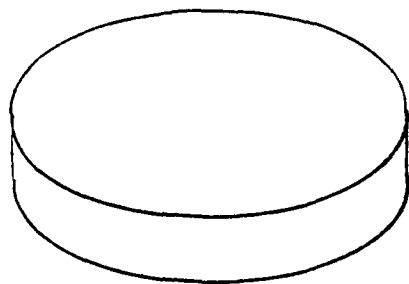
Figure 2c. BOT with no blockage in passage; only attached oblique shocks emanating from the lip of the projectile. (Photograph courtesy of NWC, China Lake).

on the average by only 0.2 mil over the entire range spectrum between the tubular and conventional HEI projectile. However, at 2000 meters, the tubular was better by 0.4 mil. The time of flight to target was another impressive finding in Ref. 5. The tubular projectile had a 30 percent shorter flight time at 1000 meters and a 40 percent shorter flight time at 2000 meters than the conventional HEI projectile.

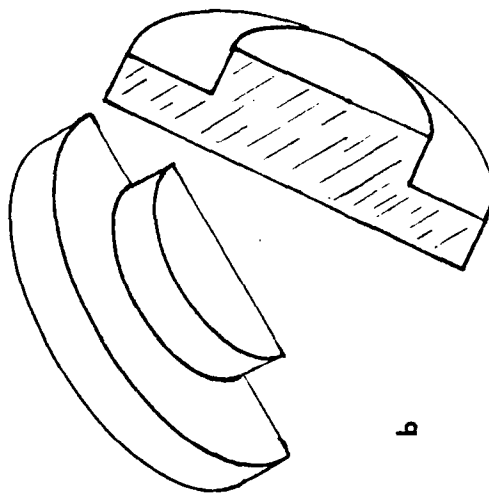
Results of firings of 25-mm and 30-mm tubular projectiles from the Oerlikin KBA and GAU-8/A respectively were reported in part in Ref. 3. Figures comparing Line-of-Sight Penetration Capability vs. Range for a conventional spinner configuration based on AR-2 shape, a finner configuration based on F10 shape, and a tubular projectile were shown. The tubular projectile was shown to be inferior in both instances. The report does not indicate the degree of compatibility the tubular configuration has with the guns used.

#### 4. Review Of Internal Shock Wave Considerations

From photographs of tubular projectiles in flight [4] and during wind tunnel testing [7], various shock patterns have been observed at the inlet region and in the wake. The photographs of Figs. 2a-c show the BOT and the conventional projectiles in flight. The sabots used in Refs. 4 and 7 were of the pusher type similar to those illustrated in Fig. 3. The detached bow shock seen in the photograph of the standard projectile (Fig. 2a) is similar to that of the tubular projectile shown in Fig. 2b with passage closed (and in Ref. 4



a



b

Figure 3. Solid (a) and Split (b) disk, pusher-type, discarding sabots/obturators.

with the sabot attached). With no blockage of the internal passage (Fig. 2c) there was no detached bow shock, with only attached oblique shocks emanating from the lip of the projectile. This latter case allows the possibility of four other internal flow/shock configurations.

- (1) A normal shock standing at the entrance to the projectile;
- (2) A normal shock standing at some intermediate position in the channel;
- (3) A system of oblique shocks present in the channel;
- (4) The channel is devoid of shocks and the flow is shock-free through the channel.

In each of the cases described, specific conditions must exist:

a. The Detached Bow Shock

When the projectile passage is closed, such as in the case of the attached sabot, the projectile acts as a blunt-nosed body with the resultant detached normal shock [10] (see Figs. 2a and b). From oblique shock theory, there is a maximum turning angle which the flow (supersonic) can negotiate through an attached oblique shock. When this turning angle is exceeded, the shock becomes normal and detaches. There have been many studies as to the strength and location of this detached bow shock, but here the internal flow is of more interest and, therefore, those references are not included in this discussion.

b. Normal Shock At The Entrance

From one-dimensional frictionless flow theory, for a given initial Mach number,  $M_1$ , the pressure ratio across a normal shock is given by:

$$\frac{P_2}{P_1} = \frac{(1 + \gamma M_1^2)}{(1 + \gamma M_2^2)} \quad (1)$$

for a perfect gas with constant specific heats.  $P_2$  is the pressure downstream of the normal shock,  $P_1$  the pressure upstream of the shock,  $M_2$  the downstream Mach number and  $\gamma$  the ratio of specific heats,  $C_p/C_v$ . This pressure ratio must exist in order for a normal shock to be formed. Kantrowitz and Donaldson [11] conducted experiments in which they concluded that the contraction-ratio in the entrance of a supersonic diffuser was important in reducing the kinetic energy losses. The studies done were on supersonic diffusers with varying areas. The formation of a normal shock at the entrance is determined by the throat area and initial Mach number such that the Mach number at the throat of the duct is exactly 1.0. The maximum value of the ratio of the capture (inlet) area,  $A_c$ , to throat area,  $A_t$ , required to allow the bow shock to be swallowed is given in Ref. 9 as:

$$\frac{A_c}{A_t} = \frac{1}{M_2} \left[ \frac{2}{\gamma+1} \left( 1 + \frac{\gamma-1}{2} M_2^2 \right) \right]^{\frac{\gamma+1}{2(\gamma-1)}} \quad (2)$$

where  $M_2$  may be obtained from tabulated values for normal shock waves for a given free stream Mach number,  $M_1$  or may be calculated from

$$M_2 = \left[ \frac{\frac{2}{(\gamma-1)} + M_1^2}{\frac{2\gamma}{(\gamma-1)} M_1^2 - 1} \right]^{\frac{1}{2}} \quad (3)$$

c. Normal Shock At An Intermediate Position

The formation and position of a normal shock at an intermediate position in a constant area duct has been theorized in the presence and absence of viscous effects. In the absence of viscous effects, the normal shock tends to grow from the interaction of oblique shocks and will be discussed under "d" below.

In the presence of friction, the formation of the boundary layer along the duct walls reduces the effective area of the duct [12, 13, 14]. This reduction has the effect of decelerating a supersonic flow as in a diffuser. In a constant area duct with friction, the location of a normal shock in the duct may be determined by Fanno Line Flow Theory. The length to diameter ratio, friction factor and initial Mach number determine the range of back pressures for which the duct will be "choked", or a normal shock set up [10].

For a given supersonic entrance Mach number, there exists a maximum value of  $fL/D$ ;  $f$ , being the Reynolds number-dependent friction factor,  $L$ , the length of the duct and  $D$ , the diameter of the duct. This maximum value, is the value

for which the duct will remain unchoked. If the actual value of  $fL/D$  is less than the maximum, the flow will remain unchoked if the back pressure is sufficiently low at the duct exit.

In the case of the tubular projectile, assuming a constant back pressure,  $L/D$  of (typically) 8.0 and  $Re$  in the range from approximately  $4 \times 10^5$  to  $6 \times 10^5$ , from Fig. 20.1 of Ref. 15,  $f$  is between 0.013 and 0.0125. Using an average value of  $f$  of 0.01275,

$$fL/D = 0.102$$

From Ref. 10, Appendix E, this corresponds to  $M \approx 1.41$ . Iterating to obtain better values of  $f$  from a revised average  $Re$  would increase the Mach number at which the projectile would choke. After one iteration the Mach number increases to  $M = 1.44$ . As  $L/D$  decreases,  $Re$  increases and  $f$  decreases resulting in a lower value of the Mach number at which the flow chokes.

#### d. System Of Oblique Shocks In The Duct

The formation of a system of oblique shocks in a duct or channel is the most difficult to explain and analyze. Ferri [16, 17] has developed an analytical solution for the shock structure utilizing the Method of Characteristics. The analysis becomes difficult if not impossible at the centerline of the duct because, according to Ferri, the oblique shock curves toward the centerline and becomes normal. The extent of the normal shock is dependent upon geometry and flow

conditions. The larger the wedge angle for a given Mach number, the stronger and larger the normal shock at the centerline. The constant area duct implies a zero internal deflection angle. In this instance, Ferri's analysis, which ignores viscous effects, implies that no normal shock is formed (Fig. 13 of Ref. [16]). With no wedge angle, there is no oblique shock formed.

Brunsvold and Kalivretenos [9] have modified a Method of Characteristics computer code [18] developed for supersonic inlets to account for the absence of a center-body on the tubular projectile. This modified code was then coupled with a subroutine to calculate the internal wave drag coefficient based on  $A_c$  and used to obtain an optimum internal geometry for the tubular projectile which would give minimum internal wave drag. The computer code assumes inviscid, supersonic flow throughout. Reference 9 states that some inaccuracies are allowed in the computation due to the relaxation of the convergence of the characteristics equations at the centerline, but that the inaccuracies do not have time to propagate to the walls of the projectile before the exit plane. Therefore, the inaccuracies do not affect the wall pressure distribution.

Rhethorst, et.al. [19] has postulated another method for determining the shock structure and the resultant internal wave drag for a tubular projectile, using Prandtl-Meyer wave theory. But again the initial oblique shock

formation is dependent upon the wedge angle at the entrance and therefore does not apply to the constant area duct case where no internal wedge angle exists. Ferri [16, 17], Brunsvold and Kalivretenos [9] and Rhethorst, et.al. [19] have neglected boundary layer/shock wave interaction.

Fejer, et.al., [14] and Waltrup and Billig [15] have conducted experiments utilizing constant area ducts. Fejer, et.al., performed experiments on constant area rectangular ducts varying in lengths, whereas Waltrup and Billig conducted their experiments on cylindrical ducts of varying lengths and diameters. Other than the obvious geometry differences, the procedures were very similar. The advantage of the rectangular duct was the ability to visualize the shock patterns through a viewing port, whereas the curvature of the walls of the cylindrical duct precluded accurate visualization.

In both experiments, oblique shock systems were formed in the ducts. The location of the shock system in the duct and the actual configuration of the shock system was controlled by the pressure ratio. The pressure ratios were controlled in different ways, but the effects were the same. As back pressure increased, a shock system formed at the exit of the duct. With further increases in back pressure the system of shocks moved upstream and out of the duct and a detached shock appeared. Shapiro [12] indicates that internal oblique shocks may be the remnants of normal shocks "with

bifurcated ends as a result of boundary layer separation." He states that the normal portion grows shorter as the boundary layer gets thicker until the normal portion disappears completely leaving only the bifurcated portion. He illustrates this in Fig. 28.27(c) of Ref. 12. This explains the movement of the oblique system toward the entrance of the duct in the experiments of Refs. 14 and 15. As back pressure increases, the flow downstream of an internal shock has more of a tendency to separate. Fejer also states that the presence of a turbulent boundary layer had a stabilizing effect on the shock system in the constant area rectangular duct. In the experiments involving the cylindrical duct, the shock structure again moved from exit toward entrance with back pressure increases. They also report a breakdown in flow downstream of the shock system as indicated by relatively constant pressure movements in this region.

e. No Shocks Present In The Duct

It can be seen from previous discussion that given an initial Mach number and inlet stagnation pressure, a sufficiently high back pressure will cause a normal shock or system of oblique shocks to be formed. If the cross-sectional area of the duct is reduced in the direction of flow, as in a supersonic diffuser, the incident flow may cause an oblique compression wave to be formed. In the absence of the requisite back pressure or area reduction,

no explanations for internal shock formation have been found other than those due to viscous effects noted in "d" above.

f. Summary

In a constant area duct with supersonic inlet flow, there is a pressure rise caused by a reduction in the effective flow area by boundary layer formation due to friction. Depending upon the length-to-diameter ratio (L/D) of the duct and the flow parameters, the increase in pressure ratio (or reduction in Mach number) required to cause formation of a system of oblique shocks is less than that required to set up a normal shock at the duct entrance. This difference is explained by the boundary layer formation and/or interaction with the shock waves.

In the case of the tubular projectile, the back pressure at the exit in flight is affected by the complex wake flow. There is no pressure difference in the surrounding medium at large distances from the projectile. The formation of shock waves inside the projectile with a constant cross section is due to viscous effects and depends upon Mach number and the length-to-diameter ratio.

5. Laboratory/Wind Tunnel Testing

From all indications, the Weapons System Concept Team (WSCT) of ARRADCOM has done extensive wind tunnel testing on various tubular projectile configurations. The work of A. Flateau of the Weapons System Concept Office is referenced often with regard to results obtained, however no

publications from that office have been found. (The work referenced in other publications is usually of the "private communication" type.) Appendix D of Ref. 8 reports results of a test conducted by the WSCT at the ARRADCOM facility. The facility utilizes a variable Mach number tunnel which may be used to simulate the deceleration of the projectile in flight.

The results of Ref. 8 agree closely to those of Ref. 7, in that the drag coefficient rises almost instantaneously at the Mach number at which the flow becomes choked.

The Mach number at which this choking occurs is dependent upon geometry. For the case of inviscid flow, Brunsvold and Kalivretenos [9] give the following relation for the area ratio corresponding to the free stream Mach number at which the shock is "regurgitated" and the flow becomes choked:

$$\frac{A_c}{A_t} = \frac{1}{M_1} \left[ \frac{2}{\gamma+1} \left( 1 + \frac{\gamma-1}{2} M_1^2 \right) \right]^{\frac{\gamma+1}{2(\gamma-1)}} \quad (4)$$

#### C. PURPOSE OF STUDY

The results of tests and experiments previously mentioned show for the most part definite advantages to the tubular projectile over the conventional projectile primarily in the area of lower drag (approximately 1/2 to 1/3 of conventional [8])

which allows a flatter trajectory and shorter time of flight for a given range [5]. With the emphasis on Anti-Missile Defense both from a Surface-to-Air and Air-to-Air standpoint, these features are definitely worth further study.

The problem seen from the air platform is that of the discarding sabot or pusher. The solid [4, 5, 7] or split [8] disk is effective and reliable, however the possibility of ingestion in the aircraft engines prohibits their use. Rhethorst et.al. in Ref. 7 illustrates a number of sabot/obturator designs for use with the tubular projectile, but these are also of the discarding type. They also investigated the possibility of using a consumable sabot [19] which would be burned up as the projectile was transiting the barrel and would be completely consumed as it exited the barrel. The most recent development has been the BOT which was designed at NWC China Lake, California [6]. The ball obturator has been bored with a hole the same diameter as the hole through the projectile. When loaded, the ball is supported inside the projectile such that the axis through the hole in the ball makes an angle of approximately  $90^\circ$  with the axis of the hole through the projectile (see Fig. 4).

Gas pressure from the burning propellant holds the ball obturator fixed with respect to the projectile as the rifling in the barrel imparts spin to the projectile (as well as the ball). Upon exiting the barrel, the propellant gas pressure

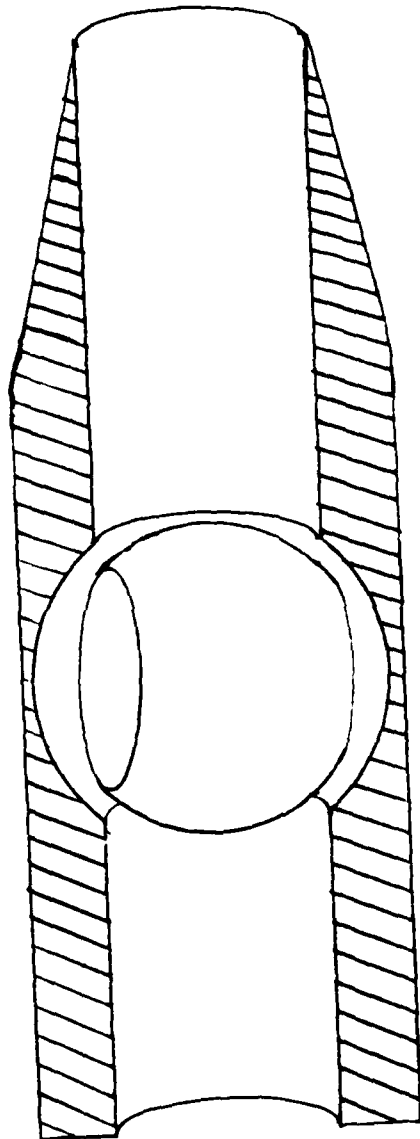


Figure 4. BOT with obturator oriented to block the passage (loading position).

is released. At that time a complex force distribution acts on the ball to cause it to change position inside the projectile in such a way as to align the holes. Inertial forces then dominate to maintain this alignment so that the projectile remains fully tubular. There are no separating parts and the opening process is automatic.

The purpose of this research is to analytically predict the motion of the ball obturator as a function of time. In support of this purpose, an experimental apparatus was designed and built to simulate the motion of the obturator in order to gain physical evidence of the accuracy of the model.

## II. ANALYSIS

### A. DEVELOPMENT AND SOLUTION OF THE EQUATIONS OF MOTION

The ball obturator may be thought of as a rigid body of rotation with a system of coordinate axes fixed to the ball having its origin at the mass center of the ball (Fig. 5). These axes will be designated  $x$ ,  $y$ , and  $z$ , where  $z$  is the axis through the hole in the ball.

The motion of the ball must be described relative to the projectile, and for this purpose an inertial frame of reference is defined with axes designated  $X$ ,  $Y$  and  $Z$  with its origin also at the mass center of the ball. For this analysis it is assumed that the projectile has only a rotation about the  $Z$ -axis and no translation or other rotation. Because only the motion of the ball with respect to the projectile is desired at this point, the relative velocities are the quantities desired. The ball has only rotational components and thus the values of angular velocity with respect to the  $X$  and  $Y$  axes are also relative to the projectile, whereas the value with respect to the  $Z$ -axis must account for the projectile spin.

By doing this, the motion may be described by Euler's Modified Equations of Motion for a rigid body of revolution about a fixed point. These are given in Thomson [20] as:

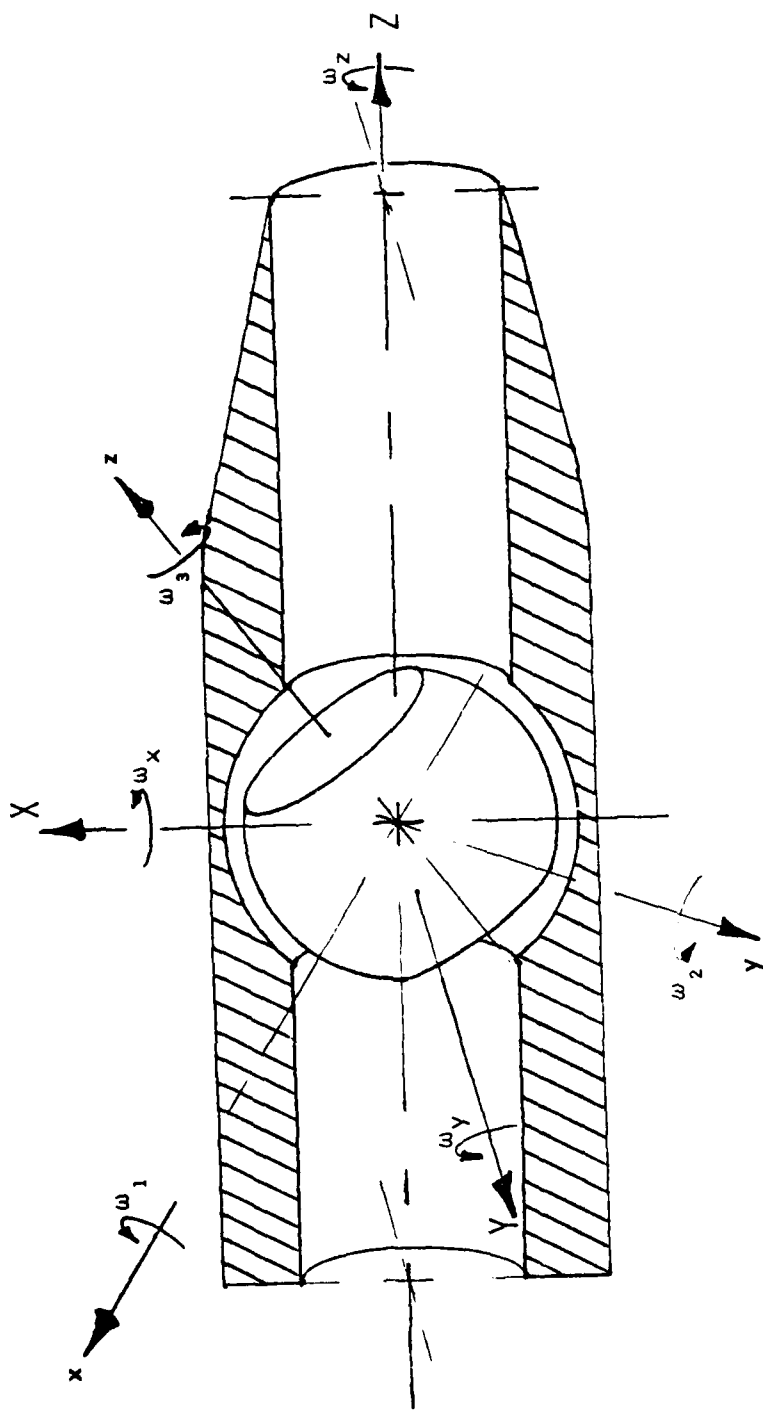


Figure 5. BOT showing orientation of coordinate axes.

$$A\dot{\omega}_1 + (C-A)\omega_2\omega_3 = G_1 \quad (5a)$$

$$A\dot{\omega}_2 + (A-C)\omega_1\omega_3 = G_2 \quad (5b)$$

$$C\dot{\omega}_3 = G_3 \quad (5c)$$

where

A = Mass moments of inertia about principal axes perpendicular to the z-axis.

C = Mass moment of inertia about the principal axis through the hole (z-axis).

$\dot{\omega}_1, \dot{\omega}_2, \dot{\omega}_3$  = Angular accelerations about the body fixed axes x, y, z respectively.

$\omega_1, \omega_2, \omega_3$  = Angular velocities about the body fixed axes.

$G_1, G_2, G_3$  = Moments acting about the body fixed axes.

Since a body of revolution has only two distinct principal axes, the mass moments of inertia about the x and y axes are equal. The moments of inertia of the ball were determined by first finding the inertia tensor. From Refs. 21 and 22 the inertia tensor is found by starting with the formulation for a hollow cylinder of inside radius r and length 2h (Fig. 6) in which the inertia tensor in terms of dyadics is

$$I = (U + \underline{ee})mr^2/2 + (U - \underline{ee})mh^2/3 \quad (6)$$

In Eq. (6) m is the mass of the cylinder (ball), U is the unit dyadic and  $\underline{ee}$  is the referenced dyad. Using Fig. 6 as a guide, the incremental value of the inertia tensor with respect to the center of mass,  $dI_G$  is given by:

$$( h = \sqrt{R^2 - \rho^2} )$$

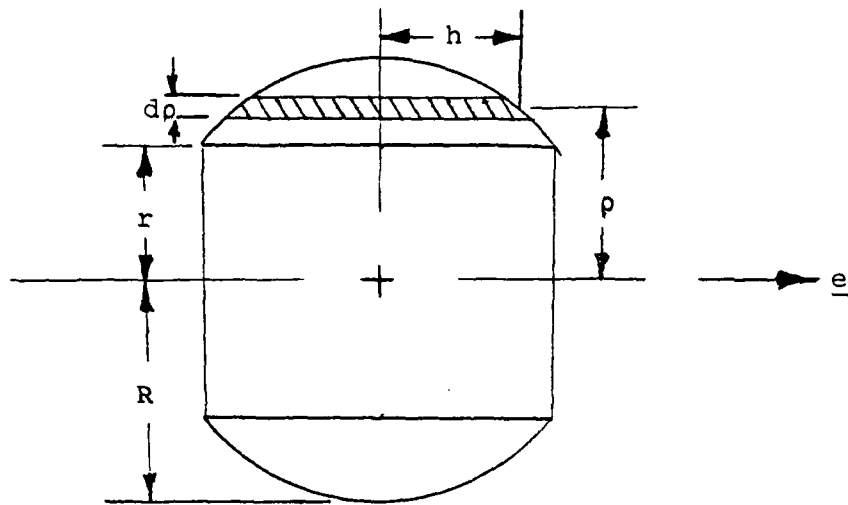


Figure 6. Dimensional relationships for calculating the inertia tensor and moments of inertia.

$$dI_G = (U + \underline{ee})\rho^2/2 \, dm + (U - \underline{ee})h^2/3 \, dm \quad (7)$$

where  $\rho$  is the radial distance to the incremental mass,  $dm$ .

The incremental mass is given by

$$dm = 4\pi\rho(R^2-\rho^2)^{\frac{1}{2}} \gamma d\rho \quad (8)$$

From Eq. (7), since the origin and center of mass coincide,

$$I_O = \int dI_G \quad (9a)$$

therefore,

$$I_O = \int_r^R (U+\underline{ee}) 2\rho^3 \pi \gamma d\rho + \int_r^R (U-\underline{ee}) \frac{h^3}{3} 4\pi\rho\gamma d\rho \quad (9b)$$

which, after simplification leaves

$$I_O = 2\pi\gamma(U+\underline{ee}) \int_r^R \rho^3 (R^2-\rho^2)^{\frac{1}{2}} d\rho + \quad (9c)$$

$$\frac{4}{3}\pi\gamma(U-\underline{ee}) \int_r^R (R^2-\rho^2)^{\frac{3}{2}} \rho d\rho$$

Solving Eq. (9c) gives

$$I_O = \pi\gamma \left\{ 2(U+\underline{ee}) \left[ \frac{1}{5}r^2 + \frac{2}{15}R^2(R^2-r^2)^{\frac{3}{2}} \right] + \right. \quad (9d)$$

$$\left. \frac{4}{3}(U-\underline{ee}) \left[ \frac{1}{5}(R^2-r^2)^{\frac{5}{2}} \right] \right\}$$

Eq. (9d) is the expression for the second order inertia tensor of the ball obturator with outside radius  $R$ , hole radius  $r$  and made of a material of density  $\gamma$ . Diadics have been used to describe this tensor. In order to obtain the moments of inertia about any axis, the diadic describing the tensor need only be premultiplied and postmultiplied by scalar multiplication by the unit vector along the axis about which the moment of inertia is described. It may be seen in Fig. 6 that the  $e$ -direction vector is along the  $z$ -axis. The  $e$ -direction may be chosen arbitrarily, however this choice greatly simplifies the formulation of the integral. Thus the moment of inertia about the  $z$ -axis,  $C$ , is given by

$$C = \underline{e} \cdot [(\underline{ii} + \underline{jj} + \underline{ee}) + \underline{ee}] \cdot \underline{e} \left\{ \left[ 2\pi\gamma \left( \frac{1}{5}r^2 + \frac{2}{15}R^2 (R^2 - r^2) \right)^{3/2} \right] \right. \\ \left. + \frac{4}{3}(\underline{ii} + \underline{jj} + \underline{ee} - \underline{ee}) \left[ \pi\gamma \frac{1}{5} (R^2 - r^2) \right]^{5/2} \right\} \quad (10a)$$

Simplifying and using the subscript  $s$  to denote particular values for the ball obturator:

$$C = 4\pi\gamma \left( \frac{1}{5}r_s^2 + \frac{2}{15}R_s^2 \right) (R_s^2 - r_s^2)^{3/2} \quad (10b)$$

For the axes perpendicular to  $\underline{e}$  through the mass center, the Moment of Inertia is given by

$$A = B = \underline{j} \cdot \underline{I}_G \cdot \underline{j} = \underline{i} \cdot \underline{I}_G \cdot \underline{i} \quad (11a)$$

Performing steps as in Eqs. (10) gives

$$A = j \cdot (\underline{ii} + \underline{jj} + \underline{ee} + \underline{ee}) \cdot j \left[ 2\pi\gamma \left( \frac{1}{5}r^2 + \frac{2}{15}R^2(R^2 - r^2) \right)^{3/2} \right] \\ + j \cdot (\underline{ii} + \underline{jj} + \underline{ee} - \underline{ee}) \cdot j \left[ \pi\gamma \frac{4}{15} (R^2 - r^2)^{5/2} \right] \quad (11b)$$

After premultiplying and postmultiplying,

$$A = \pi\gamma \left\{ 2 \left[ \frac{1}{5}r_s^2 + \frac{2}{15}R_s^2(R_s^2 - r_s^2) \right]^{3/2} + \frac{4}{15}(R_s^2 - r_s^2)^{5/2} \right\} \quad (11c)$$

In order to simplify Eqs. (5), define a non-dimensional  $\lambda$  such that

$$\lambda = \frac{C-A}{A} \quad (12)$$

Thus Eqs. (5) becomes

$$\dot{\omega}_1 + \lambda \omega_2 \omega_3 = G_1/A \quad (5a)$$

$$\dot{\omega}_2 + \lambda \omega_1 \omega_3 = G_2/A \quad (5b)$$

$$\dot{\omega}_3 = G_3/C \quad (5c)$$

The position of the ball at any time may be described by three angles,  $\theta$ ,  $\phi$  and  $\psi$ . These are known as the Euler angles and their relationships to the coordinate axes already described may be seen in Fig. 7. Reference 20 defines  $\omega_1$ ,  $\omega_2$  and  $\omega_3$  in terms of the Euler angles as

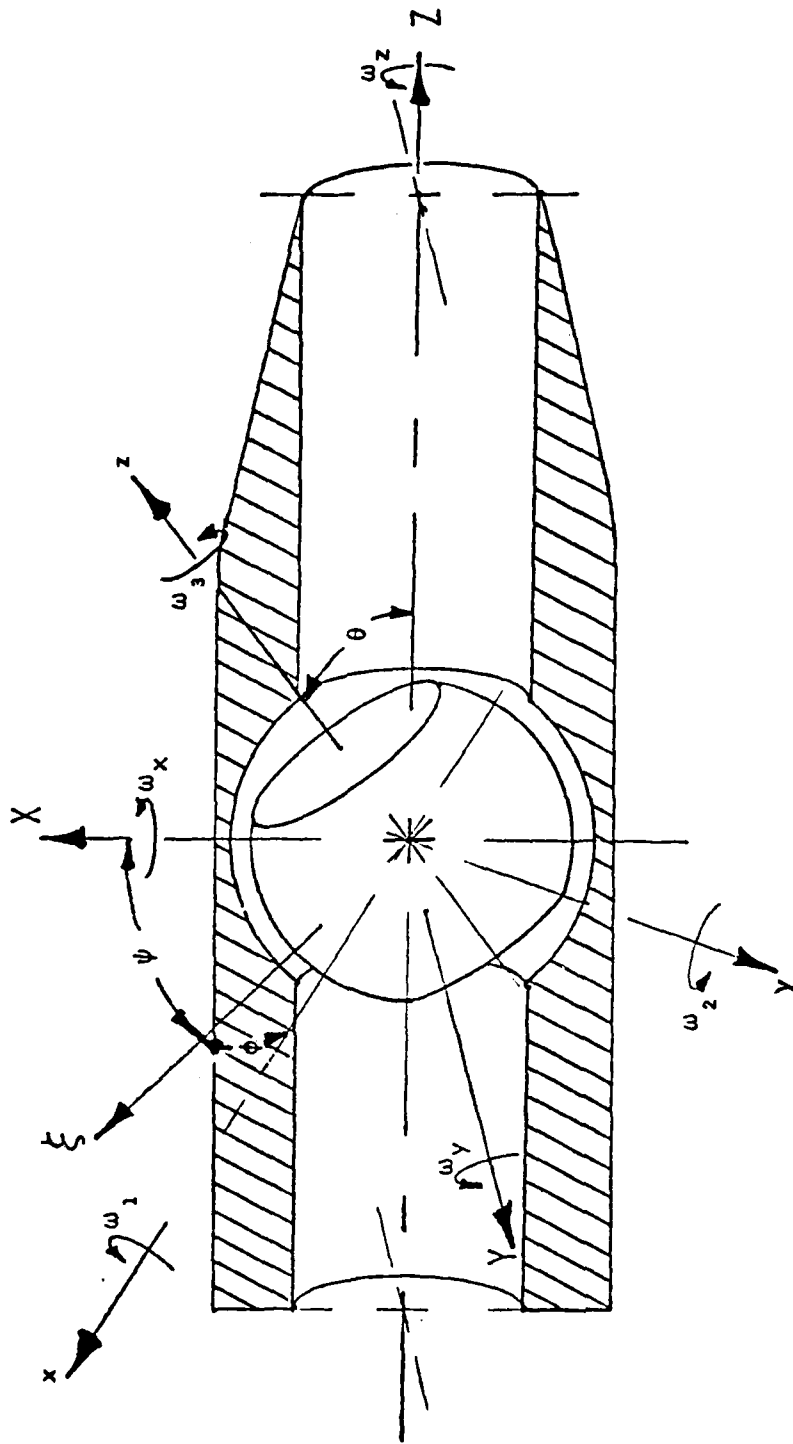


Figure 7. Relationship of Euler Angles,  $\theta$ ,  $\psi$  and  $\phi$  to the coordinate axes. ( $\zeta$  is the nodal axis in the  $x$ - $Y$  plane).

$$\omega_1 = \dot{\psi} \sin \theta \sin \phi + \dot{\theta} \cos \phi \quad (13a)$$

$$\omega_2 = \dot{\psi} \sin \theta \cos \phi - \dot{\theta} \sin \phi \quad (13b)$$

$$\omega_3 = \dot{\phi} + \dot{\psi} \cos \theta \quad (13c)$$

By differentiating Eqs. (13) with respect to time,  $\dot{\omega}_1$ ,  $\dot{\omega}_2$ , and  $\dot{\omega}_3$  may be obtained as

$$\begin{aligned} \dot{\omega}_1 = & \ddot{\psi} \sin \theta \sin \phi + \dot{\psi} (\dot{\theta} \cos \theta \sin \phi + \dot{\phi} \sin \theta \cos \phi) + \ddot{\theta} \cos \phi \\ & - \dot{\theta} \dot{\phi} \sin \phi \end{aligned} \quad (14a)$$

$$\begin{aligned} \dot{\omega}_2 = & \ddot{\psi} \sin \theta \cos \phi + \dot{\psi} (\dot{\theta} \cos \theta \cos \phi - \dot{\phi} \sin \theta \sin \phi) - \ddot{\theta} \sin \phi \\ & - \dot{\theta} \dot{\phi} \cos \phi \end{aligned} \quad (14b)$$

$$\dot{\omega}_3 = \ddot{\phi} + \ddot{\psi} \cos \theta - \dot{\psi} \dot{\theta} \sin \theta \quad (14c)$$

By substituting Eqs. (13) and Eqs. (14) into Eqs. (5), the following expressions for  $G_1/A$ ,  $G_2/A$  and  $G_3/C$  are found to be

$$\begin{aligned} & \ddot{\psi} \sin \theta \sin \phi + \dot{\psi} (\dot{\theta} \cos \theta \sin \phi + \dot{\phi} \sin \theta \cos \phi) + \ddot{\theta} \cos \phi - \\ & \dot{\theta} \dot{\phi} \sin \phi + \lambda (\dot{\psi} \sin \theta \cos \phi - \dot{\theta} \sin \phi) (\dot{\psi} \cos \theta + \dot{\phi}) = G_1/A \end{aligned} \quad (15a)$$

$$\begin{aligned} & \ddot{\psi} \sin \theta \cos \phi + \dot{\psi} (\dot{\theta} \cos \theta \cos \phi - \dot{\phi} \sin \theta \sin \phi) - \ddot{\theta} \sin \phi - \\ & \dot{\theta} \dot{\phi} \cos \phi - \lambda (\dot{\psi} \sin \theta \sin \phi + \dot{\theta} \cos \phi) (\dot{\psi} \cos \theta + \dot{\phi}) = G_2/A \end{aligned} \quad (15b)$$

$$\ddot{\psi} \cos \theta - \dot{\psi} \dot{\theta} \sin \theta + \ddot{\phi} = G_3/C \quad (15c)$$

Transforming this system of differential equations into the matrix form  $[A] \{X\} = [B]$  leaves

$$\begin{bmatrix} \sin\theta\sin\phi & 0 & \cos\phi \\ \sin\theta\cos\phi & 0 & -\sin\phi \\ \cos\theta & 1 & 0 \end{bmatrix} \begin{Bmatrix} \dot{\psi} \\ \dot{\phi} \\ \dot{\theta} \end{Bmatrix} = \begin{bmatrix} G_1/A - \dot{\psi}(\dot{\theta}\cos\theta\sin\phi + \dot{\phi}\sin\theta\cos\phi) \\ G_2/A - \dot{\psi}(\dot{\theta}\cos\theta\cos\phi - \dot{\phi}\sin\theta\sin\phi) \\ G_3/C + \dot{\psi}\dot{\theta}\sin\theta \\ + \dot{\theta}\dot{\phi}\sin\phi - \lambda(\dot{\psi}\sin\theta\cos\phi - \dot{\theta}\sin\phi)(\dot{\psi}\cos\theta + \dot{\phi}) \\ + \dot{\theta}\dot{\phi}\cos\phi + \lambda(\dot{\psi}\sin\theta\sin\phi + \dot{\theta}\cos\phi)(\dot{\psi}\cos\theta + \dot{\phi}) \end{bmatrix} \quad (16)$$

By premultiplying both sides of Eq. (16) by the inverse of the coefficient matrix, we are left with

$$\begin{Bmatrix} \dot{\psi} \\ \dot{\phi} \\ \dot{\theta} \end{Bmatrix} = \begin{bmatrix} \frac{\sin\phi}{\sin\theta} & \frac{\cos\phi}{\sin\theta} & 0 \\ \frac{\sin\phi\cos\theta}{\sin\theta} & \frac{-\cos\theta\cos\phi}{\sin\theta} & 1 \\ \cos\phi & -\sin\phi & 0 \end{bmatrix} \begin{bmatrix} G_1/A - \dot{\psi}(\dot{\theta}\cos\theta\sin\phi + \dot{\phi}\sin\theta\cos\phi) \\ G_2/A - \dot{\psi}(\dot{\theta}\cos\theta\cos\phi - \dot{\phi}\sin\theta\sin\phi) \\ G_3/C + \dot{\psi}\dot{\theta}\sin\theta \\ + \dot{\theta}\dot{\phi}\sin\phi - \lambda(\dot{\psi}\sin\theta\cos\phi - \dot{\theta}\sin\phi)(\dot{\psi}\cos\theta + \dot{\phi}) \\ + \dot{\theta}\dot{\phi}\cos\phi + \lambda(\dot{\psi}\sin\theta\sin\phi + \dot{\theta}\cos\phi)(\dot{\psi}\cos\theta + \dot{\phi}) \end{bmatrix} \quad (17)$$

In order to solve this system of non-linear second order, differential equations for  $\theta$ ,  $\phi$  and  $\psi$ , the following must be known:

Initial Values (denoted by subscript 0) of  $\theta$ ,  $\phi$ ,  $\psi$ ,  $\dot{\theta}$ ,  $\dot{\phi}$  and  $\dot{\psi}$  and the quantities, A, C,  $G_1$ ,  $G_2$  and  $G_3$ .

Due to symmetry,  $0^\circ \leq \theta \leq 90^\circ$ , and since we are interested in the performance of the ball away from  $0^\circ$ ,  $\theta_0 > 0$ . Since the ball is attached to the projectile initially (no slippage),  $\dot{\theta}_0 = \dot{\phi}_0 = 0$ .  $\dot{\psi}_0$  is equal to the spin rate of the projectile as it exits the barrel. A and C are physical constants dependent upon geometry and material properties [Eqs. (10) and (11)] and therefore  $\lambda$  is a constant.  $\phi_0$ , and  $\psi_0$  are arbitrary due to symmetry and the values of  $G_1$ ,  $G_2$  and  $G_3$  must be determined from knowledge of forces acting on the ball.

The solution to the problem of the motion of an axisymmetric rigid body about a fixed point with no moments applied is well known [20,21,22,23]. Under these conditions there is no nutation and the precession rate  $\dot{\psi}$  is constant.

Thus

$$\dot{\theta} = 0$$

and

$$\dot{\psi} = \frac{C\dot{\phi}}{(A-C)\cos\theta} \quad (18)$$

The computer solution method was tested by substituting the projectile spin velocity for  $\dot{\psi}$  in Eq. (18) and calculating  $\dot{\phi}$  for the specified value of  $0 < \theta_0 < 90^\circ$ . By inserting these values of  $\theta_0$ ,  $\dot{\psi}$  and  $\dot{\phi}$  into the computer model, and solving for  $\theta$  as a function of time,  $\dot{\theta}$  was indeed found to be zero. In addition, all other criteria for the test case, i.e., constant angular momentum and constant  $\dot{\psi}$  and  $\dot{\phi}$  were met.

The problem remaining is one of modeling the forces acting on the ball in order to determine  $G_1$ ,  $G_2$  and  $G_3$ .

## B. MODELING OF THE APPLIED TORQUES

### 1. Moments Due To Viscous Effects

Without the influence of applied forces or moments, the angular momentum remains constant or, from first principles:

$$\vec{M} = \dot{\vec{h}} = 0 \quad (19)$$

In order for the ball to nutate to the position in which the holes are aligned, a moment must be applied. This resultant torque is due to both viscous and sliding frictional forces.

The first attempt was to model the torque on the ball as that due to laminar Couette flow of a viscous fluid between two flat plates where the shear stress is given by

$$\tau = \mu_f \frac{\partial u}{\partial y} \quad (20)$$

The solution of the Navier-Stokes equations for this flow is well known and given by

$$\frac{dP}{dx} = \mu_f \frac{d^2 u}{dy^2} \quad (21)$$

where  $dP/dx$  is the pressure gradient in the direction of flow and, for our calculations, is assumed to be zero. The

governing partial differential equation is then

$$\frac{d^2u}{dy^2} = 0 \quad (22)$$

By considering the relative velocity, one plate is held fixed while the other has velocity of magnitude  $\omega_r \bar{r}$ .  $\omega_r$  is the relative angular velocity about the instantaneous axis of rotation and  $\bar{r}$  is the perpendicular distance from the instantaneous axis to the point at which the velocity is desired.

The boundary conditions are therefore given as

$$\begin{aligned} u &= -\omega_r \bar{r} \quad \text{at } y = 0 \\ u &= 0 \quad \text{at } y = h \end{aligned} \quad (23)$$

where  $y=0$  is the surface of the ball and  $h$  is the gap width between ball and projectile. Integrating Eq. (22) twice and applying the boundary conditions Eq. (23) gives

$$u(y) = -\omega_r \bar{r} (1-y/h) \quad (24)$$

Thus from Eqs. (20) and (24), the viscous shear stress at the surface of the ball, or at  $y=0$  becomes

$$\tau_0 = \mu_f \frac{\omega_r \bar{r}}{h} \quad (25)$$

The force due to viscous shear on the ball is given by the integral over the surface area of the ball of the shear stress Eq. (25), or

$$F_V = \int_A \tau_o dA. \quad (26)$$

The differential area  $dA$  is given by

$$dA = 2\pi R_s (R_s \sin\alpha d\alpha) \quad (27)$$

which is shown in Fig. 8.

Substituting Eqs. (25) and (27) into Eq. (26) gives

$$F_V = \frac{2\pi\mu_f R_s^2 \omega_r}{h} \int_0^\pi \bar{r} \sin\alpha d\alpha \quad (28)$$

The value of  $\bar{r}$  changes from 0 at the axis of rotation to  $R_s$  at  $\alpha=90^\circ$ . Thus

$$\bar{r} = R_s \sin\alpha \quad (29)$$

Substituting this expression into Eq. (28)

$$F_V = \frac{2\pi\mu_f R_s^3 \omega_r}{h} \int_0^\pi \sin^2\alpha d\alpha \quad (30)$$

The torque imparted to the ball is the force given by Eq. (30) multiplied by the moment arm at which it acts. Again, the moment arm is a function of  $R_s$  and  $\alpha$  and is given by  $R_s \sin\alpha$ . Substituting this into Eq. (30) gives an expression for the torque acting on the ball obturator due to

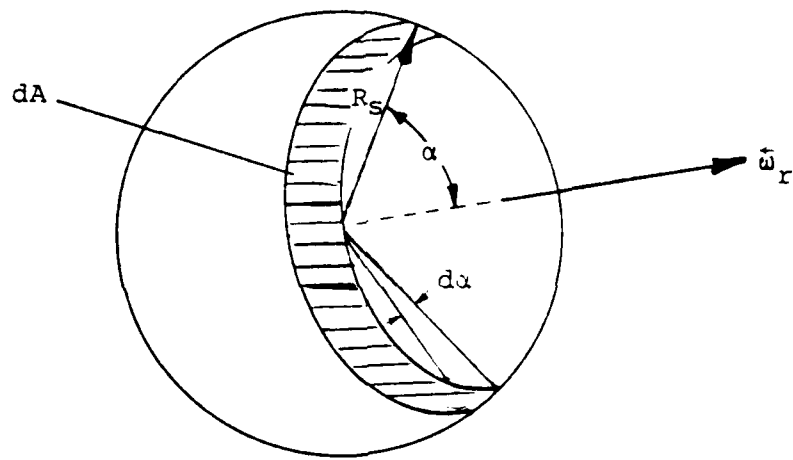


Figure 8. Differential area,  $dA$ , orientation with respect to the relative angular velocity vector,  $\omega_r$ .

the velocity of the ball relative to the projectile in a viscous medium, or

$$Q = \frac{2\pi\mu_f R_s^4 \omega_r}{h} \int_0^\pi \sin^3 \alpha d\alpha \quad (31)$$

Carrying out this integration gives

$$Q = \frac{8}{3} \frac{\pi R_s^4 \omega_r \mu_f}{h} \quad (32)$$

For a given geometry and constant fluid properties,  $\omega_r$  is the only variable in Eq. (32), therefore that portion of the expression which is multiplied by  $\omega_r$  will be called the shear constant, S, such that

$$\vec{Q} = S \vec{\omega}_r \quad (33)$$

where

$$S = \frac{8}{3} \frac{\pi R_s^4}{h} \mu_f \quad (34)$$

From the rigid body motion analysis, the relative angular velocity is easily determined. It is

$$\omega_r = [(\omega_1 - \omega_{p_1})^2 + (\omega_2 - \omega_{p_2})^2 + (\omega_3 - \omega_{p_3})^2]^{\frac{1}{2}} \quad (35)$$

where  $\omega_{p_1}$ ,  $\omega_{p_2}$  and  $\omega_{p_3}$  are the components of the projectile angular velocity about the axes fixed in the ball. These relationships are given in Thomson [20]

$$\omega_{p1} = \omega_p \sin\phi \sin\theta \quad (36a)$$

$$\omega_{p2} = \omega_p \cos\phi \sin\theta \quad (36b)$$

$$\omega_{p3} = \omega_p \cos\theta \quad (36c)$$

Equations (36) are simplified by the fact that  $\omega_p$  has only a component in the Z-direction of the inertial frame of reference.

The moments  $G_1$ ,  $G_2$  and  $G_3$  are obtained by applying Eq. (33) and resolving the moment vector into components about the x, y and z-axes. The motion of the ball may then be described fully by Eq. (17).

Figure 9 shows solutions for  $\theta$  as a function of time, using the Couette flow model with the following inputs:

$$\begin{aligned} R_s &= 7.62 \text{ mm (0.3 in.)} \\ r_s &= 4.7625 \text{ mm (0.1875 in.)} \\ h &= 0.0254 \text{ mm (0.001 in.)} \\ \rho &= 7800 \text{ Kg/m}^3 \text{ (0.282 lbm/in}^3\text{) (steel)} \\ \mu_{\text{air}} &= 1.92 \cdot 10^{-5} \text{ Pa-sec (4} \cdot 10^{-7} \text{ lbf-sec/ft}^2\text{)} \\ \omega_p &= 12042.77 \text{ rad/sec (1.15} \cdot 10^5 \text{ RPM)} \end{aligned}$$

It appears that viscous effects alone are not sufficient to cause the ball to nutate toward  $\theta=0$  in a rapid fashion. To check the model again, progressively larger orders of magnitude of S were input into the model. The effect, as expected, was to cause  $\theta$  to approach zero more

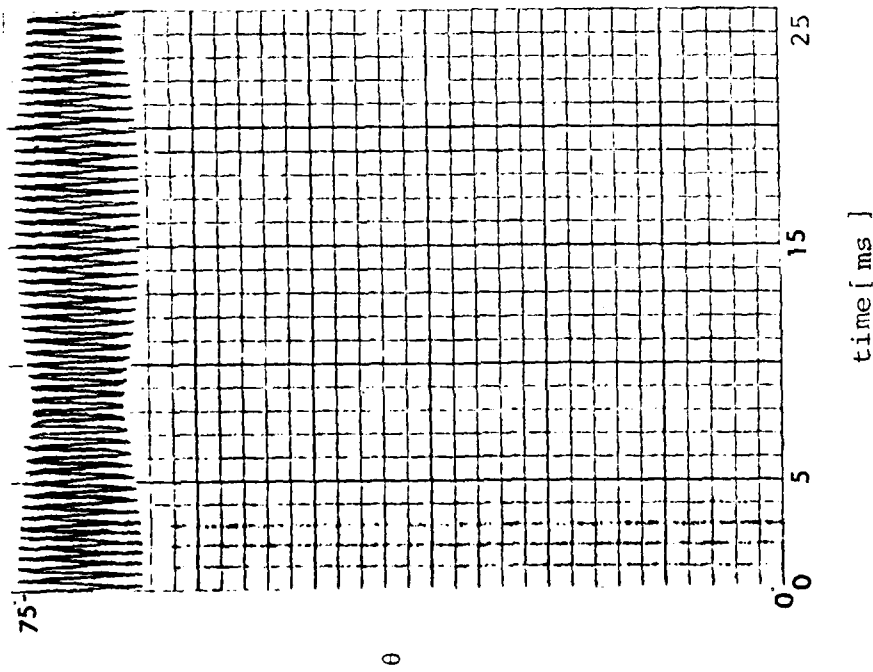


Figure 9.  $\theta$  vs. time for applied torques due to fluid friction of Couette model ( $S=1.2 \times 10^{-6}$ )

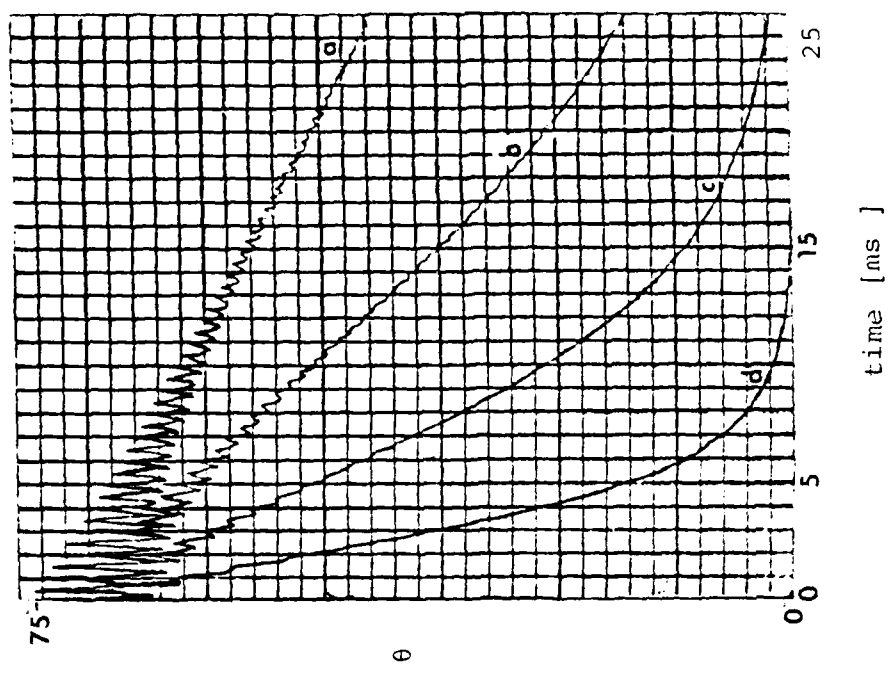


Figure 10.  $\theta$  vs. time for applied torques due to fluid friction of Couette model with increasing orders of magnitude  $S$ . (a)  $\sim 10^{-6}$ , (b)  $\sim 10^{-5}$ , (c)  $\sim 10^{-4}$  and (d)  $10^{-3}$

rapidly (see Fig. 10). From firings conducted at NWC, China Lake, on an indoor range, it is known that  $\theta$  reduces to a value which allows light from behind the projectile to be seen through the projectile by a camera aiming at the projectile image in a mirror down range. The length of the range is such that, for this to occur,  $\theta$  must reach the value  $\beta_s$  prior to impact on target, or in about 0.1 seconds. (see Fig. 11 for  $\beta_s$ ). The viscous model described above does not produce the moments required to cause sufficient reduction of  $\theta$  within this time of flight.

The viscous torques on the obturator were calculated above assuming a solid sphere. The actual obturator has an outside surface area less than that of a solid sphere of the same radius. The surface under the influence of viscous shearing stress is a very complicated function dependent upon the angle  $\theta$  as shown by the cross-hatched portion of Fig. 11. Calculations of the resulting moment are further complicated by the relative effect of the missing areas (due to the presence of holes) and their positions relative to the instantaneous axis of rotation. The time-dependent angles between the instantaneous axis of rotation and the  $x$  and  $z$ -axes must be known in order to determine the limits of integration for correct moment arm consideration.

Because the moment due to viscous effects is dependent upon the surface area involved and because the surface area in the first calculation (assuming a solid sphere) is larger,

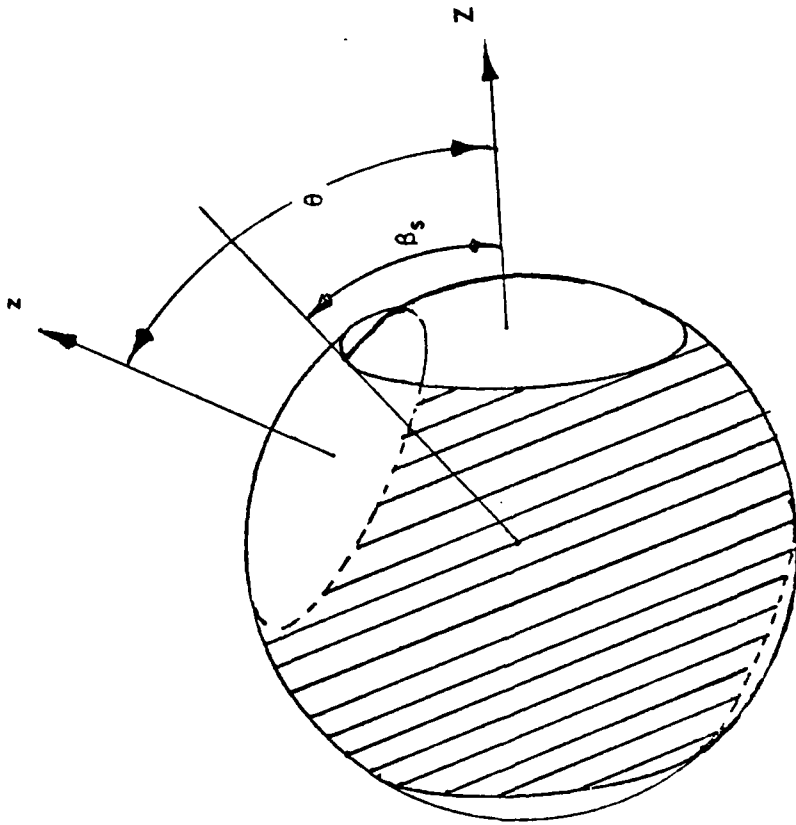


Figure 11. Surface area under the influence of viscous shearing stresses developed from Couette flow theory and physical relationships of the variable angle  $\theta$  and the geometrically determined constant  $\beta_s$ .

it is to be expected that by taking the holes into account the true moment due to viscous effects will be reduced. The effects of these area variations will be "blurred" by the high-speed relative motion and the additional complications necessary to account for them are not warranted in light of the goals of this analysis. Therefore for further development of viscous effects, the surface area of the obturator will be considered that of a solid sphere.

Nakabayashi [24] has conducted experiments to determine the viscous torque on rotating concentric spheres with various fluids and gap widths. He gives the general expression for the frictional moment on a sphere due to flow in the gap as

$$M_v = C_m \rho R_s^5 \omega_r^5 \quad (37)$$

where  $\rho$  is the density of the fluid in the gap. For laminar flow

$$C_m = \frac{8}{3\pi} \frac{(1+\epsilon)}{\epsilon} Re^{-1} \quad (38)$$

and for the turbulent flow

$$C_m = \frac{0.053}{\epsilon} \frac{1+(7/4)\epsilon}{1-(3/2)\epsilon} Re^{-0.25} \quad (39)$$

where  $\epsilon = h/R_s$ .

The Reynolds number is defined as

$$Re = \frac{R_s^2 \omega_r}{\nu} \quad (40)$$

in which  $\nu$  is the kinematic viscosity of the fluid in the gap. For the narrow gap width assumed for the BOT, the transition Reynolds number may be approximated by

$$Re_t = 70\epsilon^{-1.6} \quad (41)$$

(from Fig. 2a of Ref. 24.) In the case of the BOT, the relative angular velocities are insufficient to assume the existence of turbulent flow in the gap. Thus the frictional moment due to viscous flow in the gap is given by

$$\vec{M}_V = - \frac{8}{3}\pi \frac{(1+\epsilon)}{\epsilon} \mu_f R_s^3 \omega_r \frac{\epsilon_r}{\epsilon_r} \quad (42)$$

For small values of  $\epsilon$  (as is the case here), Eqs. (42) and (33) are identical.

## 2. Moments Due To Sliding Friction

It has been noted that the extreme propellant gas pressures inside the barrel are assumed sufficient to hold the obturator fixed to the projectile during launch. However upon exiting the barrel, the pressure distribution on the projectile is due to the aerodynamic characteristics of the projectile. Assuming the obturator is still blocking the projectile duct, a detached bow shock is set up (see Fig. 2b). The pressure,  $P_2$ , downstream of this shock is given by one-dimensional shock theory from Eq. (1). It is assumed that  $P_2$  is sufficiently large to cause the obturator to contact the rear of the projectile socket housing the obturator.

The forces involved depend upon the projected area of the hole through the projectile and the contact point(s) of the obturator and projectile. The force acting on the obturator is assumed to be given by

$$F_p = \pi r_p^2 \Delta P \quad [\text{see Eqs. (1) and (3)}] \quad (43)$$

where  $r_p$  is the radius of the hole through the projectile and

$$\Delta P = P_1 - P_2 \quad (44)$$

From sliding friction theory, the contact area is not a consideration; only the magnitude of the force normal to the contact surface and the coefficient of friction of the materials in contact are important. In the case of the obturator, the pressure force,  $F_p$  acts along the z-axis. The reaction force may be broken into a component tangent to the obturator and a normal component acting through the center of the obturator. The normal component,  $F_n$ , multiplied by the coefficient of friction  $\mu_s$ , gives the sliding friction force acting to oppose the motion of the obturator:

$$F_s = F_n \mu_s \quad (45a)$$

where

$$F_n = F_p \cos \beta_s \quad (45b)$$

so that

$$F_s = F_p \cos \beta_s \mu_s \quad (46)$$

This assumes the holes through the obturator and projectile have the same diameter and that the point or points of contact are on the locus of points described by the intersection of the hole through the projectile and the spherical socket housing the obturator in the projectile. This locus of points is a circle of radius  $r_p$  and each point is a distance  $R_s$  from the center of the obturator. Gravity forces are neglected since they are relatively small and act both on the obturator and the projectile.

For a "perfect" fit between ball and projectile, the sliding friction force is distributed over an infinite number of points and, in the limit, the force at each point vanishes. This situation has no significance in reality and, therefore, engineering judgement dictates making some assumptions with regard to the point(s) of application of the friction force  $F_s$ .

For the general case, a point of contact  $P$  may be described relative to the inertial reference frame as being at an angle  $\beta_s$  from the inertial  $Z$ -axis, a distance  $R_s$  from the center of the obturator and at an angle  $\gamma$  from the  $X$ - $Z$  plane measured toward the positive  $Y$ -axis as shown in Fig. 12. For this approximation, assume two contact points in the  $X$ - $Z$  plane,  $P_1$  and  $P_2$ .  $P_1$  and  $P_2$  are  $180^\circ$  apart on the circle of points so that  $\gamma=0$  and  $\beta=\beta_s$ .

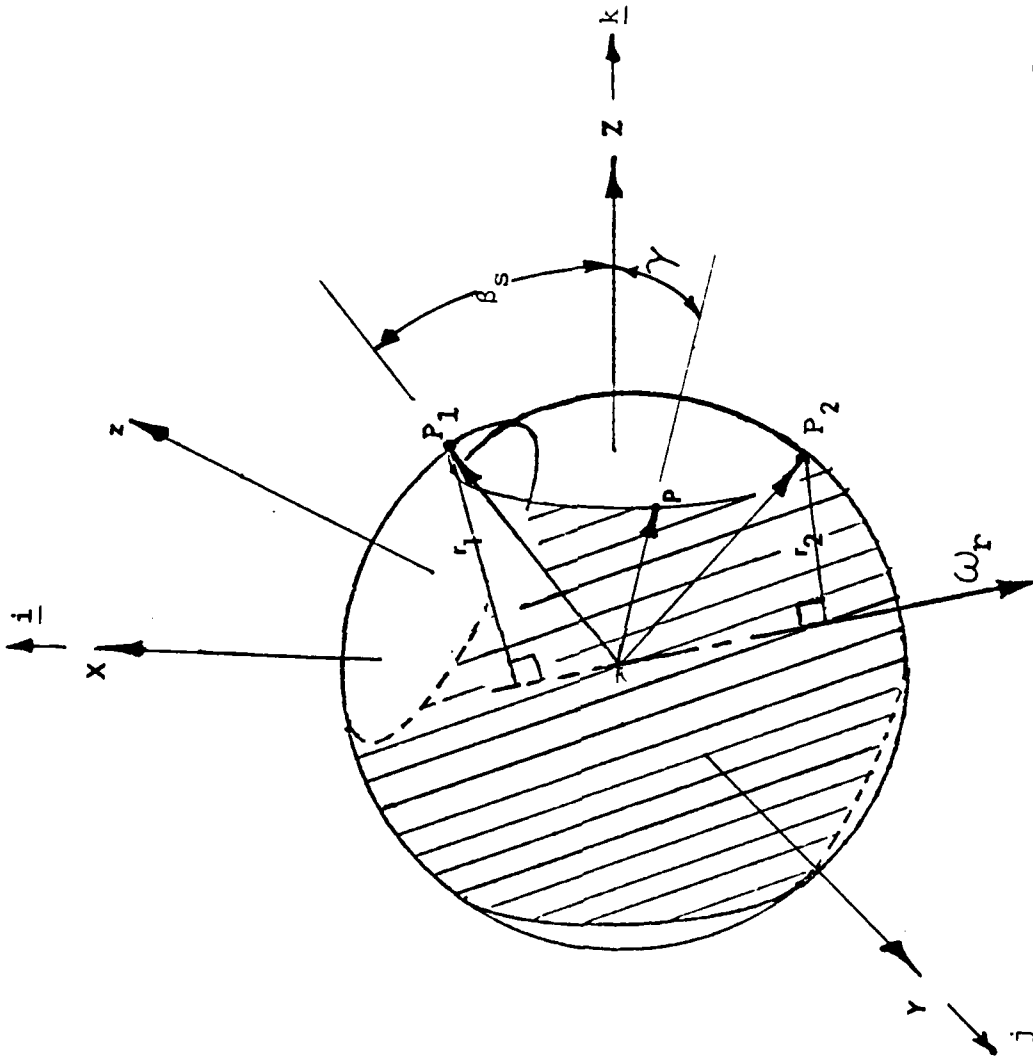


Figure 12. Geometric relationships for determining moment arm  $r_1$  and  $r_2$  for calculating sliding friction torques due to aerodynamic forces.

From the vector analysis, the projection of one vector onto another is given by the scalar or dot product. The vectors  $\vec{P}_1$  and  $\vec{P}_2$  are given by:

$$\begin{aligned}\vec{P}_1 &= R_S (\sin\beta\vec{i} + \cos\beta\vec{k}) \\ \vec{P}_2 &= R_S (-\sin\beta\vec{i} + \cos\beta\vec{k})\end{aligned}\tag{47}$$

Their projections onto the relative angular velocity vector  $\vec{\omega}_R$ , with components  $\omega_x$ ,  $\omega_y$  and  $\omega_z$ , are

$$\begin{aligned}\vec{P}_1 \cdot \vec{\omega}_R &= R_S (\omega_x \sin\beta + \omega_z \cos\beta) \\ \vec{P}_2 \cdot \vec{\omega}_R &= R_S (-\omega_x \sin\beta + \omega_z \cos\beta)\end{aligned}\tag{48}$$

The scalar dot product is also defined as

$$\vec{P}_1 \cdot \vec{\omega}_R = P_1 \omega_R \cos\eta\tag{49}$$

where  $\eta$  is the angle between the vectors  $\vec{P}_1$  and  $\vec{\omega}_R$ . Therefore from Eqs. (48) and (49)

$$\begin{aligned}R_S (\omega_x \sin\beta + \omega_z \cos\beta) &= P_1 \omega_R \cos\eta \\ R_S (-\omega_x \sin\beta + \omega_z \cos\beta) &= P_2 \omega_R \cos\Omega\end{aligned}\tag{50}$$

The magnitude of the vectors  $\vec{P}_1$  and  $\vec{P}_2$  is  $R_S$ , so solving for  $\eta$  and  $\Omega$  gives

$$\eta = \cos^{-1} \left[ \frac{\omega_x}{\omega_r} \sin\beta + \frac{\omega_z}{\omega_r} \cos\beta \right] \quad (51)$$

$$\Omega = \cos^{-1} \left[ -\frac{\omega_x}{\omega_r} \sin\beta + \frac{\omega_z}{\omega_r} \cos\beta \right]$$

The moment arms  $r_1$  and  $r_2$  from Fig. 12 are therefore given by

$$r_1 = R_s \sin \left[ \cos^{-1} \left( \frac{\omega_x}{\omega_r} \sin\beta + \frac{\omega_z}{\omega_r} \cos\beta \right) \right] \quad (52)$$

$$r_1 = R_s \left[ 1 - \left( \frac{\omega_x}{\omega_r} \sin\beta + \frac{\omega_z}{\omega_r} \cos\beta \right)^2 \right]^{\frac{1}{2}}$$

$$r_2 = R_s \sin \left[ \cos^{-1} \left( -\frac{\omega_x}{\omega_r} \sin\beta + \frac{\omega_z}{\omega_r} \cos\beta \right) \right] \quad (53)$$

$$r_2 = R_s \left[ 1 - \left( \frac{\omega_z}{\omega_r} \cos\beta - \frac{\omega_x}{\omega_r} \sin\beta \right)^2 \right]^{\frac{1}{2}}$$

The moment acting on the obturator due to the sliding friction due to aerodynamic forces are given by

$$\vec{M}_{sa} = (r_1 + r_2) \frac{F_p}{2} \cos\beta \mu_s \frac{\vec{\omega}_r}{\omega_r} \quad (54)$$

Substituting from Eqs. (52) and (53) into Eq. (54) leaves

$$\vec{M}_{sa} = \frac{\sqrt{2}}{2} R_s F_p \cos\beta \mu_s \left[ 1 - \left( \frac{\omega_x}{\omega_r} \right)^2 \sin^2\beta - \left( \frac{\omega_z}{\omega_r} \right)^2 \cos^2\beta \right]^{\frac{1}{2}} \frac{\vec{\omega}_r}{\omega_r} \quad (55)$$

It should be noted that if there were  $n$  contact points that the normal force at each point would be given by  $F_n/n$ . Equation (54) indicates the case of two points of contact discussed here.

As yet, there has been no attempt in the laboratory to produce the aerodynamic forces present on the obturator for an actual projectile in flight. The sliding friction forces present on the obturator in the experiments (described in section III) are due to gravity alone. The obturator is supported by the projectile simulator (see Fig. 24). Because the obturator is smaller than the housing in the projectile, a point contact at the bottom of the housing is assumed. This point has inertial coordinates of  $(-R_s, 0, 0)$ . The vector from the origin to the point is given by

$$\vec{P}_G = -R_s \underline{i} \quad (56)$$

Using a development similar to that for obtaining the moment arm for the friction forces due to aerodynamic considerations, the forces on the model due to gravity may be determined. Again, the dot product is given by

$$\vec{P}_G \cdot \vec{\omega}_r = -R_s \omega_x \quad (57)$$

which is the same as  $P_G \omega_r \cos \xi$ .

Therefore the angle ( $\xi$ ) between the angular velocity vector  $\vec{\omega}_r$  and  $\vec{P}_G$  is obtained from

$$\xi = \cos^{-1} \left( - \frac{\omega_X}{\omega_r} \right) \quad (58)$$

The moment arm  $r_g$  is found as in Eq. (55) from

$$r_g = R_s \sin \left[ \cos^{-1} \left( - \frac{\omega_X}{\omega_r} \right) \right] \quad (59)$$

or

$$r_g = R_s \left[ 1 - \left( \frac{\omega_X}{\omega_r} \right)^2 \right]^{\frac{1}{2}} \quad (60)$$

which means the sliding friction moment due to the weight  $W$  is

$$\vec{M}_{sg} = \mu_s W R_s \left[ 1 - \left( \frac{\omega_X}{\omega_r} \right)^2 \right]^{\frac{1}{2}} \frac{\vec{\omega}_r}{\omega_r} \quad (61)$$

The torques acting on the obturator are the summation of the torques due to friction, both viscous and sliding (aerodynamic or gravitational). The general form of the torques acting to oppose the motion of the obturator in terms of total moment  $M_t$  and the unit vector  $\vec{l}_r$  along  $\vec{\omega}_r$  is

$$\vec{G} = -M_t \vec{l}_r \quad (62)$$

which, when broken into the various contributors becomes, for the projectile in flight,

$$\vec{G}_p = -(M_v + M_{sa}) \vec{l}_r \quad (63)$$

TABLE I

COMMON VALUES

$\theta_0 = 87.25^\circ$   
 $\dot{\phi}_0 = 0$   
 $\dot{\theta}_0 = 0$   
 $\phi_0 = 0$   
 $\psi_0 = 0$   
 $\rho = 7669.6 \text{ Kg/m}^3$   
 $R_s = 7.899 \text{ mm}$   
 $r_p = 4.72 \text{ mm}$   
 $C = 3.125 \times 10^{-7} \text{ N-m-s}^2$   
 $A = 2.216 \times 10^{-7} \text{ N-m-s}^2$   
 $\lambda = 0.41$   
 $\mu_f = 1.917 \times 10^{-5} \text{ Pa-s}$   
 $\mu_s = 0.35$   
 $h = 5.08 \times 10^{-5} \text{ m}$   
 $S = 12.38 \times 10^{-9} \text{ N-m-s}$

AERODYNAMIC MODEL

$R_p = 9.96 \text{ mm}$   
 $L_p = 76.2 \text{ mm}$   
 $m_p = 0.141 \text{ Kg}$   
 $I_p = 8.58 \times 10^{-6} \text{ N-m-s}^2$   
 $M_1 = 3.0$   
 $\gamma = 1.4$   
 $P_1 = 0.099 \text{ MPa}$   
 $\omega_p = 12042 \text{ sec}^{-1}$

GRAVITATIONAL MODEL

$W = 0.07987 \text{ N}$   
 $E(\theta_0, \pi/2) = 1.0063$   
 $\omega_p = 200 \text{ sec}^{-1}$

and for the experimental model,

$$\vec{G}_m = -(M_v + M_{sg}) \vec{I}_r \quad (64)$$

These may easily be transformed into the body-fixed coordinate system for solution of the equations of motion.

For solving Eq. (17), a numerical integration subroutine [25] was used and computer plots of  $\theta$  vs. time were obtained. A copy of the calling program is included in Appendix A. Figures 13 and 14 show plotted output for the input parameters shown in Table 1.

### C. DEVELOPMENT OF AN APPROXIMATE SOLUTION

Observations of the nature of the exact solution (Figs. 13 and 14) indicate that the response of the obturator orientation ( $\theta$ ) to the applied torques (determined from Table 1 parameters) is similar to that of a linear damped second-order system with a combined step and ramp input. That is, the relationship closely follows a relationship of the form

$$\theta = \theta_0 + D + \frac{R}{\omega_n} (\omega_n t - 2\zeta) + \frac{\exp(-\zeta\omega_n t)}{(1-\zeta^2)^{\frac{1}{2}}} \left\{ \frac{R}{\omega_n} \sin[\omega_n (1-\zeta^2)^{\frac{1}{2}} t + \phi_R] - D \sin[\omega_n (1-\zeta^2)^{\frac{1}{2}} t + \phi_D] \right\} \quad (65)$$

in which the parameters are:

- D = step height (negative)
- R = ramp slope (negative)
- $\omega_n$  = natural frequency
- $\zeta$  = damping ratio
- $\phi_D, \phi_R$  = phase angles

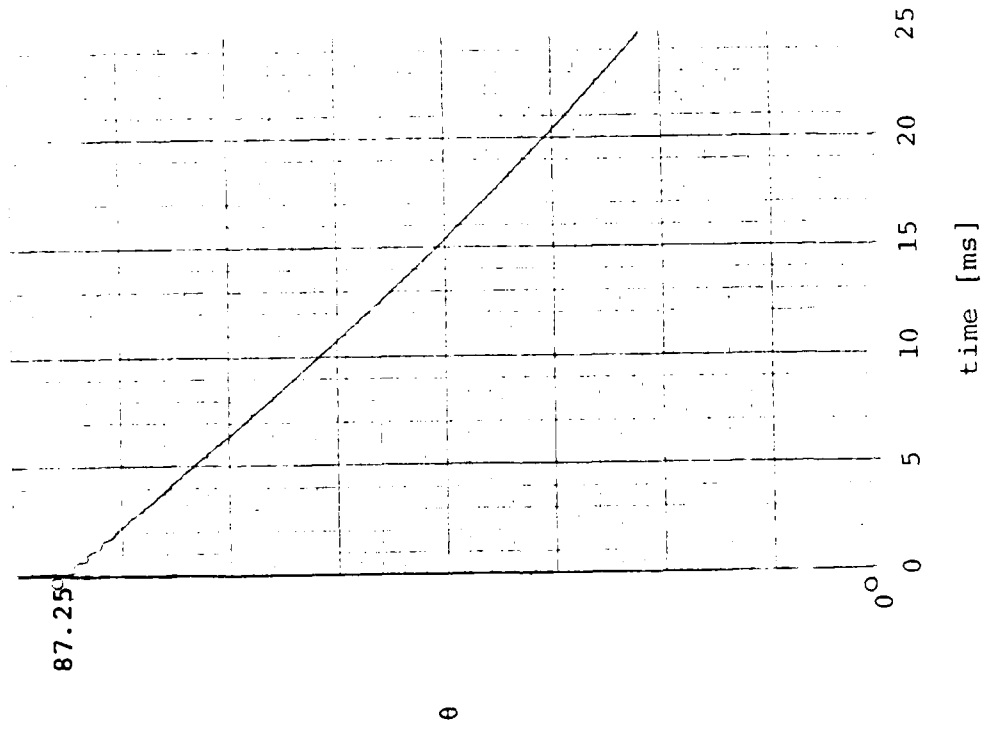


Figure 13. Plot of  $\theta$  vs. time for BOT utilizing aerodynamic force development.

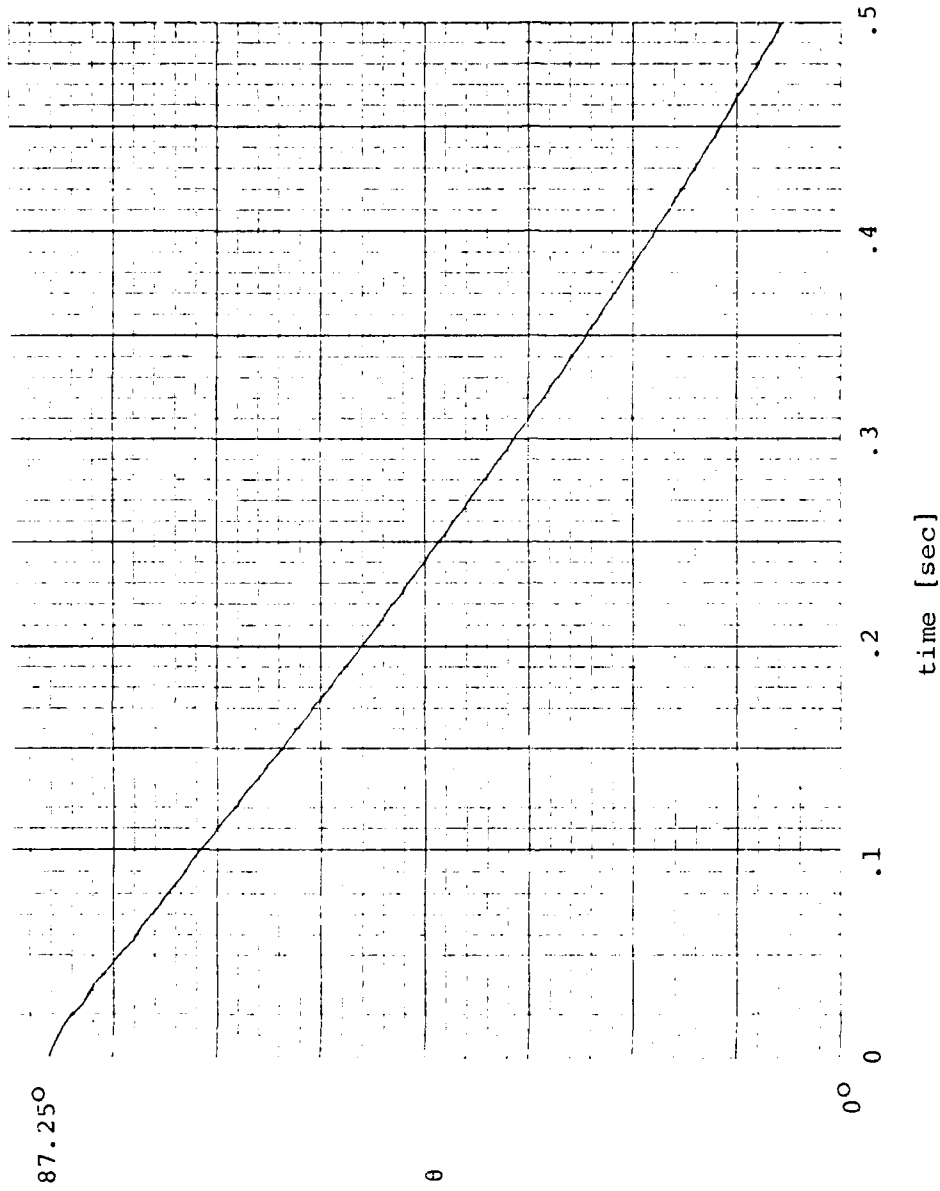


Figure 14. Plot of  $\theta$  vs. time for BOT utilizing gravitational force development.

These may be determined by means of a solution to the linearized equations of motion under the assumption of small applied torques  $[(M/C\omega_p^2) \ll 1]$ . This has been accomplished<sup>2</sup> by a perturbation of the steady state solution given by Eq. (18) for the case of no applied torques.

The first step in the approximation is to rewrite Eq. (18) to read

$$\lambda \dot{\psi}_0 \cos \theta_0 + (\lambda+1) \dot{\phi}_0 = 0 \quad (66)$$

where  $\dot{\psi}_0$ ,  $\dot{\phi}_0$  and  $\theta_0$  are constants. The dependent variables of the general form of the governing equations (Eq. 17) are written as sums of the unforced values and the perturbation values. Thus

$$\begin{aligned} \dot{\phi} &= \dot{\phi}_0 + \dot{\phi}, \quad \dot{\psi} = \dot{\psi}_0 + \dot{\psi}, \quad \theta = \theta_0 + \theta \\ \ddot{\phi} &= \ddot{\phi}, \quad \ddot{\psi} = \ddot{\psi}, \quad \dot{\theta} = \dot{\theta}, \quad \ddot{\theta} = \ddot{\theta} \end{aligned} \quad (67)$$

The general form for the applied torques on the obturator in the experimental model (gravity-driven sliding friction) is given by Eq. (64) in which the moment term is composed of a fluid ( $M_V$ ) and a sliding friction ( $M_{SG}$ ) term. When both are expanded from Eqs. (42) and (61), Eq. (62) becomes

$$\vec{G} = - \left\{ S\omega_r + \mu_S W R_S \left[ 1 - \left( \frac{\omega_x}{\omega_r} \right)^2 \right]^{\frac{1}{2}} \right\} \frac{\vec{\omega}_r}{\omega_r} \quad (68)$$

---

<sup>2</sup>The theoretical development of the linear approximation is not complete. The analysis presented here therefore represents a preliminary report.

The relative velocity  $\omega_r$  from Eqs. (13, 35 and 36) has components

$$\begin{aligned}\omega_{1r} &= (\dot{\psi} - \omega_p) \sin\theta \sin\phi + \dot{\theta} \cos\phi \\ \omega_{2r} &= (\dot{\psi} - \omega_p) \sin\theta \cos\phi - \dot{\theta} \sin\phi \\ \omega_{3r} &= (\dot{\psi} - \omega_p) \cos\theta + \dot{\phi}\end{aligned}\tag{69}$$

To the first approximation,  $\dot{\psi}_0 = \omega_p$  ( $\dot{\psi}_0 = \omega_p$  for the case of no applied torques). With this approximation, and the application of the perturbed variables, Eq. (67),

$$\begin{aligned}\omega_{1r} &= \dot{\theta} \cos\phi_0 \\ \omega_{2r} &= -\dot{\theta} \sin\phi_0 \\ \omega_{3r} &= \dot{\psi} \cos\theta_0 + \dot{\phi}_0 + \dot{\phi}\end{aligned}\tag{70}$$

The only term of zeroth order in Eqs. (70) is  $\dot{\phi}_0$  so that, to the first approximation,

$$\omega_r = \omega_{3r} \approx |\dot{\phi}_0|\tag{71}$$

The modulus is taken in order to preserve the positive sense of  $\omega_r$ . Under the same approximations as above,

$$\omega_x = \dot{\phi}_0 \sin\phi_0 \sin\psi_0\tag{72}$$

Substituting Eqs. (71 and 72) into Eq. (60) for the sliding friction moment arm,  $r_g/R_s$  becomes

$$\frac{r_g}{R_s} = [1 - (\sin\theta_0 \sin\psi_0)^2]^{\frac{1}{2}} \quad (73)$$

For the purpose of the linear approximation, the mean value of this moment arm is required. Integrating to find the average moment arm gives

$$\bar{\frac{r_g}{R_s}} = \frac{1}{T} \int_0^T (r_g/R_s) dt \quad (74)$$

where T is the period for one revolution. From the approximation, however,

$$T = \frac{2\pi}{\psi_0} = \frac{2\pi t}{\psi_0} \quad (75)$$

and because of symmetry, the average is valid over one-quarter period, therefore

$$\bar{\frac{r_g}{R_s}} = \frac{4}{T} \int_0^{\pi/4} (1 - \sin^2\theta_0 \sin^2 \frac{2\pi t}{T})^{\frac{1}{2}} dt \quad (76)$$

By letting  $u = 2\pi t/T$  and  $du = (2\pi/T)dt$ , Eq. (76) becomes

$$\bar{\frac{r_g}{R_s}} = \frac{2}{\pi} \int_0^{\pi/2} (1 - \sin^2\theta_0 \sin^2 u)^{\frac{1}{2}} du \quad (77)$$

Letting  $E(\theta_0)$  denote a Complete Elliptic Integral of the Second Kind with modular angle  $\theta_0$ , Eq. (77) may now be written as

$$\frac{\bar{r}}{R_s} = \frac{2}{\pi} E(\theta_0) \quad (78)$$

Solutions to Eq. (78) are tabulated for various values of  $\theta_0$ .

The expression for the applied torque vector (Eq. 68) may now be written as

$$\vec{G} = -[S|\dot{\phi}| + \mu_s WR_s \frac{2}{\pi} E(\theta_0)] \frac{\vec{\omega}_r}{|\dot{\phi}|} \quad (79)$$

With these approximations, the applied torque terms appearing in Eq. (17) are given by

$$\frac{G_1}{A} \sin \phi + \frac{G_2}{A} \cos \phi = \frac{-M}{A\omega_r} (\psi - \omega_p) \sin \theta \approx 0$$

$$\frac{G_2}{A} \cos \phi - \frac{G_1}{A} \sin \phi = \frac{-M}{A\omega_r} \dot{\theta} \approx \frac{-M\dot{\theta}}{A|\dot{\phi}_0|}$$

$$\frac{G_3}{C} = \frac{-M}{C\omega_r} [(\psi - \omega_p) \cos \theta + \dot{\phi}] \approx \frac{-M}{C|\dot{\phi}_0|} \dot{\phi}_0 \approx \frac{-M}{C} \frac{\dot{\phi}_0}{|\dot{\phi}_0|} \quad (80)$$

where  $M$  is given by

$$M = S|\dot{\phi}_0| + \mu_s WR_s \frac{2}{\pi} E(\theta_0) \quad (81)$$

and  $\omega_p$  is the projectile angular velocity.

Equations (66), (67) and (80) are combined with Eq. (17). After simplification, and retaining only the first order (linear) terms, the results are:

$$\ddot{\psi} = -(\dot{\psi}_0 \cot \theta_0) \dot{\theta} \quad (82)$$

$$\ddot{\phi} = (\dot{\psi}_0 \csc \theta_0) \dot{\theta} - \frac{M}{C} \frac{\dot{\phi}_0}{|\dot{\phi}_0|} \quad (83)$$

$$\ddot{\theta} = \frac{-M}{A|\dot{\phi}_0|} \dot{\theta} - \dot{\psi}_0 \sin \theta_0 [\dot{\phi}(1+\lambda) - \theta \lambda \dot{\psi}_0 \sin \theta_0 + \dot{\psi} \lambda \cos \theta_0] \quad (84)$$

These equations are then integrated under the following initial conditions

$$\left. \begin{aligned} \dot{\psi}(0) &= \dot{\psi}_0 = \omega_p \\ \dot{\phi}(0) &= 0 \\ \theta(0) &= \theta_0 \\ \dot{\theta}(0) &= 0 \end{aligned} \right\} \begin{aligned} \dot{\psi} &= 0 \\ \dot{\phi}(0) &= -\dot{\phi}_0 = \frac{\lambda}{\lambda+1} \dot{\psi}_0 \cos \theta_0 \\ \dot{\theta}(0) &= 0 \\ \dot{\theta}(0) &= 0 \end{aligned}$$

Eq. (82) yields

$$\dot{\psi} = -(\dot{\psi}_0 \cot \theta_0) \theta \quad (85)$$

From Eq. (83)

$$\dot{\phi} = -\dot{\phi}_0 + (\dot{\psi}_0 \cos \theta_0) \theta - \frac{M}{C} \frac{\dot{\phi}_0}{|\dot{\phi}_0|} \quad (86)$$

By substituting the expressions obtained in Eqs. (85) and (86) into Eq. (84), the differential equation for  $\theta$  becomes

$$\ddot{\theta} = \frac{-M\dot{\theta}}{A|\dot{\phi}_0|} - \dot{\psi}_0 \sin\theta_0 [\dot{\psi}_0 \dot{\theta} - (1+\lambda)(\dot{\phi}_0 + \frac{M}{C} t)] \quad (87)$$

or, in a more familiar form,

$$\frac{\ddot{\theta}}{\omega_n^2} + \frac{2\zeta}{\omega_n} \dot{\theta} + \theta = D + Rt \quad (88)$$

where  $\omega_n = \dot{\psi}_0 = \omega_p$ ,  $\dot{\phi}_0/|\dot{\phi}_0| = -1$  and

$$\zeta = \frac{M}{2A|\dot{\phi}_0|\dot{\psi}_0}$$

$$D = \frac{(1+\lambda)\dot{\phi}_0 \sin\theta_0}{\dot{\psi}_0} = -\frac{\lambda}{2} \sin 2\theta_0$$

$$R = -\frac{(1+\lambda)}{\dot{\psi}_0} \frac{M}{C} \sin\theta_0 = -\frac{MD}{\dot{\phi}_0 C}$$

Expansion of the expressions above, using Eq. (81) shows that the damping coefficient is given by:

$$\zeta = \frac{1}{2A|\dot{\phi}_0|\dot{\psi}_0} [S|\dot{\phi}_0| + \mu_s W R_s \frac{2}{\pi} E(\theta_0)]$$

or

$$\zeta = \frac{1}{2A\dot{\psi}_0} [S + \mu_s R_s W \frac{2}{\pi} \frac{(\lambda+1)}{\lambda\dot{\psi}_0 \cos\theta_0} E(\theta_0)]$$

and the ramp slope (rate of decay) becomes

$$R = \left( - \frac{\lambda}{(\lambda+1)} \dot{\psi}_0 \sin 2\theta_0 \right) \zeta \quad (90)$$

The integral of Eq. (87) with the initial conditions specified [ $\theta(0) = \dot{\theta}(0) = 0$ ] is Eq. (65) where

$$\phi_R = 2\phi_D = 2 \tan^{-1} \frac{(1-\zeta^2)^{\frac{1}{2}}}{\zeta} \quad (91)$$

For large values of  $\zeta\omega_n t$ , the ramp decay dominates the response and the solution may be further approximated by

$$\theta = \theta_0 + \tilde{\theta} = \theta_0 + D + \frac{R}{\omega_n} (\omega_n t - 2\zeta)$$

The time to nutate through a known angle  $\theta$  may be found from

$$t = \frac{\theta - \theta_0 - D}{R} + \frac{2\zeta}{\omega_n} = \frac{2\zeta}{\omega_n} - \frac{(\theta_0 - \theta)}{R} - \frac{D}{R} \quad (92)$$

where  $\zeta$ ,  $R$ ,  $D$  and  $\omega_n$  are prescribed in Eqs. (88)-(90).

Figure 15 is a plot of  $\theta$  vs. time comparing the results of the exact solution from Fig. 14 with those of the approximation developed here. The physical constants and initial conditions are identical for the two cases.

#### D. THE EFFECT OF GEOMETRY ON OBTURATOR RESPONSE

In the discussion to this point a primary consideration has been to model the external forces acting on the obturator.

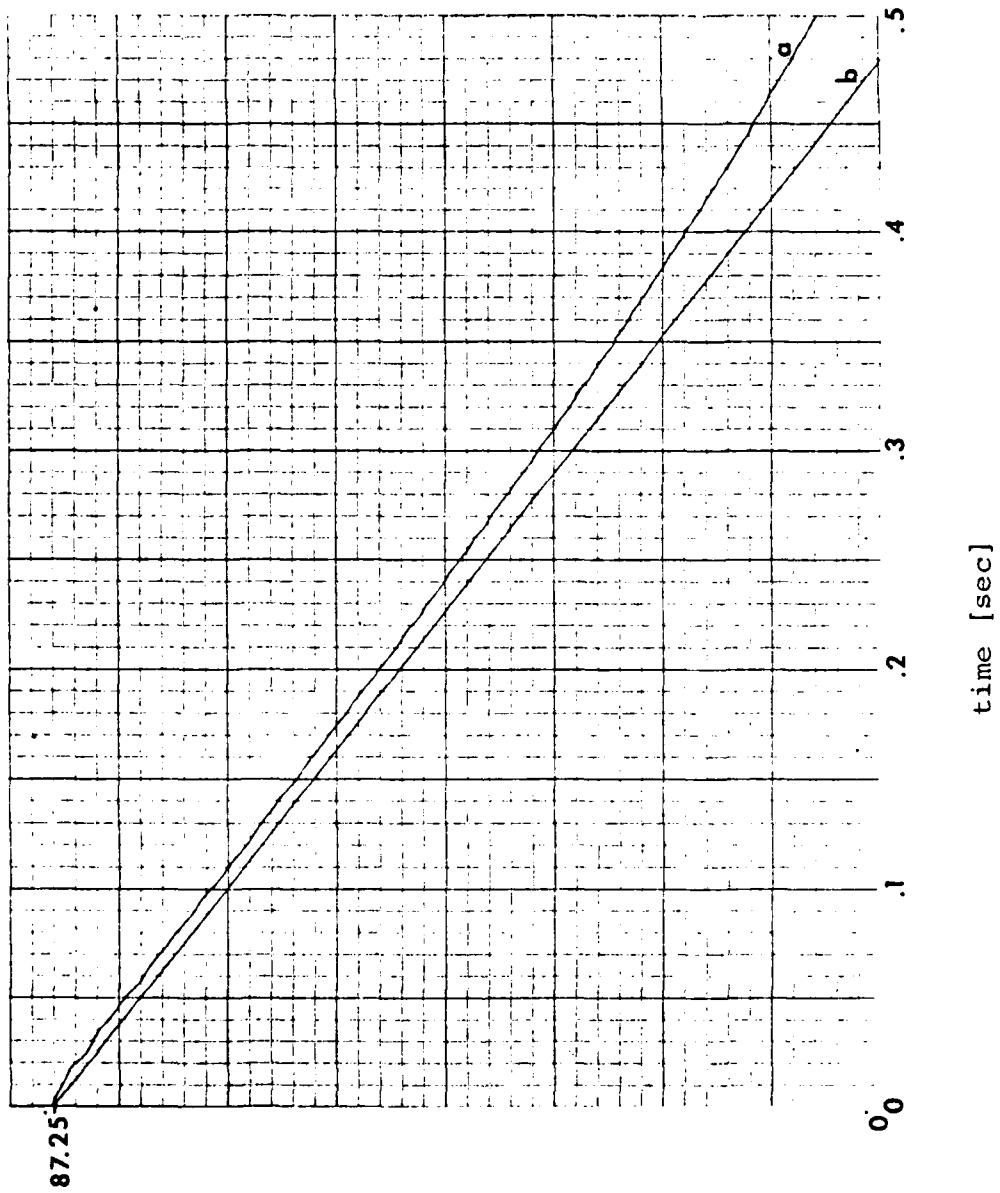


Figure 15. Comparison plot of  $\theta$  vs. time for the (a) exact and (b) approximate solutions.

The effect of geometry has not been discussed, but is a most significant contributor to the response of the obturator.

C and A are functions of mass density and physical dimensions. By varying the material composition (density) the response will vary. Utilizing the physical dimensions of the obturator in Table 1, the obturator volume may be calculated by subtracting the volumes of a right circular cylinder of radius  $r_p$ , length  $2R_s \cos \beta$ , and the two spherical caps at the ends of the hole from the volume of a sphere [26]. Thus the volume of the obturator is given by

$$V = \frac{4}{3}\pi R_s^3 - \frac{2}{3}\pi (R_s - R_s \cos \beta)^2 (2R_s + R_s \cos \beta) - 2\pi r_p^2 R_s \cos \beta$$

Collecting terms gives

$$V = 2\pi R_s \cos \beta \left[ R_s^2 \left( 1 - \frac{\cos^2 \beta}{3} \right) - r_p^2 \right]$$

By knowing the mass density, the weight of the obturator [for use in the torque expression, Eq. (61)] may be obtained. Therefore as the density varies, the values of C, A and W vary. Fig. 16 is a family of curves of  $\theta$  vs.  $t$  for varying density with all other physical properties being those of Table 1.

There is however a limiting case for the size of the hole. If the hole becomes too large (assuming same size

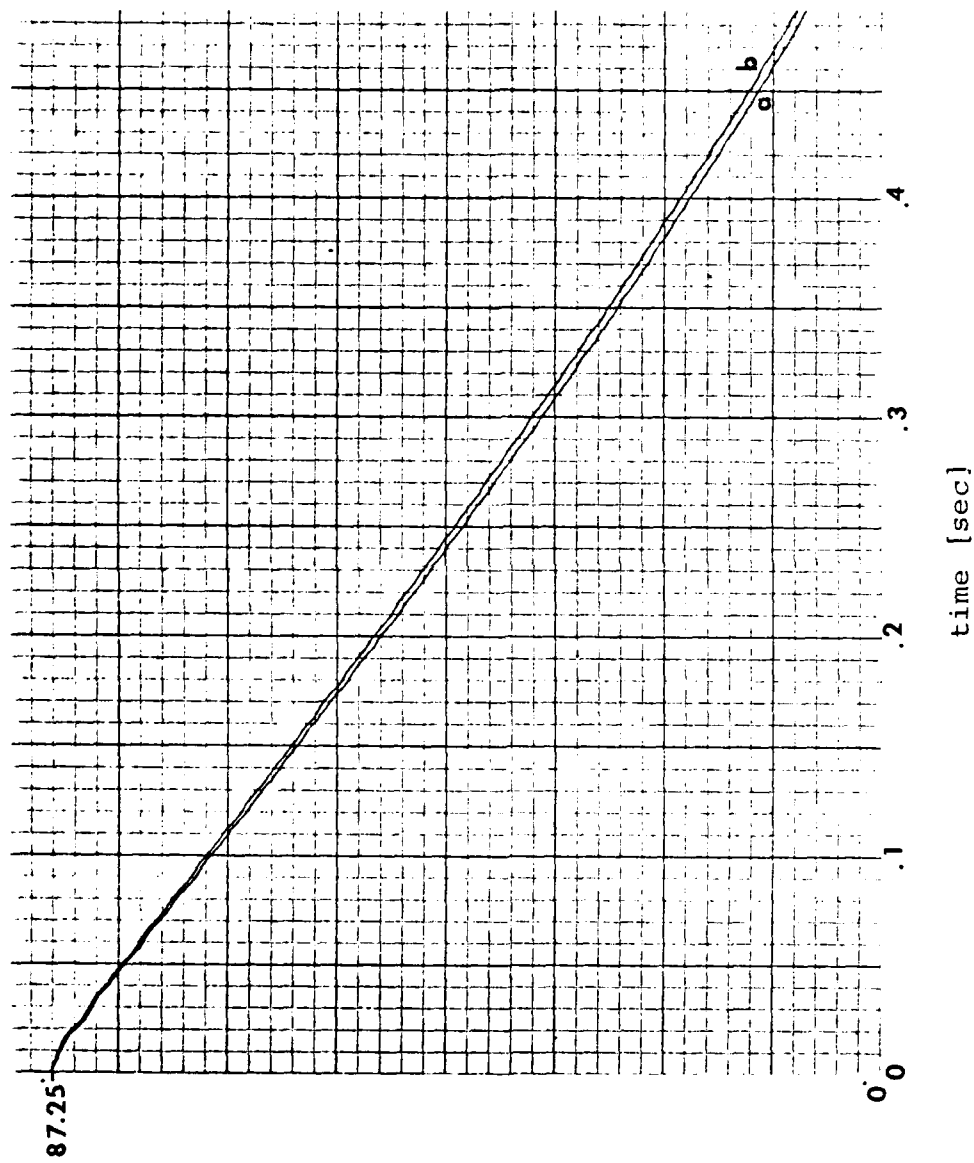


Figure 16. Comparison plot of  $\theta$  vs. time for obturator material densities of (a) 6000 Kg/m<sup>3</sup> and (b) 10000 Kg/m<sup>3</sup>

projectile hole), there may not be sufficient obturator surface area to block the passage. The limiting relationship is

$$r_s \leq \frac{R_s}{\sqrt{2}}$$

This limit is purely theoretical and is not a feasible design parameter. Engineering judgement in the selection of realistic values is required so that the projectile will meet the ballistics criteria and retain its integrity while undergoing the forces associated with the entire firing evolution from chambering to target impact.

The effect on the obturator response due to increasing the hole diameter is shown in Fig. 17. The inertial contribution to the response (coupled term) is increased by increasing C/A and therefore  $\lambda$ ; however the friction torque ( $M_{sg}$ ) contribution is lessened by the reduction in the mass of the ball.

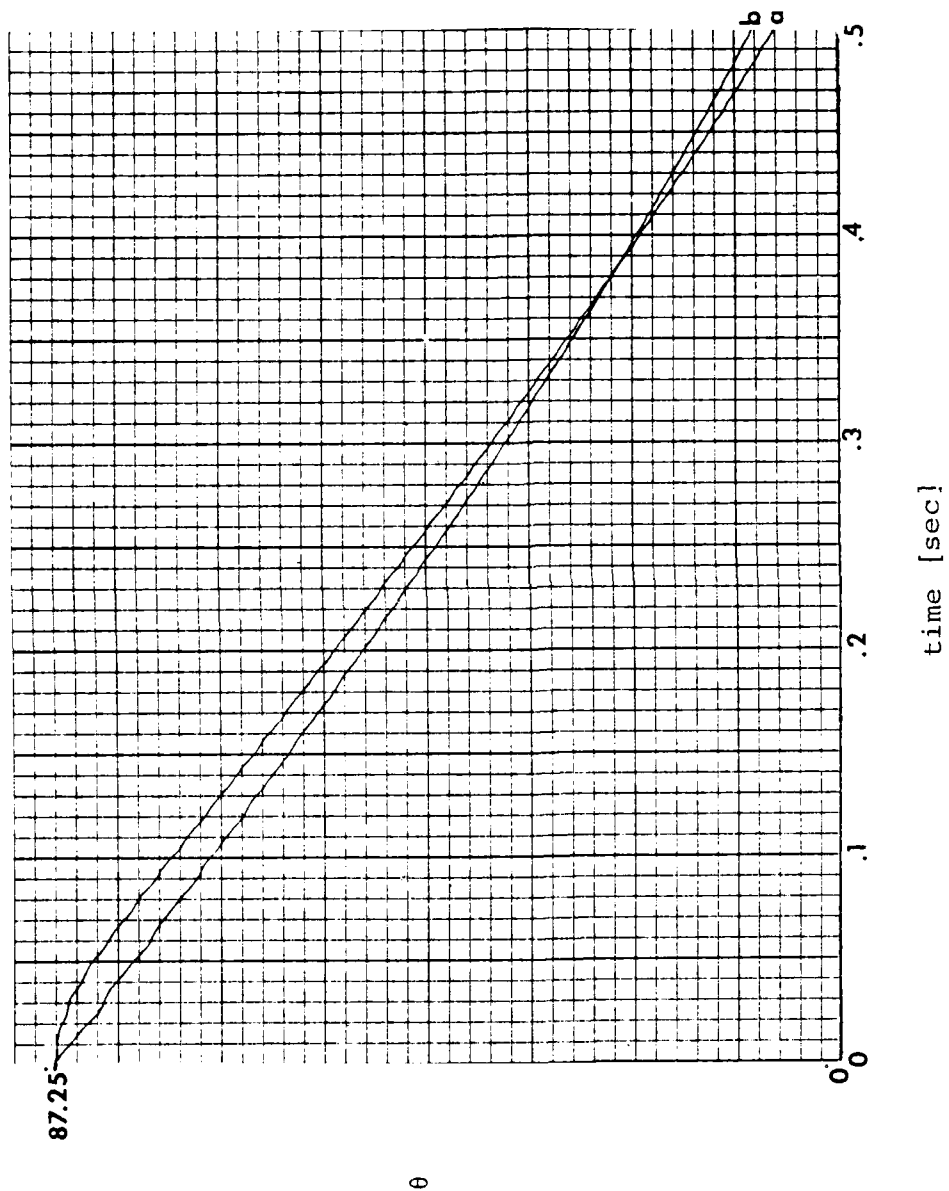


Figure 17. Comparison plot of  $\theta$  vs. time for obturator hole radii of (a) 3.75 mm and (b) 5.58 mm.

### III. EXPERIMENTATION

#### A. EXPERIMENTAL APPARATUS

An experimental system was designed to simulate the spinning BOT. The apparatus consisted of a compressed-air-driven spin-up rig, optical timing mechanism, air manifold and associated piping, tubing and electronics.

The obturator was fabricated from a standard 5/8-in. diameter chrome-steel (52100) bearing ball. The ball was annealed to allow machining and then bored along a diametrical axis (Fig. 18). The bored ball was then mounted in a bakelite metallographic specimen mount. The mounted ball was placed in a milling machine and a flat was machined in the bakelite at a specified angle relative to the axis through the hole in the ball (Figs. 19 and 20). This flat was then used as the polishing plane for metallographic specimen preparation. A small flat spot was polished on the obturator to provide a highly reflective surface at a known orientation relative to the z-axis of the obturator (Fig. 21).

After removal from the bakelite mount, the obturator was placed in a three-piece, lucite housing (Fig. 22). The mating ends of the two hollow inner cylinders were each machined with a 5/8-inch end mill to a depth of approximately 5/16-inch. When mated, a spherical cavity was formed to accommodate the obturator. The third cylinder was press fit

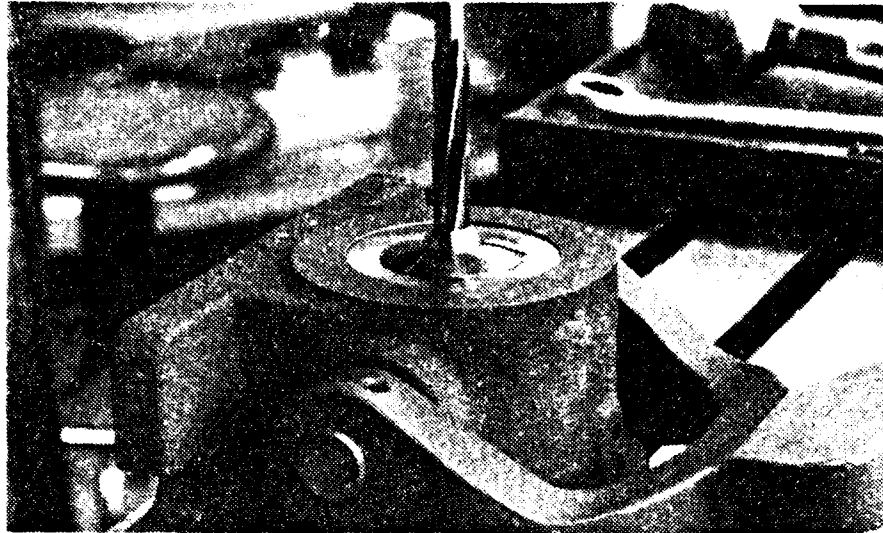


Figure 18. Boring of hole along a diametrical axis of the annealed bearing ball.

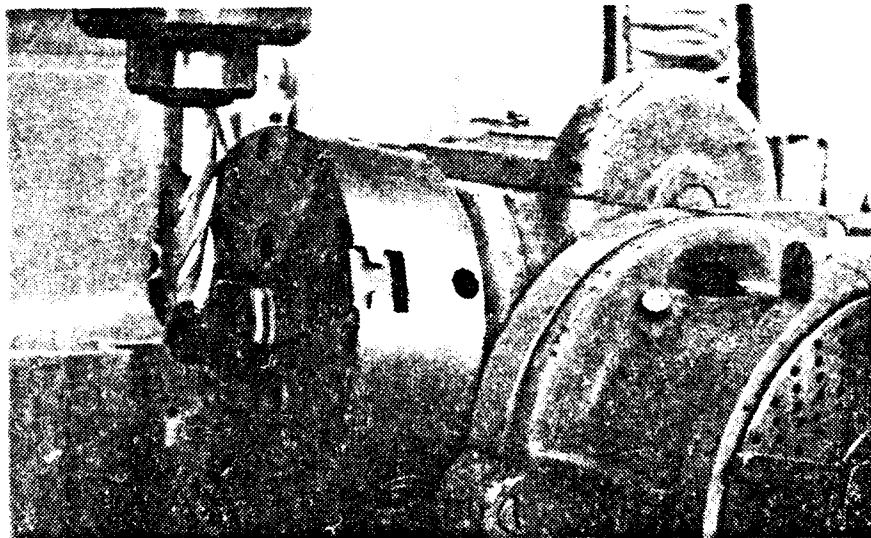


Figure 19. Machining of flat in metallographic specimen mount.

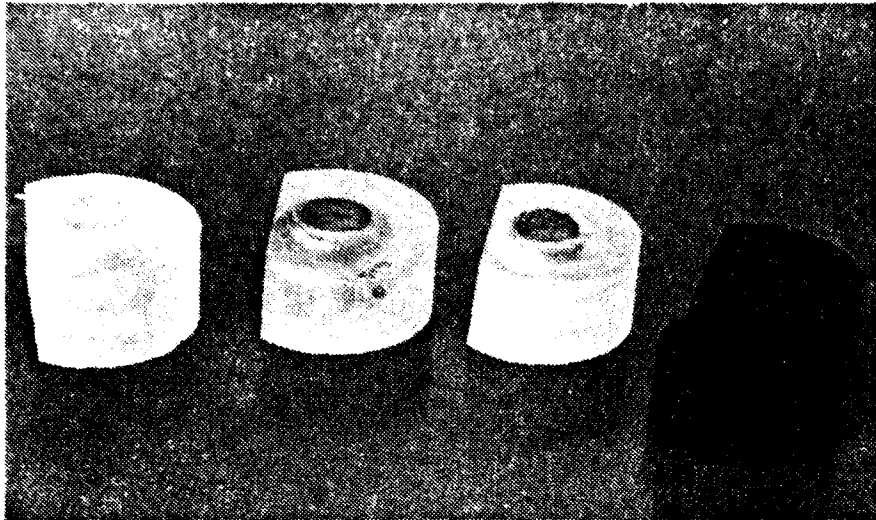


Figure 20. Machined specimen mounts with varying angles ( $\theta_0$ ).

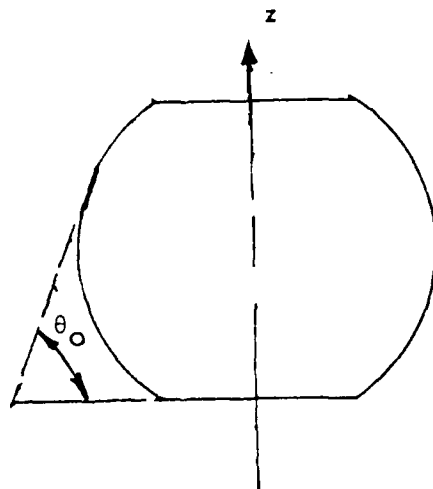


Figure 21. Polished spot orientation on obturator and relationship to  $\theta_0$ .

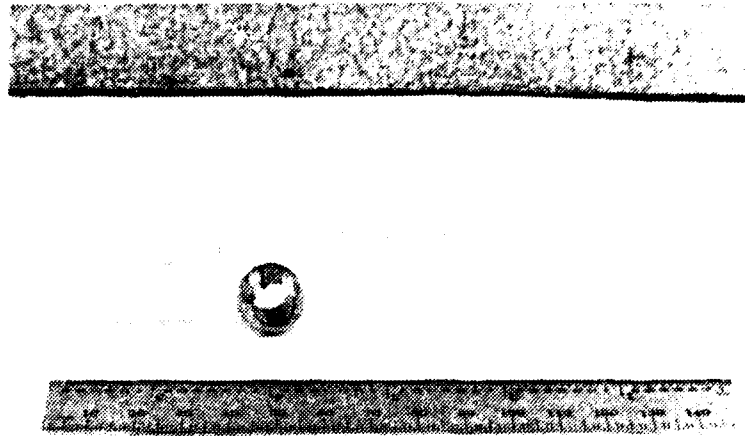


Figure 22. Obturator and components of lucite obturator housing with mating ends of inner cylinders machined to house the obturator.

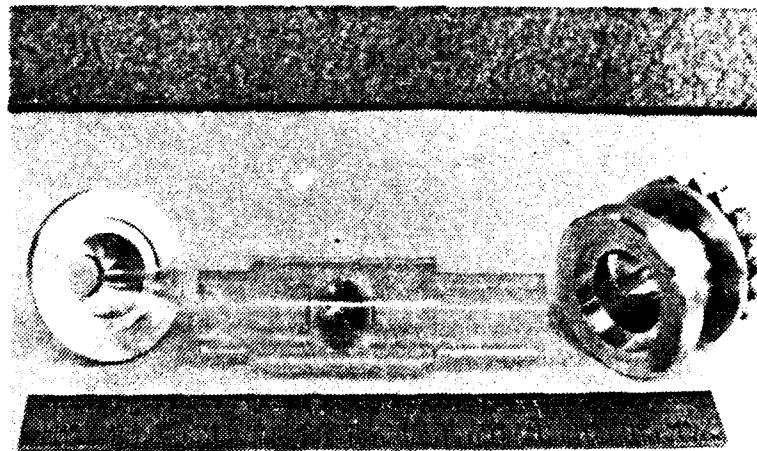


Figure 23. Assembled obturator housing with aluminum end pieces.

over the others after the obturator was inserted to insure alignment of the inner pieces and provide rigidity (Fig. 23). The ends of this lucite assembly were then press fit into aluminum end-pieces similar to those in Fig. 23. These end-pieces served as the shaft for the bearings and one also served as the prime mover (bucket wheel) for the apparatus. The shaft rotated in two ball bearings mounted in aluminum pillow blocks aligned on a rigid pedestal. The prime mover was a bucket wheel machined from a solid aluminum disk (Fig. 24).

The bucket wheel was driven by compressed air supplied from an installed system through an air filter to a manifold and then through one of two Model-10 Kendall pressure regulators. From the regulator, the air passed through a flexible tube to a tee, each leg of which supplied a nozzle. These nozzles were mounted opposite one another on the pillow block in such a way as to allow the air jet to impinge upon the bucket wheel to cause rotation (Fig. 25). The speed of rotation was sensed by a Bentley Nevada Proximitor, Model 3100N, which was mounted above the bucket wheel to detect the passage of each point on the wheel. The sensor was supplied from a LAMBDA Regulator Power Supply Model LP413FM by 18VDC. The pulses generated by the sensor were counted, averaged and displayed as a frequency by a Monsanto Programmable Counter-Timer Model 110B.

While the spin-up rig was being brought up to the desired speed, an air jet from a nozzle mounted rigidly on the pedestal

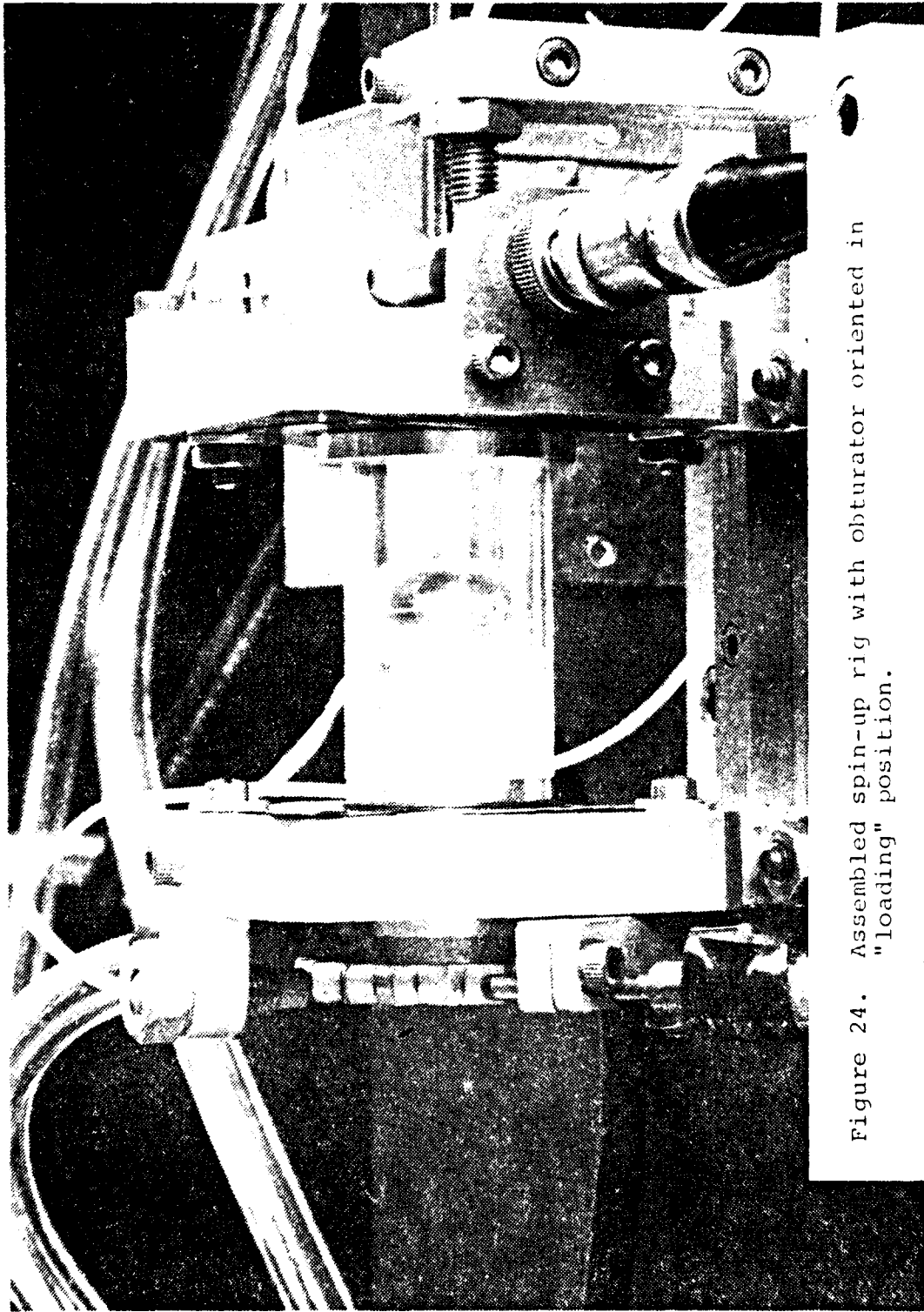


Figure 24. Assembled spin-up rig with obturator oriented in "loading" position.

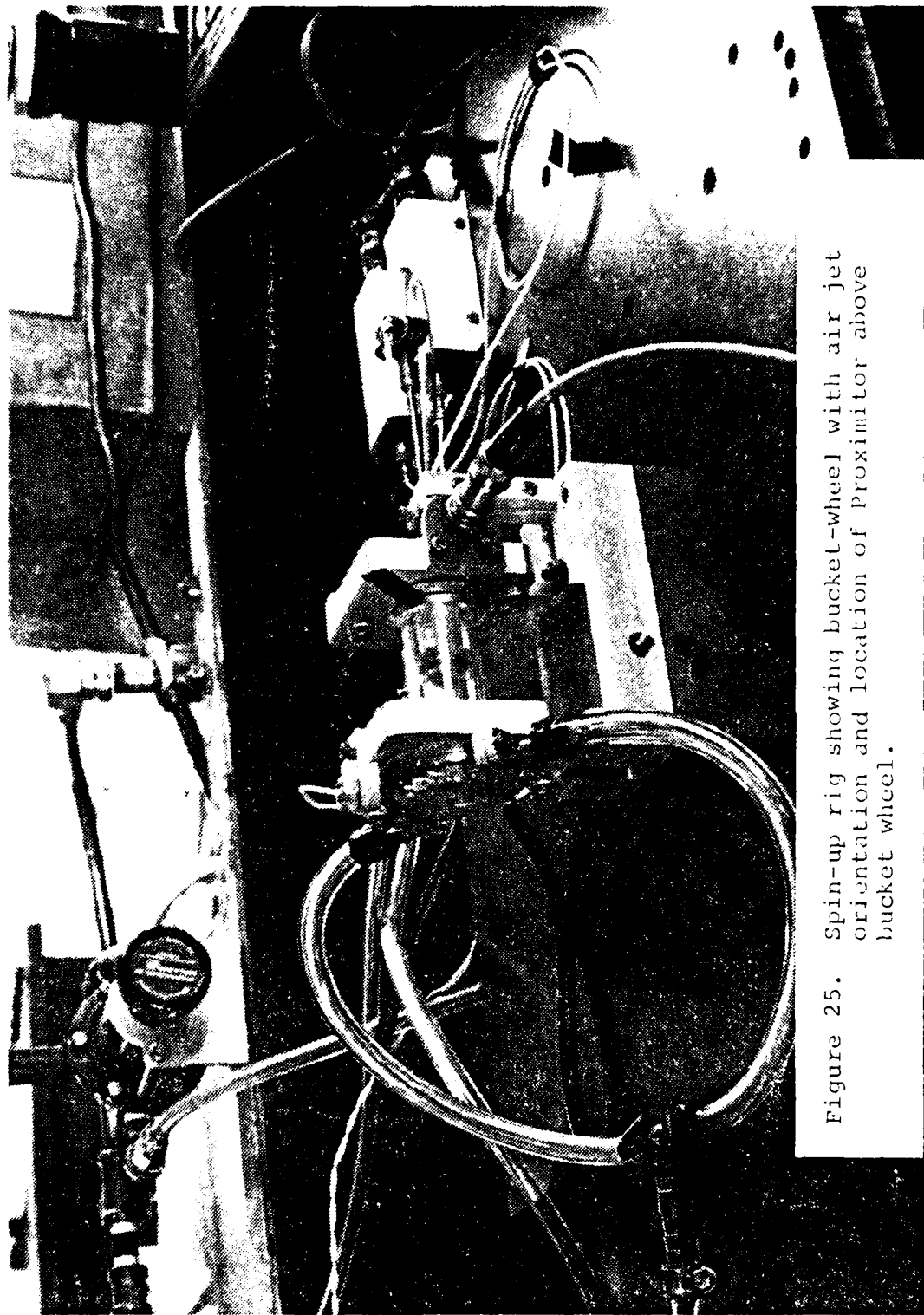


Figure 25. Spin-up rig showing bucket-wheel with air jet orientation and location of proximator above bucket wheel.

at the end opposite the bucket wheel held the obturator fixed to the spinning rig. This jet was supplied from the common air manifold and the other pressure regulator also through flexible tubing. The air jet passed through a hole in the plunger of a Rocker Solenoid, R.S. No. 10-207. This hole was aligned with the hole through the "projectile" to allow the jet to impinge upon the obturator (Fig. 26). When the switch at the far right of Fig. 26 was activated, standard 115VAC was applied to the Rocker solenoid and removed from a normally closed ASCO Solenoid Valve in the air supply line to the jet. The plunger retracted from the position shown in Fig. 26 and the solenoid valve closed. The retraction of the plunger performed three functions. It first caused a pulse to be generated by another Proximitior mounted next to the nozzle and powered from the same 18VDC supply. This pulse started the timer function of a second Model 110B Counter-Timer. The plunger also covered the nozzle outlet by misaligning its hole with that of the nozzle. This removed the restraining influence of the air jet on the obturator and prevented any air remaining in the supply line from impinging on the obturator. And lastly, in the fully retracted position, the machined and polished end of the plunger was positioned opposite the projectile hole (Fig. 27). When the released obturator nutated through enough of an angle, the beam of a SPECTRA PHYSICS MODEL 132 LASER, MODEL NO. 3187, passed through the projectile and was reflected by the polished end of the plunger into a light

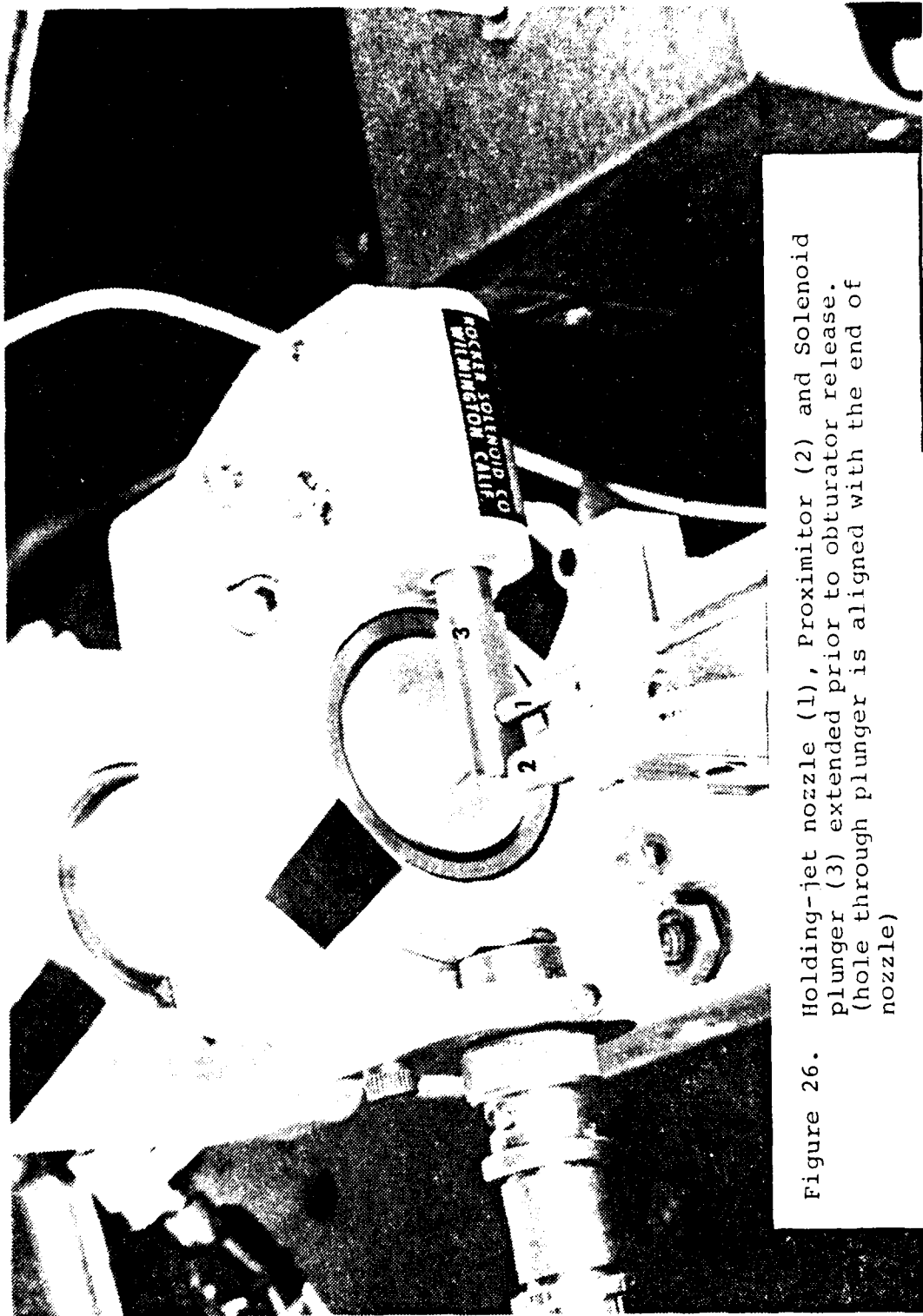


Figure 26. Holding-jet nozzle (1), Proximator (2) and Solenoid plunger (3) extended prior to obturator release. (hole through plunger is aligned with the end of nozzle)

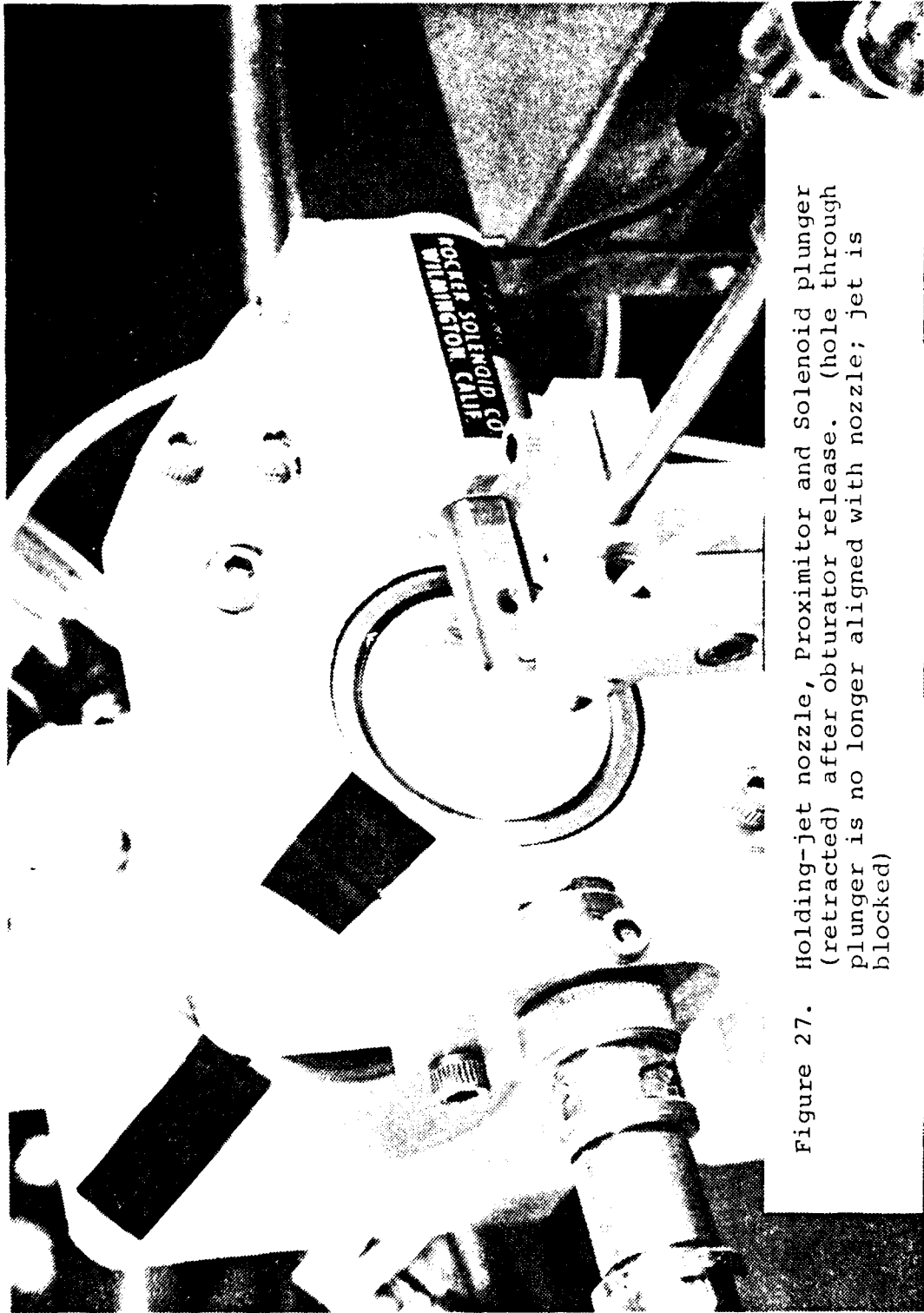


Figure 27. Holding-jet nozzle, Proximitator and Solenoid plunger (retracted) after obturator release. (hole through plunger is no longer aligned with nozzle; jet is blocked)

sensitive diode (Fig. 28). The pulse emitted by the diode triggered the stop channel on the timer and the elapsed time was displayed. Figure 29 shows the entire experimental set-up with air flasks in the background.

#### B. EXPERIMENTAL PROCEDURE

The obturator was positioned in the spin-up rig in such a way that the laser beam was reflected off the polished spot back to the target mounted on the laser (Figs. 29 and 30). The center of the target is the location of the beam and the obturator was adjusted to place the reflected spot on the center of the target. Thus the orientation of the z-axis through the obturator was known relative to the Z-axis (laser beam) through the projectile. This is the initial value  $\theta_0$ .

The solenoid plunger was checked in position with the hole aligned with the nozzle (Fig. 26) and then air was admitted to hold the obturator in place. The pressure was then increased to the turbine to set the apparatus in motion. Figure 31 illustrates the circle traced by the reflected spot (Fig. 30) on the target. This circle facilitates alignment of the laser to insure the beam was centered through the projectile. (It can be seen in Fig. 31 that the beam was slightly off-center.) Alignment was accomplished by positioning the beam from side to side for horizontal alignment, then raising or lowering the spin-up rig's mounting platform with adjusting

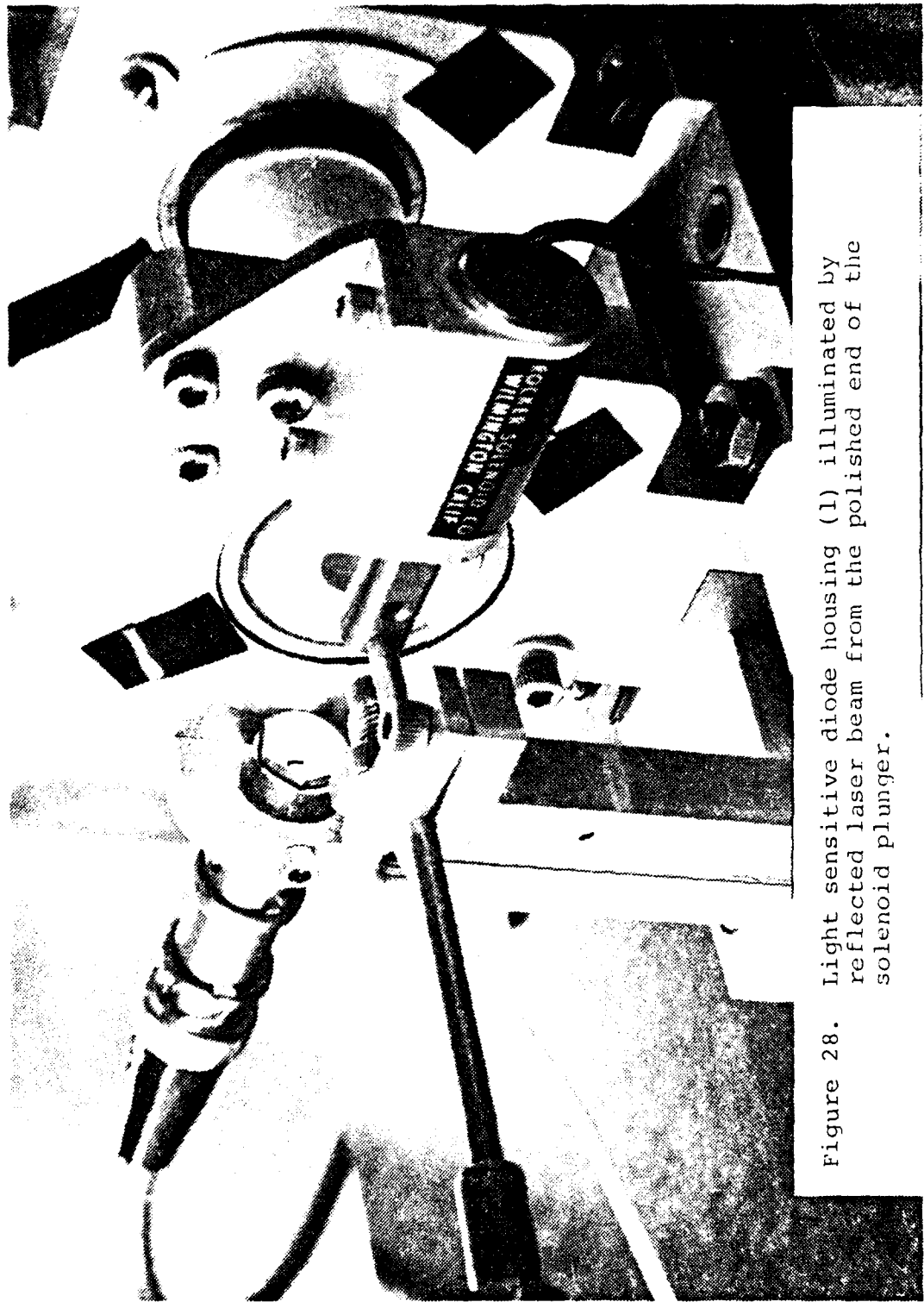
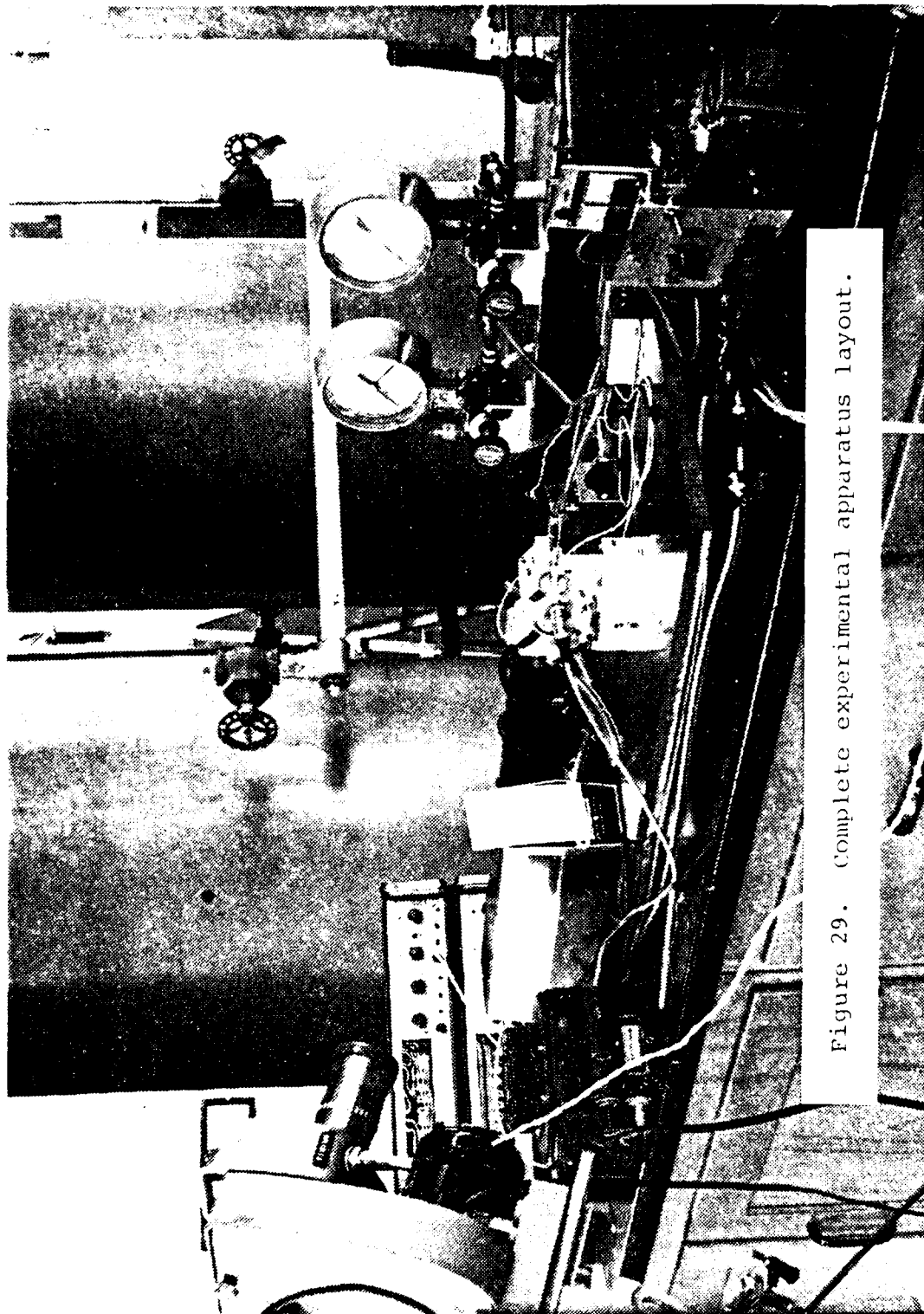


Figure 28. Light sensitive diode housing (1) illuminated by reflected laser beam from the polished end of the solenoid plunger.



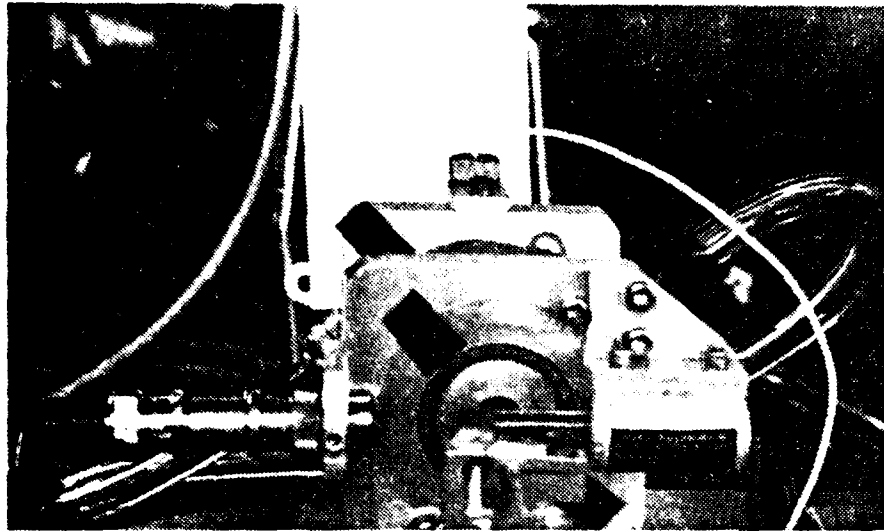


Figure 30. Laser reflection on the target from the polished spot on the obturator.

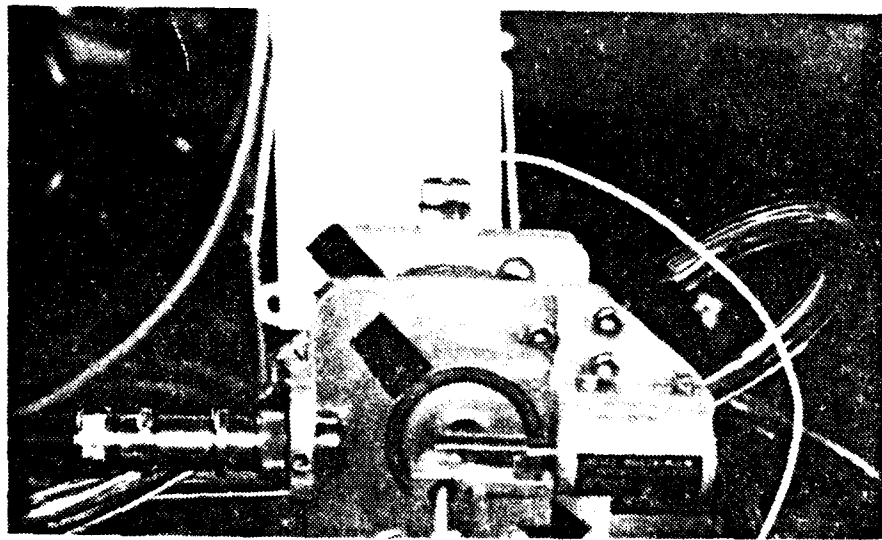


Figure 31. Circle traced by the reflected laser while the apparatus is spinning.

screws for vertical alignment. When aligned, the circular trace of the reflection exactly follows the circles of the target.

Once the alignment had been checked and the obturator positioned at the known  $\theta_0$ , the pressure was increased to the turbine nozzles until the desired spin rate was achieved. The regulator was then adjusted so as to maintain the spin rate at  $\pm 5$  Hz on the digital display or approximately  $\pm 1.75$  rad/sec. (The actual tubular projectile spin rate is approximately  $1.2 \times 10^4$  rad/sec). Once the desired rate was achieved and noted, and the timer checked and reset if necessary, the switch (Fig. 26) was activated. This secured the air to the nozzle holding the obturator and retracted the solenoid plunger (Fig. 27). The obturator was released and began to move relative to the spin-up rig. When the angle  $\theta$  reached the value at which the laser beam could pass through the obturator hole ( $\theta = \theta_{cr} = \beta$ ), the beam struck the polished plunger and was reflected into the light sensitive diode housing (Fig. 28). The reflected beam striking the diode caused the diode to emit a pulse which turned off the timer gate. The elapsed time from plunger retraction to release the obturator, to the obturator nutating to  $\theta_{cr}$  was displayed on the timer display to the 0.0001 second. This time,  $t_{cr}$ , was recorded.



### C. DATA REDUCTION

The only data reduction required was the conversion from Hz to Radians per second. The frequency read-out on the digital display indicated the number of teeth on the bucket-wheel passing the sensor in one second. Since there were eighteen teeth on the bucket wheel, the conversion was simply

$$\omega_p = \frac{f_{ro}}{18} \times 2\pi = \frac{f_{ro}\pi}{9} \text{ sec}^{-1}$$

Appendix B is a listing of the raw data and the corresponding values of  $\omega_p$ .

#### IV. CORRELATION OF RESULTS

Figures 32 through 37 show  $\theta$  vs. time for various values of  $\omega_p$  from 40 to 1000  $\text{sec}^{-1}$ . At high and low values of  $\omega_p$ ,  $\theta$  approaches zero more slowly than at the intermediate values. Figure 38 is a plot of Eq. (92) and the experimental data. The plot of Eq. (92) uses the physical qualities from Table 1 and  $\mu_s=0.35$  over the range  $100 \leq \omega_p \leq 1000 \text{ sec}^{-1}$ . It is clear that the experimental data falls below the approximation curve at high  $\omega_p$  and rises sharply above the curve at low  $\omega_p$ .

In order to determine what parameters may effect the position of the approximate curve, sensitivity checks were run on the quantities in which the most uncertainty existed, namely  $\mu_s$  and  $\theta_0$  (even though  $\theta_0$  could only vary by  $\pm 1^\circ$ ). Figures 39 and 40 indicate the sensitivity of  $t_{cr}$  to variations in  $\mu_s$  and  $\theta_0$  respectively. Small variations in  $\theta_0$  are not discernable within the range of scatter of the data (Fig. 41). Variations in  $\mu_s$  have a much more pronounced effect. From Fig. 42 it may be seen that the data at higher values of  $\omega_p$  correlate well for a  $\mu_s=0.55$ .

It has been noted that the approximate solution is based upon the assumption  $M/C\omega_p^2 \ll 1$ . At values of  $\omega_p (< 200 \text{ sec}^{-1})$ , this assumption is no longer valid and therefore calculations and correlation of the data to the approximate solution will not be conducted for  $\omega_p > 200 \text{ sec}^{-1}$ . Also at low values of  $\omega_p$ ,

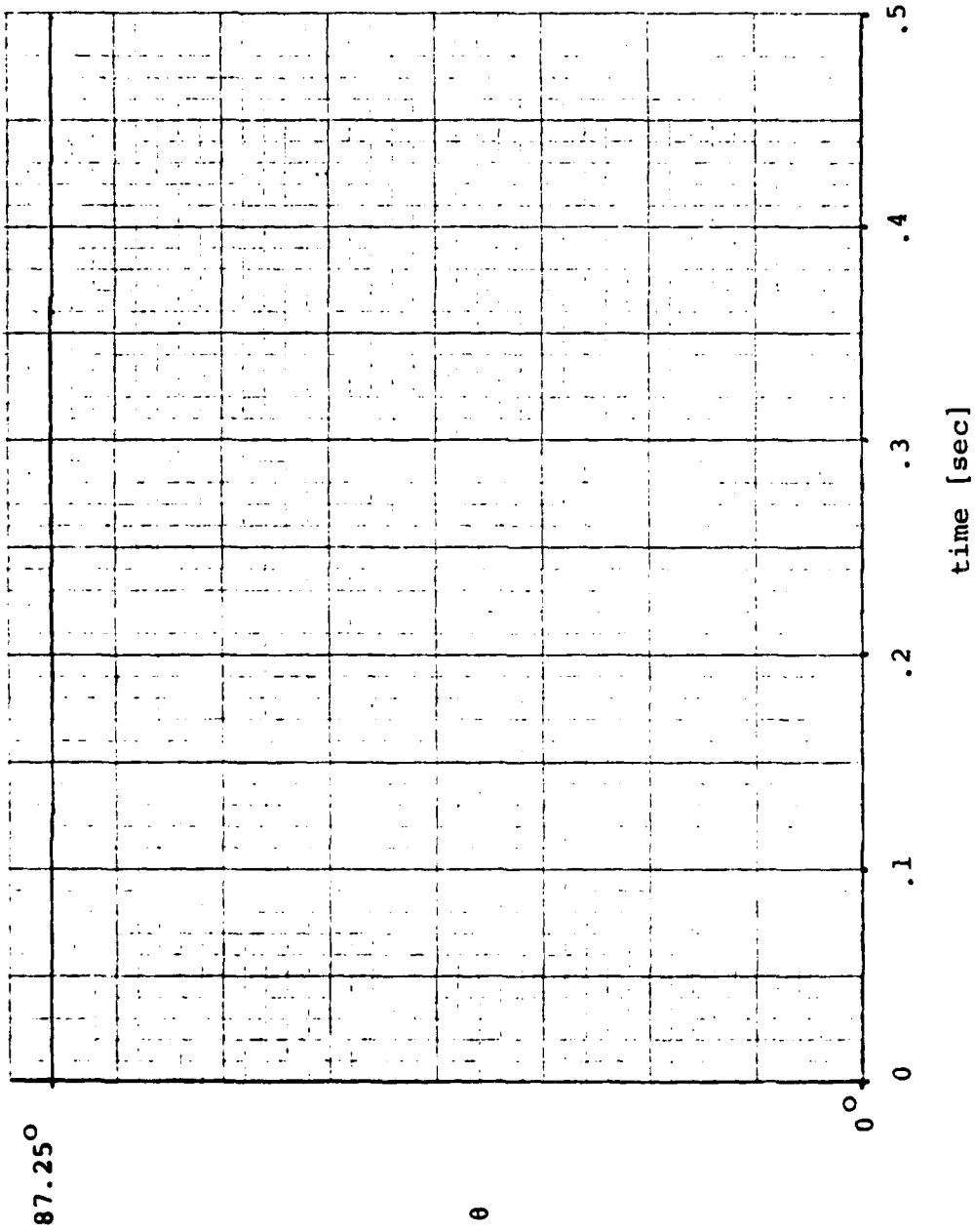


Figure 32.  $\theta$  vs. time for gravity model,  $\omega_p = 40 \text{ sec}^{-1}$

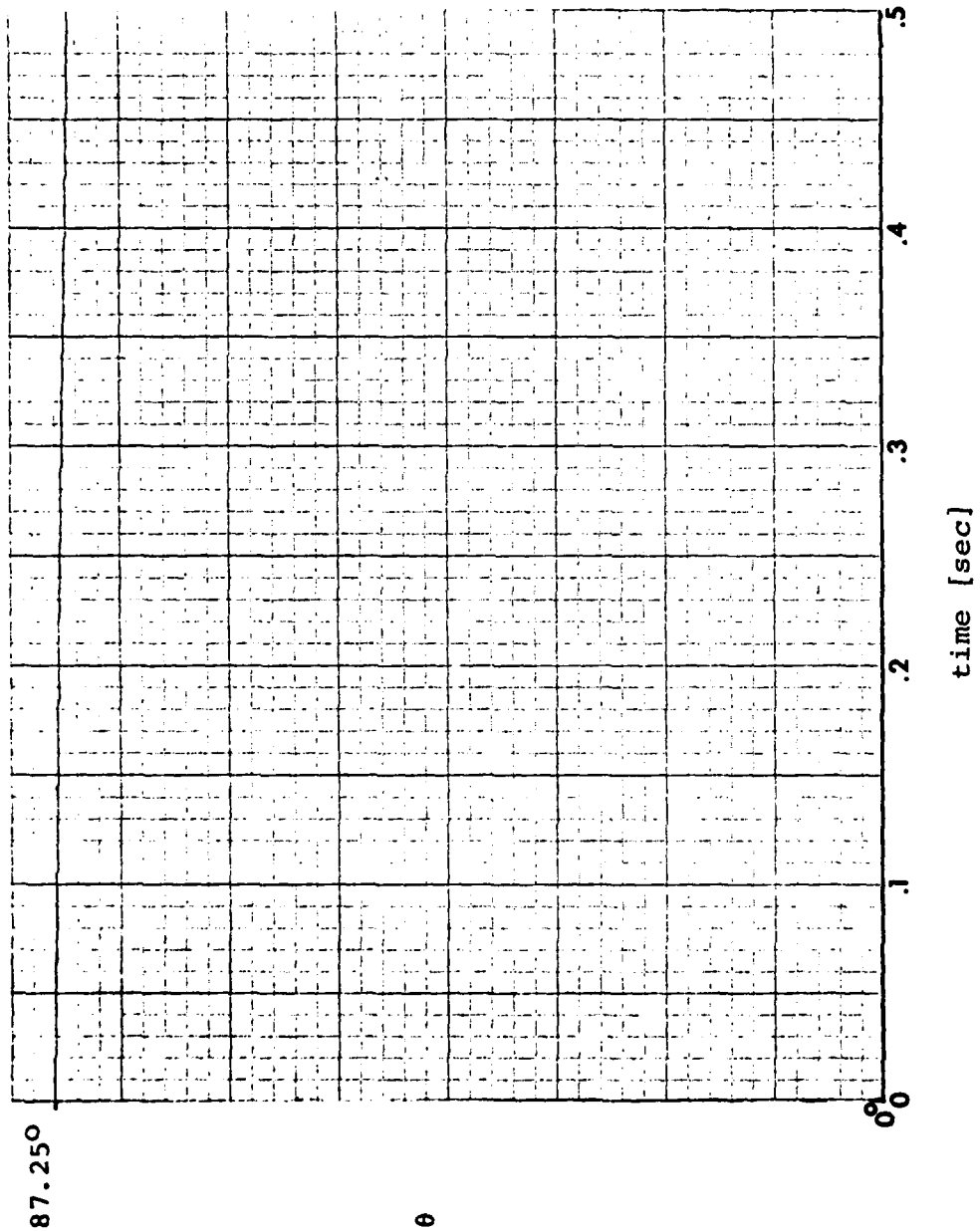


Figure 33.  $\theta$  vs. time for gravity model,  $\omega_p = 100 \text{ sec}^{-1}$

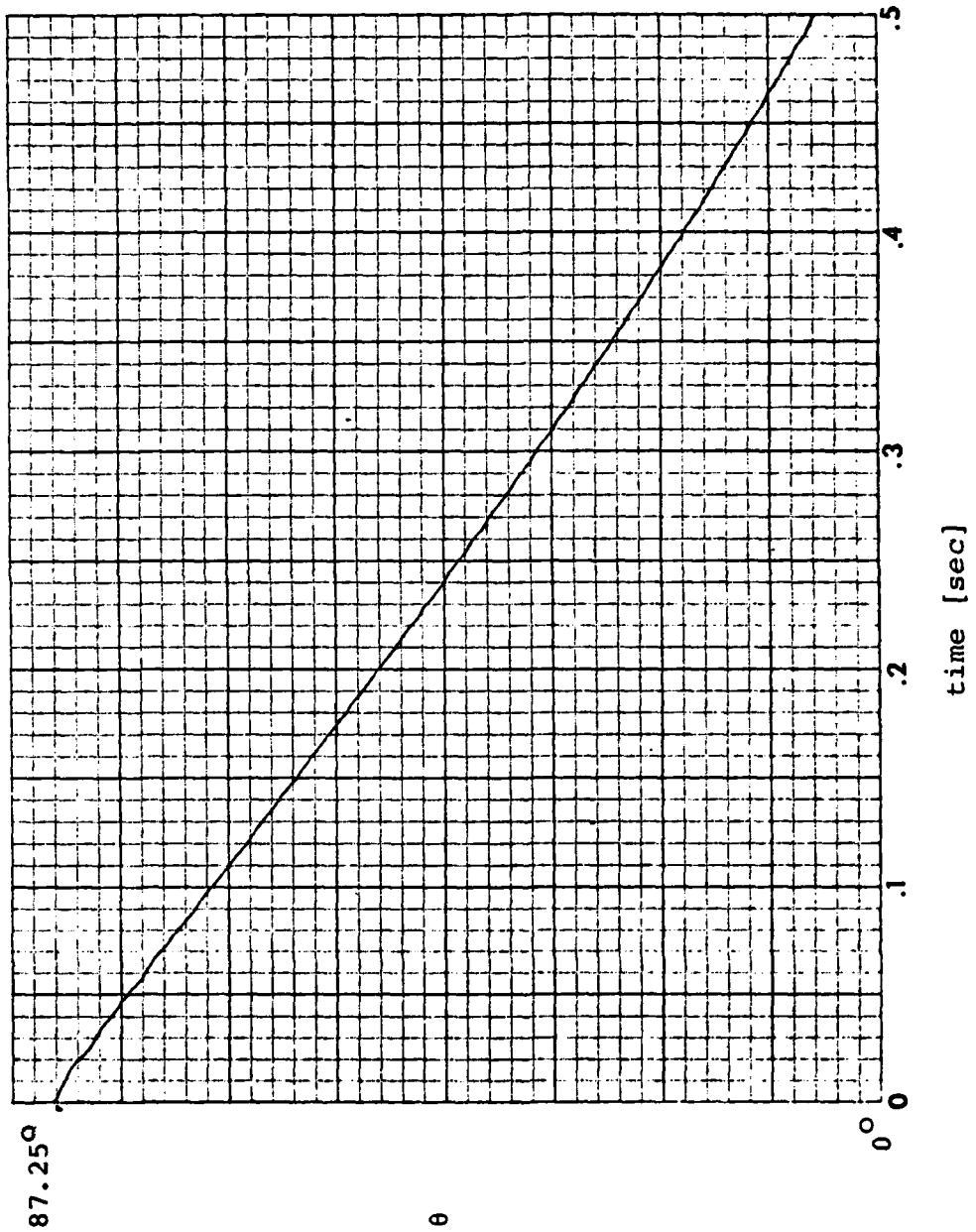


Figure 34.  $\theta$  vs. time for gravity model,  $\omega_p = 200 \text{ sec}^{-1}$

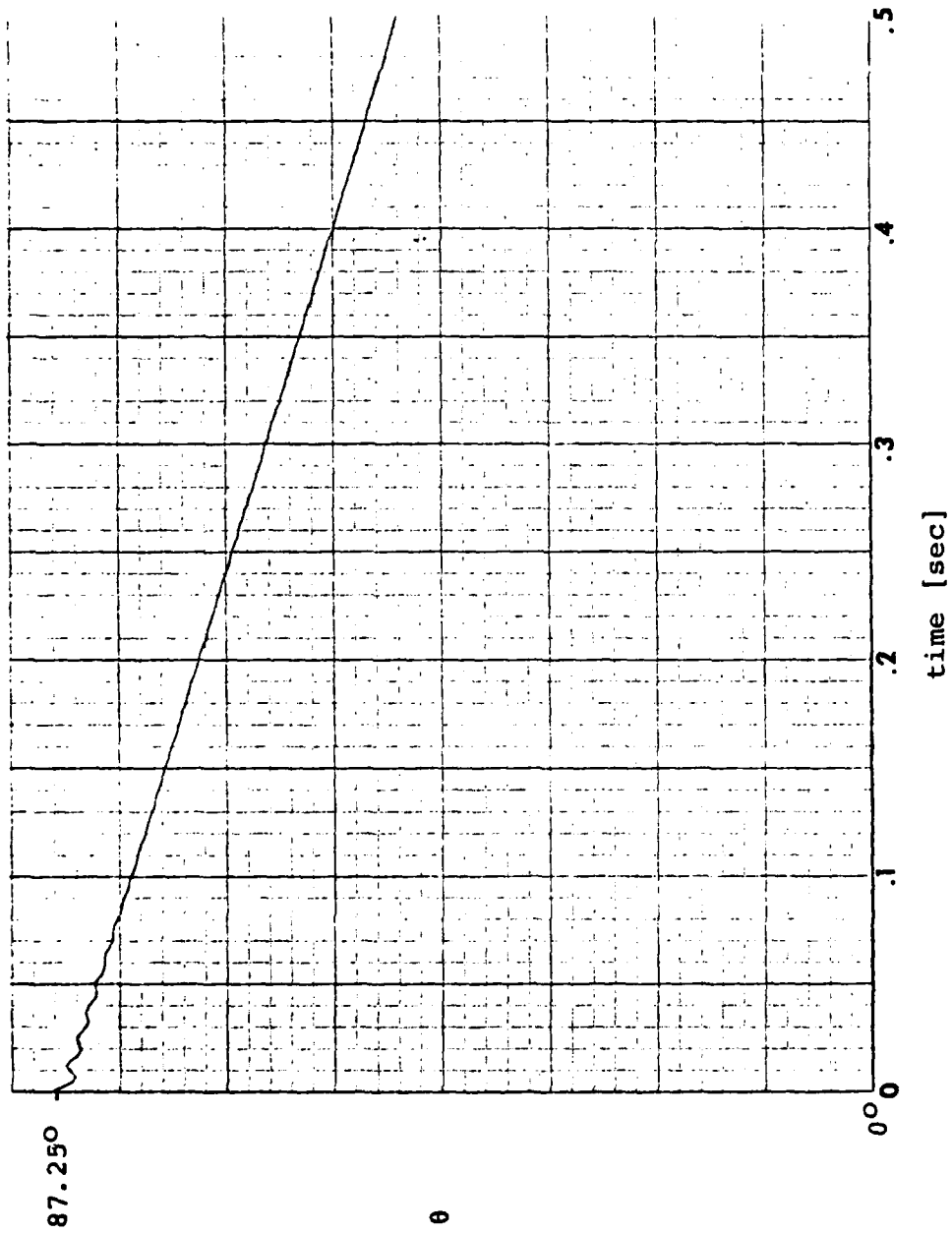


Figure 35.  $\theta$  vs. time for gravity model,  $\omega_p = 500 \text{ sec}^{-1}$

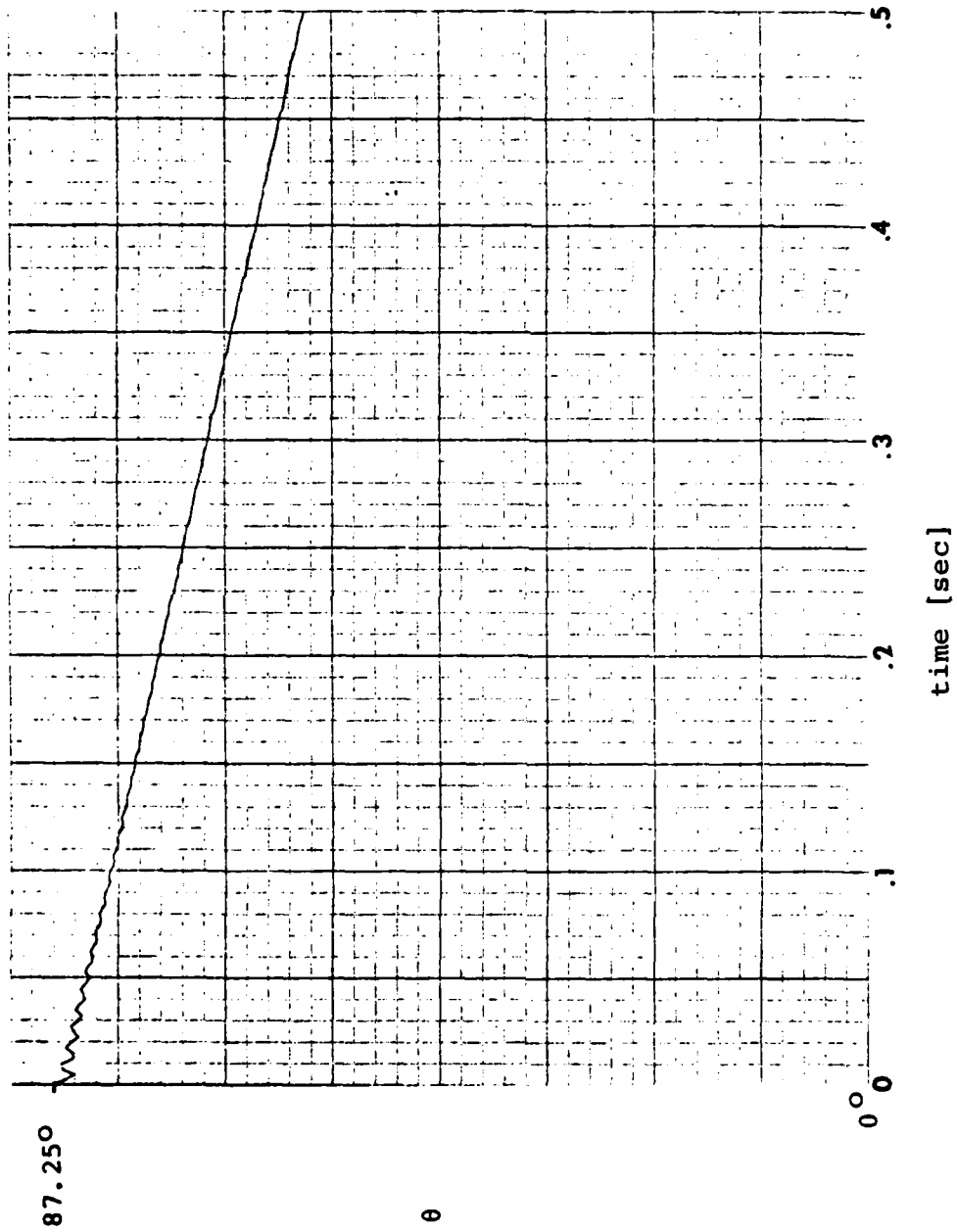


Figure 36.  $\theta$  vs. time for gravity model,  $\omega_p = 700 \text{ sec}^{-1}$

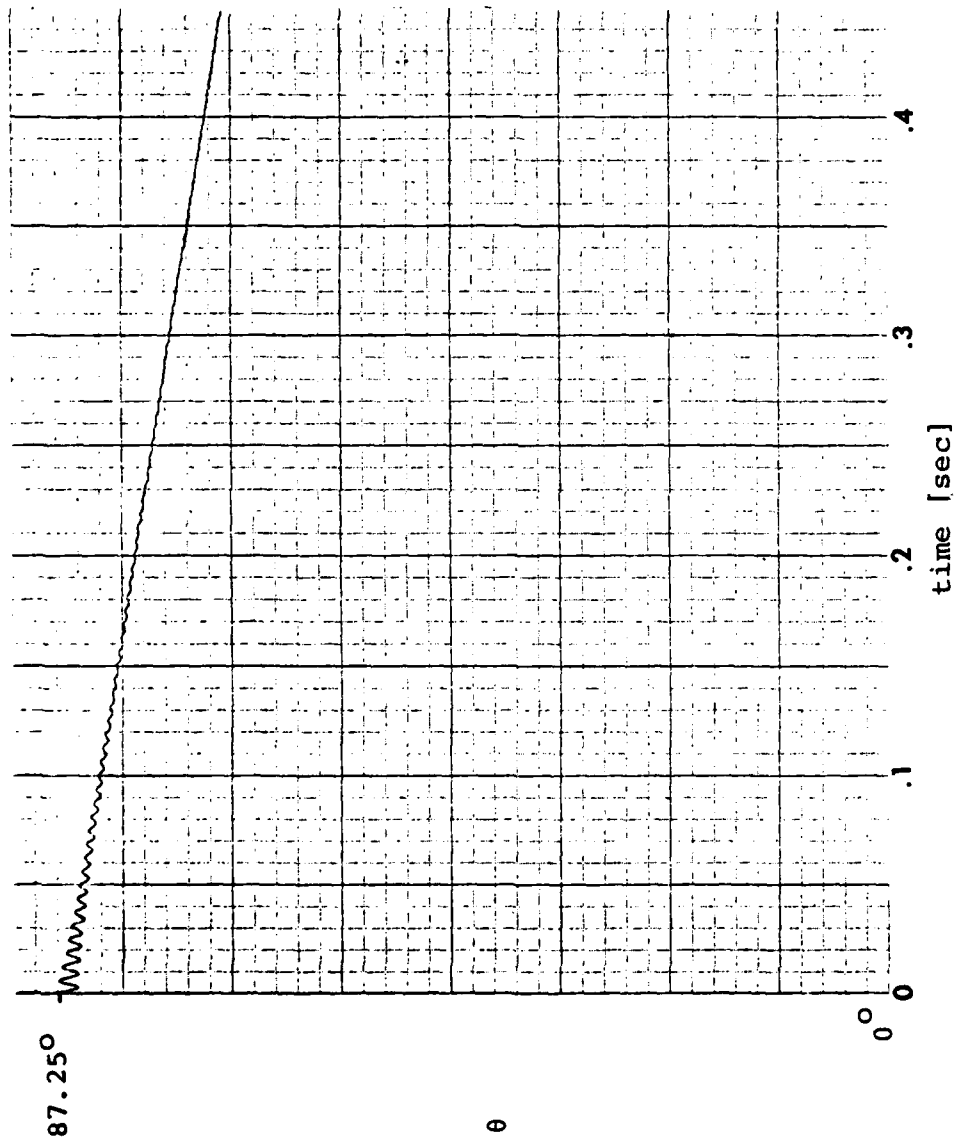


Figure 37.  $\theta$  vs. time for gravity model,  $\omega_p = 1000 \text{ sec}^{-1}$

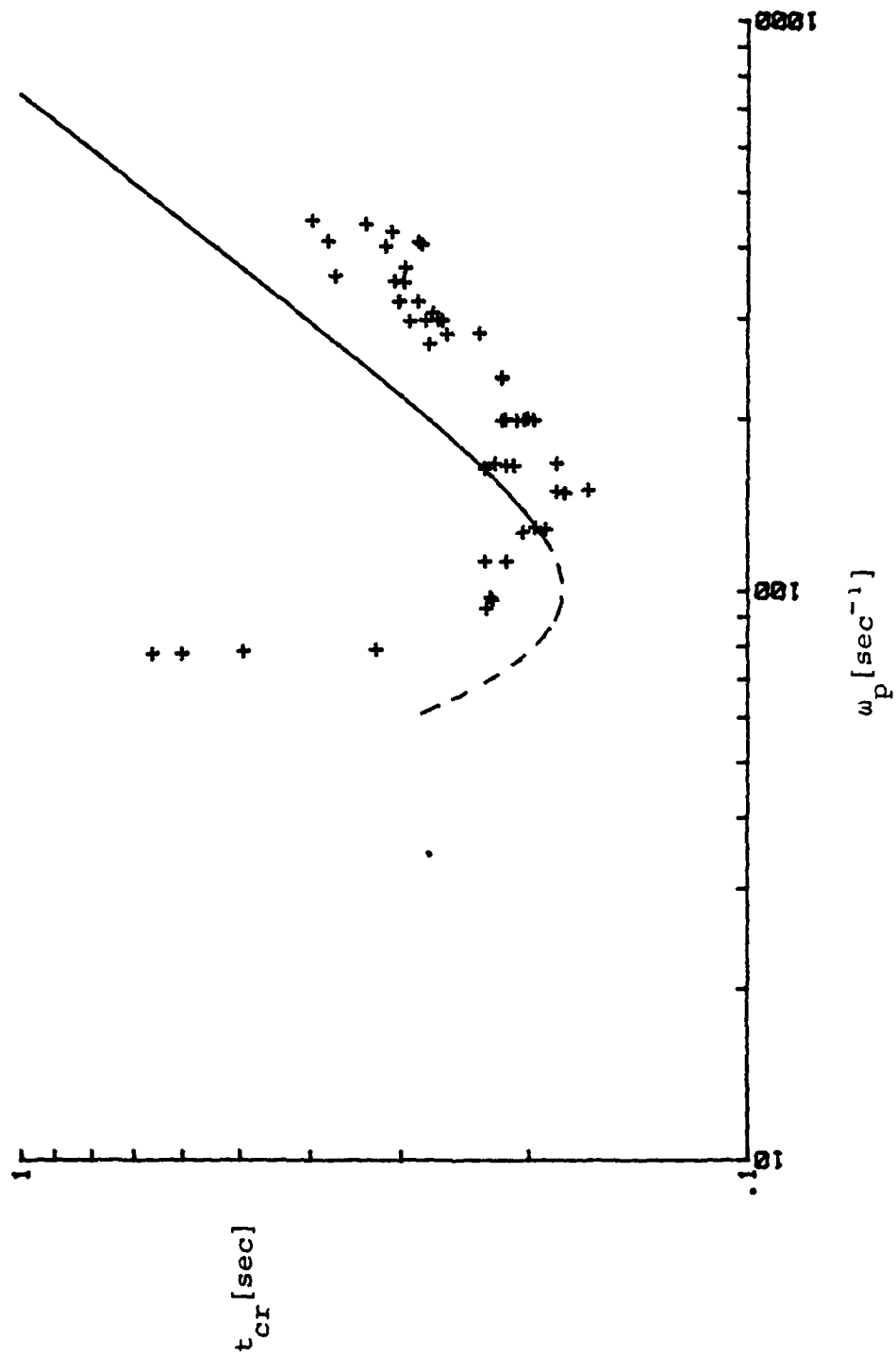


Figure 38. Experimental data and  $t_{cr}$  vs.  $\omega_p$  from Eq. (92) for  $\mu_s = 0.35$ .

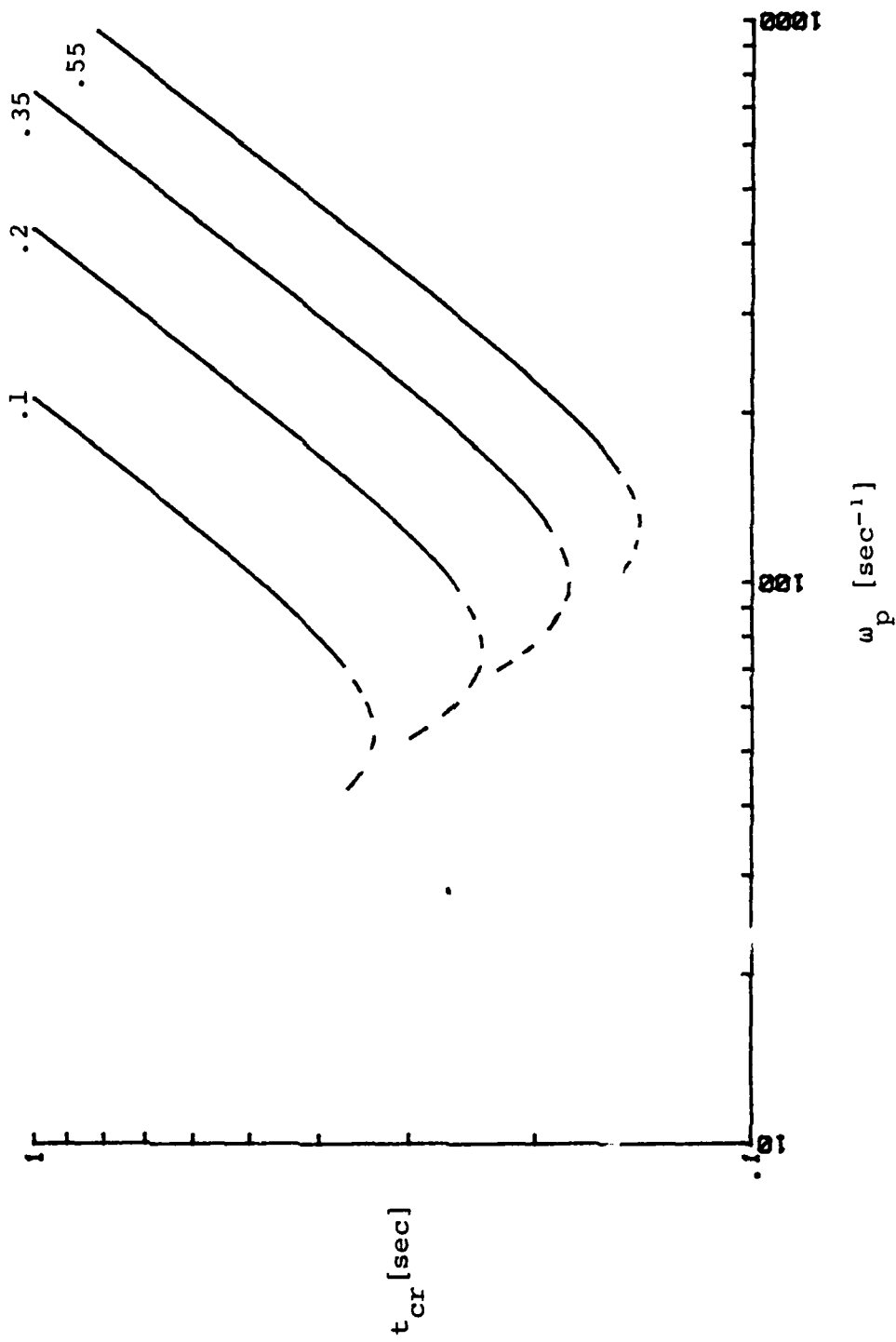


Figure 39. Plot of  $t_{cr}$  vs.  $\omega_p$  from Eq. (92) for values of  $\mu_s = 0.1; 0.25; 0.35; 0.55$

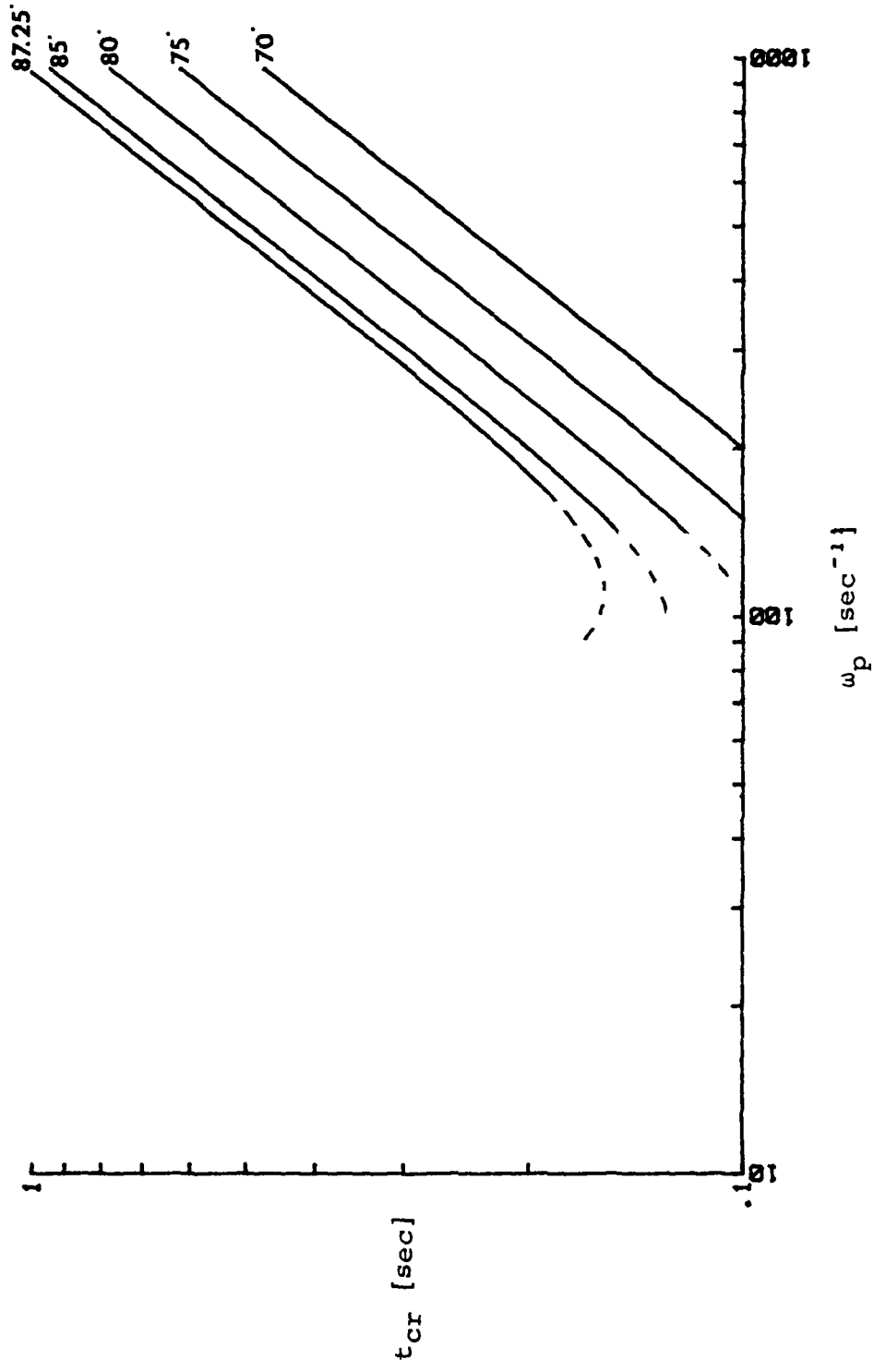


Figure 40. Plot of  $t_{cr}$  vs.  $\omega_p$  for various values of  $\theta_0$ .

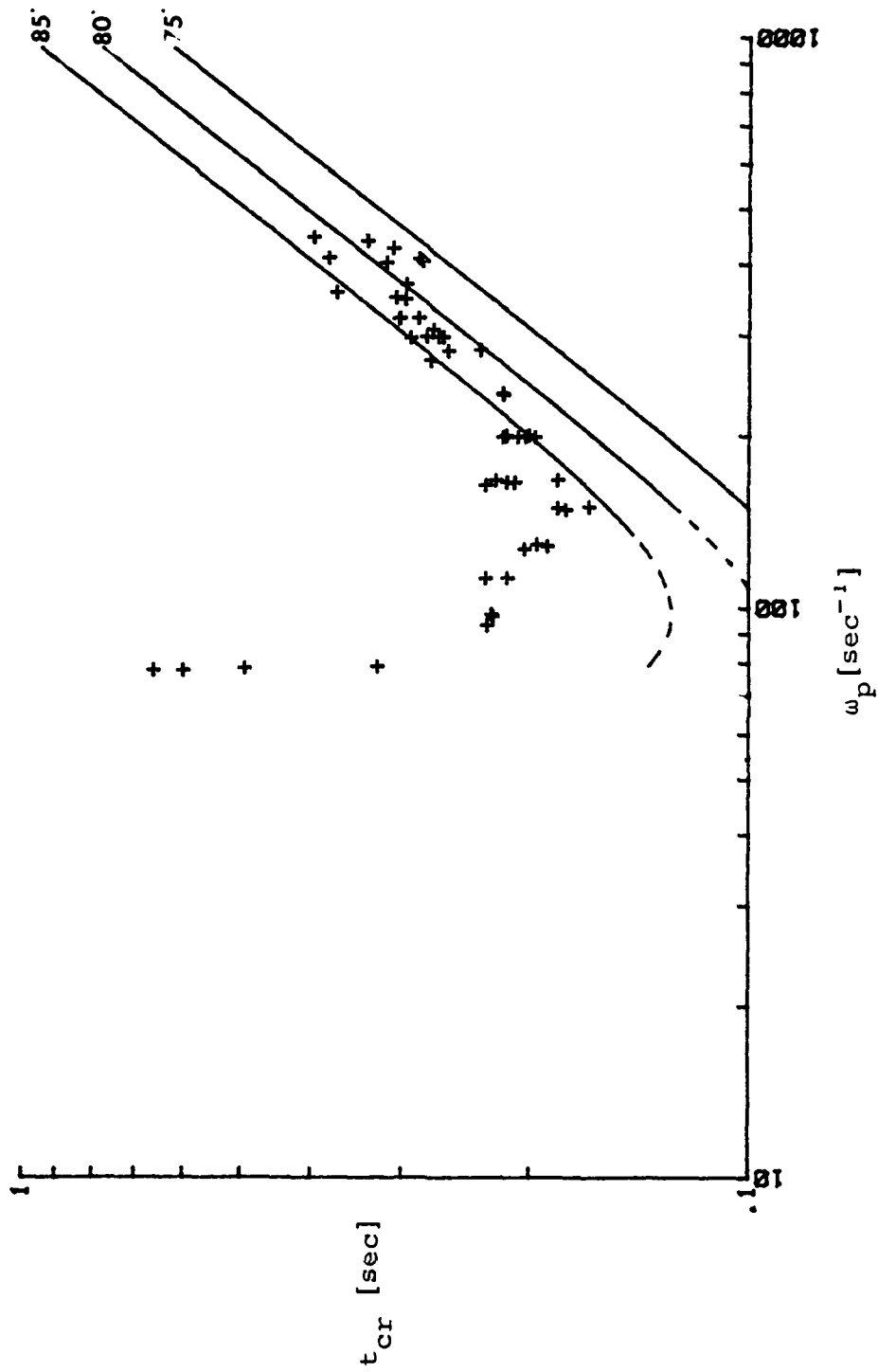


Figure 41. Plot of experimental data and  $t_{cr}$  from Eq. (92) for  $\theta_0 = 85^\circ, 80^\circ$  and  $75^\circ$

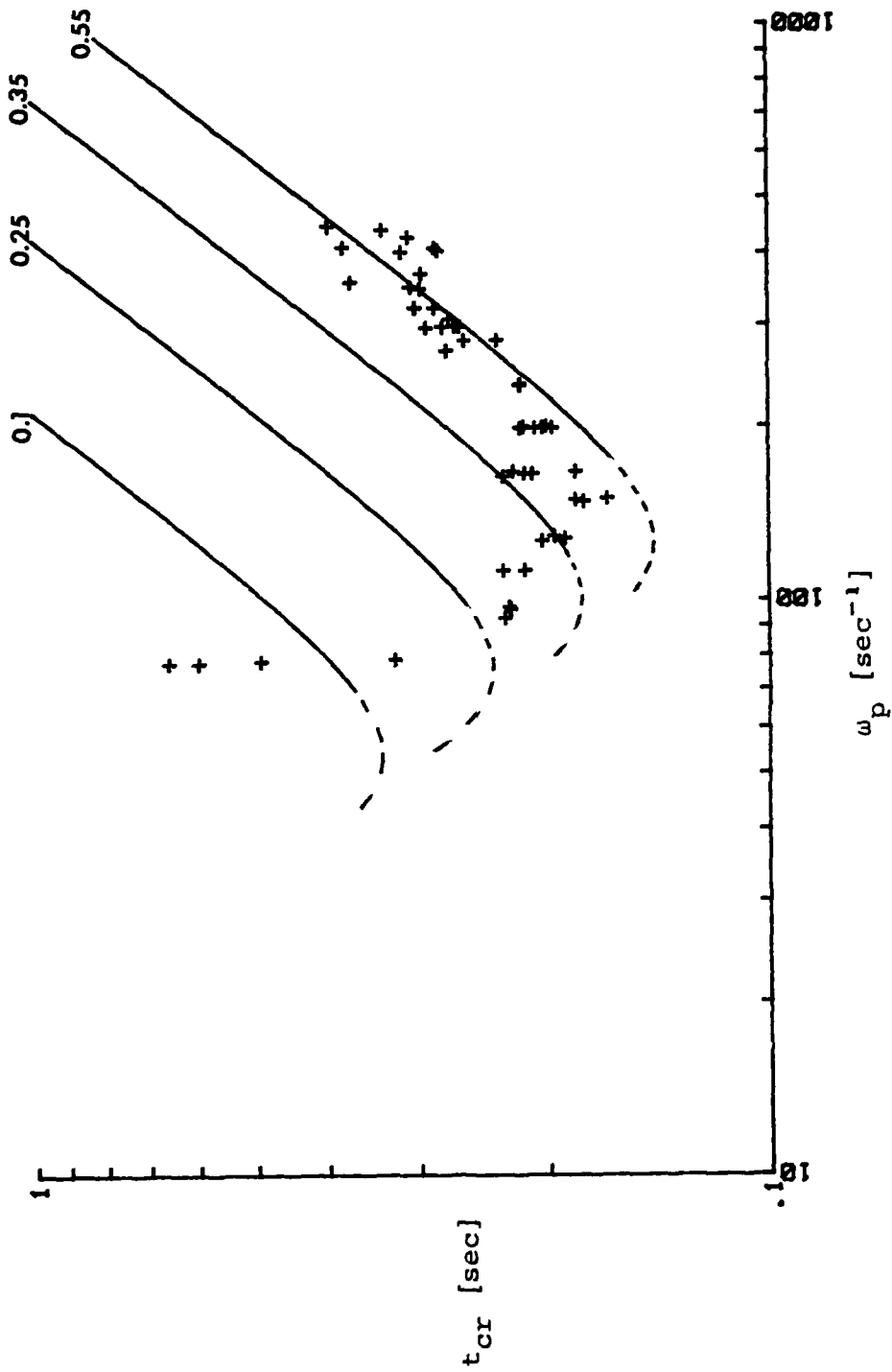


Figure 42. Experimental data and  $t_{cr}$  from Eq. (92) for  $\mu_s = 0.10, 0.25, 0.35$  and  $0.55$

$t_{cr}$  appears to approach  $\infty$  almost asymptotically. Because  $\theta_0 = 90^\circ$  ( $87.25^\circ$ ), the obturator may be near a metastable state at low  $\omega_p$  such that the coupled terms in the equations of motion have little effect. The amplitude of oscillation at low  $\omega_p$  is also relatively small.

In general, for large values of  $\zeta\omega_n t$  (Eq. 65) and neglecting the effect of viscosity,  $t$  becomes

$$t = \frac{\lambda+1}{\lambda} \frac{M}{A\omega_p^3 \cos\theta_0} + \frac{A\omega_p}{M \sin\theta_0} [(\theta_0 - \theta) - \frac{A}{2} \sin\theta_0] \quad (93)$$

where  $M$  is the gravitational contribution from Eq. (81).

This may be written as

$$t = \frac{T_1}{\omega_p^3} + T_2 \omega_p \quad (94)$$

with  $T_1$  and  $T_2$  being constants determined from the known physical parameters (Table 1). Utilizing values of  $\theta_0 = 87.25^\circ$ ,  $\theta = \theta_{cr} = \sin^{-1}(r/R_s) = 36.734^\circ$  and the measured weight of the obturator,  $W = 0.0798$  N,

$M$  is found to be

$$M = 6.34 \times 10^{-4} \bar{\mu} \text{ N-m}$$

Therefore,

$$T_1 = 2.039 \times 10^5 \bar{\mu}$$

and

$$T_2 = 3.03 \times 10^{-4} / \bar{\mu} \quad (95)$$

thus

$$t = \frac{2.039 \times 10^5}{\omega_p^3} \bar{\mu} + \frac{3.03 \times 10^{-4}}{\bar{\mu}} \omega_p$$

But for large values of  $\omega_p$ ,

$$t = \frac{3.03 \times 10^{-4} \omega_p}{\bar{\mu}} \quad (96)$$

A least squares fit of the data ( $\omega_p \geq 235.97$ ) to Eq. (96), such that  $t = \bar{T}_2 \omega_p$ , gives

$$\bar{T}_2 = \frac{\sum t_i^2}{\sum t_i \omega_{pi}}$$

Substituting in the data points (denoted by '\*' in Appendix B),

$$\sum t_i^2 = 2.1046884 \text{ sec}^2$$

$$\sum \omega_{pi}^2 = 2.8413714 \times 10^6 \text{ sec}^{-2}$$

$$\sum t_i^2 \omega_{pi}^2 = 2.430257 \times 10^3$$

therefore

$$\bar{T} = 8.6603508 \times 10^{-4} \text{ sec}^2$$

Since the standard deviation for  $\bar{T}$  is given by

$$\frac{1}{\sigma_{\bar{T}}^2} = \frac{1}{\sigma^2 \bar{T}^4} \sum t_i^2$$

where

$$\sigma^2 = \frac{1}{N} (\sum \omega_{pi}^2 - \frac{1}{T_2} \sum t_i \omega_{pi})$$

the following results are obtained:

$$\sigma^2 = 1.4659547 \times 10^3$$

$$\sigma_T^2 = 3.9181053 \times 10^{-10}$$

$$\sigma_T = 1.97742 \times 10^{-5}$$

$$\frac{\sigma}{T} = 0.023$$

The data therefore, deviates from the least squares value by only 2.3 percent.

Using the value calculated for  $T_2$  in Eq. (95),

$$\bar{\mu} = \frac{3.03 \times 10^{-4}}{8.66 \times 10^{-4}} = 0.35$$

with  $E(87.25^\circ) = 1.00458$ ,

$$\frac{\bar{r}}{R_s} = \frac{2}{\pi} (1.00448) = 0.63954$$

thus

$$\mu_s = \frac{0.35}{0.63954} = 0.5473$$

With this value of  $\mu_g$ , values of  $t_{cr}$  were obtained from the exact solution over the range  $125 \leq \omega_p \leq 700 \text{ sec}^{-1}$  and plotted with the approximation of  $t_{cr}$  from Eq. 94 and the data points (Fig. 43).

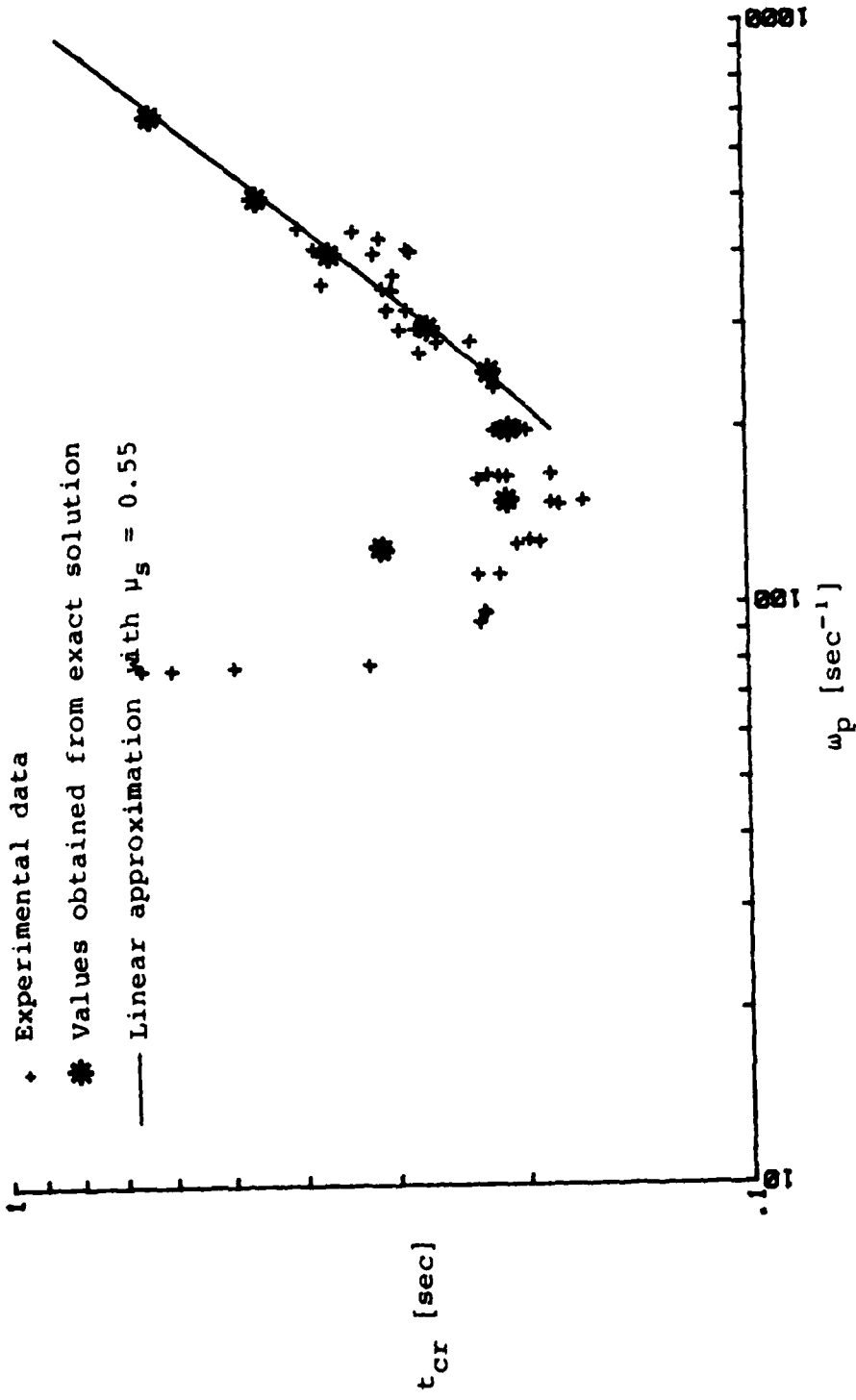


Figure 43. Experimental data, linear approximation from least squares fit and values obtained from exact solution for  $\mu_s = 0.5473$ .

## V. CONCLUSIONS

The response of the obturator ( $\theta$ ) as a function of time to applied torques was found to be that of a rigid body of revolution about its mass center. Euler's Modified Equations of Motion in terms of Euler Angles describe the response to these applied torques. The response is predictable and was compared for various combinations of physical parameters. By varying density, hole size and angular velocity, various response times may be obtained. It was found that in each case, a minimum response time was attainable for a given value of  $\omega_p$ . For the case of the experimental apparatus, this minimum occurred at  $\omega_p = 150 \text{ sec}^{-1}$ .

The analytical model and a linear approximation to this model were used with the parameters of the experimental apparatus and close agreement to the data was achieved at  $\omega_p > 200 \text{ sec}^{-1}$ . Below  $\omega_p = 200 \text{ sec}^{-1}$  the exact solution appeared to be higher and the approximate solution lower than the experimentally observed values of  $t_{cr}$ . This is explainable in the approximation since it was based upon the assumption that  $M/\omega_p^2 C \ll 1$ . At low values of  $\omega_p$ , this assumption does not hold.

The trend in the exact solution at low  $\omega_p$  is to approach  $t_{cr} = \infty$  almost asymptotically. This trend is observable in the experimental data as well and may be explained by the metastable initial position of the obturator  $\theta_0 = 90^\circ$  ( $\theta_0 = 90^\circ$  is

a stable position). The effect of the coupled terms in the equations of motion is small at low  $\omega_p$ , therefore the initial effects are not as great and the amplitude of oscillation of  $\theta$  is insufficient to cause departure from this metastable position. Since the actual projectile operates at  $\omega_p=12,000$   $\text{sec}^{-1}$ , high values of  $\omega_p$  are of interest. The theory agrees well with the data above  $\omega_p=200$   $\text{sec}^{-1}$  and therefore the correlation to the data was made at these higher values.

Because the linear approximation agreed closely at higher  $\omega_p$ , a least squares fit of that approximate equation to the experimental data ( $\omega_p \geq 235.97$   $\text{sec}^{-1}$ ) lead to the calculation of a higher sliding friction coefficient than had been used previously. The assumed value was  $\mu_s=0.35$  for laminated plastic on steel [27]. This was found to be too low by the least squares fit. A sensitivity check of the approximate solution for  $t_{cr}$  to variations in  $\mu_s$  also indicated that 0.35 was too low (Fig. 39). Therefore, a method for determining the sliding friction coefficient from the experimental data and the approximate solution was discovered.

By knowing initial orientation ( $\theta_0$ ), projectile spin rate ( $\omega_p$ ) and the physical dimensions and material properties of the projectile, the response may be predicted in a gravity environment with reasonable accuracy.

The aerodynamic model appears to give reasonable results within the scope of this study. The complex forces acting on

the obturator in flight are extremely difficult to model theoretically and therefore they were simplified greatly. The confidence gained in the gravity model, however, leads to the conclusion that once the complex aerodynamic forces are better understood, the motion of the ball within the flight model will be predictable.

## VI. RECOMMENDATIONS

Further experimentation should be undertaken with variation of other parameters (hole size, obturator material) to obtain more confidence in the analytical model. Wind tunnel tests of the BOT should be conducted in order to more closely approximate the actual forces on the obturator in flight, and to determine the position ( $\theta$ ) at which the detached bow shock is swallowed. This would greatly enhance the predictive capabilities of the model and thus allow coupling to a trajectory model for predicting flight characteristics. This, in turn, could be coupled to a numerical optimization routine for optimizing the BOT design for the desired performance criteria.

APPENDIX A - COMPUTER CODE

```

*****
* BALL OBTURATED TUBULAR PROJECTILE *
* BALL MOTION ANALYSIS *
* LT J. W. BLOOMER II, USN *
*****
DIMENSION X(30),XDOT(30),C(15)
C(1)= (SIN(BETA))**2, WHERE BETA IS GIVEN BY ARSIN(RP/RO)
C(2)= LAMBDA = (C-A)/A
C(3)= AERODYNAMIC OR GRAVITATIONAL SLIDING FRICTION CONSTANT.
C(4)= TOTAL KINETIC ENERGY OF COMBINED PROJECTILE AND OBTURATOR.
C(5)= MINIMUM MOMENT OF INERTIA, A.
C(6)= MAXIMUM MOMENT OF INERTIA, C.
C(7)= MOMENT OF INERTIA OF A FOLLOW CIRCULAR CYLINDER
APPROXIMATING THAT OF THE PROJECTILE.
C(8)= FLUID FRICTION CONSTANT, S.
C(10)=1.

*****CALL INTEG2 SIMULTANECUS DIFF. EQN. SOLVER

1 CALL INTEG2(T,X,XDOT,C)

*****DEFINE EULER ANGLES THETA, PHI AND PSI AND 1ST DERIVATIVES

TH=X(1)
XDCT(1)=X(2)
PS=X(3)
XDCT(3)=X(4)
PH=X(5)
XDCT(5)=X(6)

*****DEFINE TRIGONOMETRIC FUNCTIONS OF EULER ANGLES

STH=SIN(TH)
CTH=COS(TH)
SPH=SIN(PH)
CPH=COS(PH)
SPS=SIN(PS)
CPS=COS(PS)

*****DEFINE THETA-DOT, PHI-DOT AND PSI-DOT

THC=XDOT(1)
PSD=XDOT(3)
PHD=XDOT(5)

*****CALCULATE ANGULAR VELOCITIES WITH RESPECT TO BODY-
FIXED AXES A, B, AND C RESPECTIVELY.

OM1=PSD*STH*SPH+THC*CPH
OM2=PSD*STH*CPH-THC*SPH
OM3=PSD*CTH+PHD

*****CALCULATE ANGULAR VELOCITIES ABOUT INERTIAL AXES X, Y, AND
Z RESPECTIVELY.

OMX=OM1*(CPH*CPS-SPH*CTH*SPS)+OM2*(-SPH*CPS-CPH*CTH*SPS)
+OM3*(STH*SFS)
OMY=OM1*(CPH*SFS+SPH*CTH*CPS)+OM2*(-SPH*SFS+CPH*CTH*CPS)
+OM3*(-STH*CPS)
OMZ=OM1*STH*SPH+OM2*STH*CPH+OM3*CTH

*****CALCULATE THE ANGULAR VELOCITY OF THE PROJECTILE
FROM CONSERVATION OF ENERGY PRINCIPLES.

```

```

SPIN=0.0
SPIN=SQRT((2.*C(4)-C(5)*(OM1**2+OM2**2)-C(6)*OM3**2)/C(7))
C*****CALCULATE ANGULAR VELOCITY OF BALL RELATIVE TO THE PROJECTILE
C WITH RESPECT TO BODY-FIXED AXES.
OM1R=OM1-SPIN*SPH*STH
OM2R=OM2-SPIN*CPH*STH
OM3R=OM3-SPIN*CTH
C*****CALCULATE RELATIVE ANGULAR VELOCITIES WITH RESPECT TO
C THE INERTIAL REFERENCE FRAME.
OMXR=OM1R*(CPH*CPS-SPH*CTH*SFS)+OM2R*(-SPH*CPS-CPH*CTH*SFS)
+OM3R*(STH*SFS)
OMYR=OM1R*(CPH*SPS+SPH*CTH*CPS)+OM2R*(-SPH*SPS+CPH*CTH*CPS)
+OM3R*(-STH*CPS)
OMZR=OM1R*STH*SPH+OM2R*STH*CPH+OM3R*CTH
C*****CALCULATE MAGNITUDE OF RELATIVE ANGULAR VELOCITY VECTOR.
OMR=SQRT(OMXR**2+OMYR**2+OMZR**2)
C*****CALCULATE THE MOMENT ARM AT WHICH THE FRICTIONAL FORCES ACT.
ARM= MOMENT ARM AND C(1) IS AS DEFINED EXCEPT IN THE CASE OF
GRAVITY WHERE C(1) = 1.0.
FRIC= COMBINED FLUID AND SLIDING FRICTION CONSTANTS.
ARM=SQRT(1.-C(1)*(OMXR/OMR)**2-(1.-C(1))*(OMZR/OMR)**2)
FRIC=C(3)*ARM
AMCM=C(8)*CMP+FRIC
C*****CALCULATE MOMENTS ACTING ON THE BALL ABOUT THE BODY-FIXED
C AXES.
G1=-AMCM*OM1R/OMR
G2=-AMCM*C*2F/OMR
G3=-AMCM*C*3P/OMR
C*****CALCULATE ELEMENTS OF MATRIX OF COEFFICIENTS, Y1, Y2 AND Y3.
Y1=G1/C(5)-PSD*(THD*CTH+SPH*PHD*STH+CPH)+THD*PHC*SPH-C(2)*
*(PSD*STH*CPH-THD*SPH)*(PSD*CTH+PHD)
Y2=G2/C(5)-FSC*(THD*CTH*CPH-PHD*STH*SPH)+PHC*THC*CPH+C(2)*
*(PHD+PSD*CTH)*(PSD*STH*CPH+THD*CPH)
Y3=G3/C(6)+FSC*THD*STH
C*****CALCULATE ANGULAR ACCELERATION TERMS FOR INTEGRATION, 2ND
C DERIVATIVES OF RULER ANGLES WRT TIME.
XDOT(2)=CPH*Y1-SPH*Y2
XDCT(6)=-SPH*CTH/STH*Y1-CTH*CPH/STH*Y2+Y3
XDCT(4)=SPH/STH*Y1+CPH/STH*Y2
C*****CALCULATE VALUES FOR THE APPROXIMATE SOLUTION
THCRIT=.6411
IF(T.NE.C.CCC0000) GO TO 25
THNOT=X(1)
OMP=X(4)
ERTC=C(6)
A=C(5)
AMCA=C(2)
AMCAP=AMCA+.1
EM=C(3)*.62E-4
D=-AMDA/2.*SIN(2.*THNOT)
R=-AMCAP*.1.*SIN(THNOT)/(ERTC*OMP)
TCRIT=-1./R*(THNOT-THCRIT)-D/R
WRITE(6,2) TCRIT
20 FCRMAT(5X,TCRIT = .E16.8)
ZETA=4MDAP/(2.*A*AMDA*CF=CMP*CGS(THNOT))*EM

```

```

IF(ZETA.GT.1.0)GO TO 25
DZETA=SQRT(1.-ZETA*ZETA)
PHASE=ATAN(CZETA/(ZETA*(1.-2./(4.*ZETA*ZETA-AMDAP))))
THPROX=THNOT+C/R/OMP*(-2.*ZETA)+1./ZETA*SIN(PHASE)
GO TO 26
25 THPROX=THNOT+Q/R/OMP*(CMP*T-2.*ZETA)+1./(EXP(ZETA*OMP*T)*DZETA)*
*SIN(OMP*T*CZETA+PHASE)
26 X(7)=THPROX
X(9)=OMZ
X(13)=SPIN
GO TO 1
END

```

APPENDIX B - RAW DATA

READOUT [Hz]	TIME [sec]	$\omega_p$ [sec <sup>-1</sup> ]	READOUT [Hz]	TIME [sec]	$\omega_p$ [sec <sup>-1</sup> ]
776	.274	270.88*	880	.2717	307.2*
676	.218	235.97*	920	.3026	321.14*
679	.2181	237.02*	920	.2847	321.14*
573	.2157	200.01	936	.2816	326.7*
570	.2079	198.97	983	.2699	343.1*
574	.2009	200.36	1001	.306	349.4*
570	.197	198.97	994	.2972	346.97*
571	.2031	199.32	1055	.296	368.26*
475	.2099	165.8	1063	.2530	371.06*
479	.1833	167.2	1151	.315	401.77*
570	.2179	198.97	1022	.369	356.7 *
475	.215	165.8	1175	.378	410.15*
479	.223	167.2	1258	.3348	439.12*
470	.230	164.1	1278	.3968	446.1 *
428	.1831	149.4	1255	.4268	438.08*
425	.1786	148.35	1221	.3088	426.2 *
430	.1659	150.1	1170	.284	408.4 *
367	.1896	128.1	1158	.281	404.2 *
363	.2037	126.7			
370	.1959	129.15			
277	.2249	96.7			
267	.2292	93.2			
279	.2259	97.4			
323	.230	112.7			
323	.2149	112.7			
225	.493	78.5			
223	.658	77.8			
223	.599	77.8			
226	.3241	78.9			
807	.2592	281.7*			
810	.2339	282.7*			
853	.2773	297.8*			
853	.2631	297.8*			
850	.2917	296.7*			
854	.267	298.1*			
921	.3022	321.49*			

## LIST OF REFERENCES

1. Whitworth, Joseph, Miscellaneous Papers on Mechanical Subjects, J. and J. Thomson, 1858.
2. Ballistics Research Laboratory Report 460, Retardation of Tubular Projectiles Developed From 20-mm American Ball, by A. C. Charters and R. N. Thomas, Apr. 1944.
3. Army Ballistics Research Laboratory Technical Report 02100, On the Overall Ballistic Performance of Tubular and Non-tubular Kinetic Energy Projectiles, by Frank and McLaughlin, Sep. 1978.
4. Air Force Armament Laboratory Technical Report 75-106, Aeroballistic Range Tests of Tubular Projectiles at Mach Nos. 1.0-3.2, by G. L. Winchenbach, et. al., August 1975.
5. Fackner, W. P., Concept Evaluation of Tubular Round for Vulcan, USARADBD-195, May 1978.
6. Naval Weapons Center China Lake Technical Memorandum 4106, Vol. 4, Advanced Armor Penetrator (Tubular Projectile), by L. Smith, et.al., pp. 25-26, Dec. 1979.
7. Vehicle Research Corporation Report No. 26, High Performance Hollow Projectiles, by Scott Rhethorst, et.al., Aug. 1973.
8. Air Force Armament Test Laboratory Technical Report 77-109, Spinning Tubular Projectile Test Program, by T.D. Kitchun and J.W. Keeser, Jr., September 1977.
9. Brunsvold, R. S. and Kalivretenos, C. A., Spinning Tubular Projectile, Proceedings of the 10th Navy Symposium on Aeroballistics, v. 4, pp. 52-82, July 1975.
10. John, James E. A., Gas Dynamics, Allyn and Bacon, 1969.
11. National Advisory Committee on Aeronautics ACRL5D20, Preliminary Investigation of Supersonic Diffusers, by Arthur Kantrowitz and Coleman Du P. Donaldson, May 1945.
12. Shapiro, A. H., The Dynamics And Thermodynamics of Compressible Fluid Flow, Vol. II, Ronald Press, 1954.

13. Armament Research Laboratory Report 64-81, An Investigation of Constant Area Supersonic Flow Diffusion, by Andrew A. Fejer and others, May 1954.
14. Waltrup, P. J. and Billig, F. S., "Structure of Shock Waves in Cylindrical Ducts," AIAA Journal, Vol. 11, No. 10, pp. 1404-1408, October 1978.
15. Schlichting, H., Boundary Layer Theory, 7th ed., McGraw-Hill, 1979, p. 598.
16. National Advisory Committee on Aeronautics Technical Note 1135, Application of the Method of Characteristics to Supersonic Rotational Flow, by Anthony Ferri, September, 1946.
17. Ferri, Antonio, Elements of Aerodynamics of Supersonic Flows, McMillan, 1949.
18. Air Force Armament Propulsion Laboratory Technical Report 68-7, Investigation of the Low Speed Fixed Geometry Scramjet "Inlet Design Practice Manual", by J. Johnson, February 1968 AD829332.
19. Vehicle Research Corporation Report No. 29, Analytical Study of Tubular Projectiles Employing Consumable Sabots, by Scott Rhethorst, et.al., October 1975 (Revised April 1975).
20. Thomson, W. T., Introduction to Space Dynamics, John Wiley & Sons, N.Y. 1961.
21. Brock, John E., Rigid Body Dynamics and the Inertia Tensor, paper presented as class lecture series at Naval Postgraduate School, Monterey, California, July 1978.
22. Synge, J. L. and Griffith, B. A., Principles of Mechanics, 3d ed., McGraw-Hill, 1959.
23. Timoshento and Young, Advanced Dynamics, McGraw-Hill, 1948.
24. Nakabayashi, K., Frictional Moment of Flow Between Two Concentric Spheres, One of Which Rotates, J. of Fluids Engineering, Transactions of ASME, Vol. 100, No. 1, pp. 97-106, Mar. 1978.
25. Ward, J. R., Integ2 Computer Program for solving simultaneous differential equations, Naval Postgraduate School, Monterey, California, October 1963 (revised 11/71).

26. Flügge, Handbook of Engineering Mechanics, 1st ed., p. 20-5, McGraw-Hill, 1962.
27. Baumeister, T. and Marks, L. S., Standard Handbook for Mechanical Engineers, 7th ed., p. 3-35, McGraw-Hill, 1967.

INITIAL DISTRIBUTION LIST

1. Defense Technical Information Center 2  
Cameron Station  
Alexandria, Virginia 22314
2. Library, Code 0142 2  
Naval Postgraduate School  
Monterey, California 93940
3. Department Chairman, Code 69Mx 2  
Department of Mechanical Engineering  
Naval Postgraduate School  
Monterey, California 93940
4. Commander (Code 3205) 5  
Naval Weapons Center  
China Lake, Ca. 93555  
Attn: Dr. L. H. Smith
5. Professor R. H. Nunn, Code 69NN 5  
Naval Postgraduate School  
Monterey, California 93940
6. Professor G.N. Vanderplaats, Code 69Zw 1  
Naval Postgraduate School  
Monterey, California 93940
7. Mr. Len Young 2  
Aircraft Armament Division  
Naval Air Systems Command  
Code 54111D  
Arlington, Virginia 20360
8. LT James W. Bloomer II 5  
7601 Hardy St.  
Overland Park, Ks. 66204
9. Dr. William Oberkampf 1  
Div. 5631  
Sandia Labs  
Albuquerque, N.M. 87185
10. Dr. R. S. Brunsvold (Code K82) 1  
NAVSURFWEAPSCEN  
White Oak Lab  
Silver Spring, MD 20910

11. Mr. Howard Bensch  
EMD Photo Lab  
Naval Postgraduate School  
Monterey, California 93940

1